

<sup>1</sup> **Searches for Supersymmetry using the  $\alpha_T$   
<sup>2</sup> variable with the CMS detector at the LHC**

<sup>3</sup> Darren Burton

<sup>4</sup> Imperial College London  
<sup>5</sup> Department of Physics

<sup>6</sup> A thesis submitted to Imperial College London  
<sup>7</sup> for the degree of Doctor of Philosophy

## Abstract

10

## Declaration

11

I, the author of this thesis, declare that the work presented within this  
document to be my own. The work presented in Chapters 3.4.1, 4 and 6  
is a result of the authors own work or that of which I have been a major  
contributor unless explicitly stated otherwise, and is carried out within the  
context of the Imperial College London and CERN SUSY groups, itself a  
subsection of the greater CMS collaboration. All figures and studies taken  
from external sources are referenced appropriately throughout this document.

12

Darren Burton

13

14

15

16

17

18

19

## Acknowledgements

20

Of the many people who deserve thanks, some are particularly prominent....

# Preface

# **Contents**

23	<b>List of Figures</b>	ix
24	<b>List of Tables</b>	xii
25	<b>1. Introduction</b>	2
26	<b>2. A Theoretical Overview</b>	5
27	2.1. The Standard Model . . . . .	5
28	2.1.1. Gauge Symmetries of the SM . . . . .	7
29	2.1.2. The Electroweak Sector and Electroweak Symmetry Breaking . . . . .	9
30	2.2. Motivation for Physics Beyond the Standard Model . . . . .	13
31	2.3. Supersymmetry Overview . . . . .	15
32	2.3.1. R-Parity . . . . .	16
33	2.4. Experimental signatures of SUSY at the LHC . . . . .	17
34	2.4.1. Simplified Models . . . . .	18
35	<b>3. The LHC and the CMS Detector</b>	20
36	3.1. The LHC . . . . .	20
37	3.2. The CMS detector . . . . .	23
38	3.2.1. Detector Subsystems . . . . .	23
39	3.2.2. Tracker . . . . .	24
40	3.2.3. Electromagnetic Calorimeter . . . . .	25
41	3.2.4. Hadronic Calorimeter . . . . .	26
42	3.2.5. Muon Systems . . . . .	28
43	3.3. Event Reconstruction and Object Definition . . . . .	28
44	3.3.1. Jets . . . . .	28
45	3.3.2. B-tagging . . . . .	30
46	3.4. Triggering System . . . . .	32
47	3.4.1. The Level-1 Trigger . . . . .	34

48	3.4.2. L1 Trigger Jet Algorithm . . . . .	35
49	3.4.3. Measuring L1 Jet Trigger Efficiencies . . . . .	36
50	3.4.4. Effects of the L1 Jet Seed . . . . .	38
51	3.4.5. Robustness of L1 Jet Performance against Pile-up . . . . .	41
52	3.4.6. Summary . . . . .	44
53	<b>4. SUSY searches in Hadronic Final States</b>	<b>45</b>
54	4.1. An introduction to the $\alpha_T$ search . . . . .	46
55	4.1.1. The $\alpha_T$ variable . . . . .	48
56	4.2. Search Strategy . . . . .	50
57	4.2.1. Physics Objects . . . . .	52
58	4.2.2. Event Selection . . . . .	55
59	4.2.3. Control Sample Definition and Background Estimation . . . . .	57
60	4.2.4. Estimating the QCD Background Multi-jet Background . . . . .	64
61	4.3. Trigger Strategy . . . . .	66
62	4.4. Measuring MC normalisation factors via $H_T$ sidebands . . . . .	67
63	4.5. Determining MC Yields With Higher Statistical Precision . . . . .	68
64	4.5.1. The formula method . . . . .	69
65	4.5.2. Establishing proof of principle . . . . .	70
66	4.5.3. Correcting Measured Efficiencies In Simulation To Data . . . . .	70
67	4.6. Systematic Uncertainties On Transfer Factors . . . . .	71
68	4.6.1. Determining systematic uncertainties from closure tests . . . . .	74
69	<b>5. Searches For Natural SUSY With B-tag Templates.</b>	<b>78</b>
70	5.1. Concept . . . . .	78
71	5.2. Application to the $\alpha_T$ search . . . . .	79
72	5.2.1. Proof of principle in simulation . . . . .	81
73	<b>6. Results</b>	<b>82</b>
74	6.1. Statistical Interpretation . . . . .	82
75	6.2. Interpretation in Simplified Signal Models . . . . .	82
76	<b>A. Miscellaneous</b>	<b>83</b>
77	A.1. Noise Filters . . . . .	83
78	A.2. Primary Vertices . . . . .	85
79	<b>B. L1 Jets</b>	<b>87</b>
80	B.1. Jet matching efficiencies . . . . .	87

81	B.2. Leading Jet Energy Resolution . . . . .	88
82	B.3. Resolution for Energy Sum Quantities . . . . .	91
83	<b>C. Additional material on background estimation methods</b>	<b>96</b>
84	C.1. Determination of $k_{QCD}$ . . . . .	96
85	C.2. Effect of varying background cross sections on closure tests . . . . .	97
86	<b>Bibliography</b>	<b>99</b>

# <sup>87</sup> List of Figures

88	2.1. One loop quantum corrections to the Higgs squared mass parameter $m_h^2$ due to a fermion. . . . .	14
90	2.2. Two example simplified model decay chains. . . . .	19
91	3.1. A top down layout of the LHC, with the position of the four main detectors labelled. . . . .	21
93	3.2. The total integrated luminosity delivered to and collected by Compact Muon Solenoid (CMS) during the 2012 8 TeV $pp$ runs . . . . .	22
95	3.3. A pictorial depiction of the CMS detector. . . . .	24
96	3.4. Illustration of the CMS Electromagnetic CALorimeter (ECAL). . . . .	26
97	3.5. Schematic of the CMS Hadronic CALorimeter (HCAL). . . . .	27
98	3.6. Combined Secondary Vertex (CSV) algorithm discriminator values in enriched $t\bar{t}$ and inclusive multi jet samples . . . . .	31
100	3.7. Data/MC b-tag scale factors derived using the Combined Secondary Vertex Medium Working Point (CSVM) tagger. . . . .	32
102	3.8. Data/MC mis-tag scale factors derived using the CSVM tagger. . . . .	33
103	3.9. The CMS Level 1 Trigger (L1) Trigger system. . . . .	34
104	3.10. Illustration of the Level-1 jet finding algorithm. . . . .	36
105	3.11. L1 jet efficiency turn-on curves as a function of the offline CaloJet and PFJet $E_T$ . . . . .	38
107	3.12. L1 jet efficiency turn-on curves as a function of the offline CaloJet $E_T$ for the 2012 run period B and C. . . . .	39

---

109	3.13. Trigger cross section for the L1HTT150 trigger path. . . . .	40
110	3.14. L1 $H_T$ efficiency turn-on curves as a function of the offline CaloJet $H_T$ . . . . .	40
111	3.15. L1 jet efficiency turn-on curves as a function of the leading offline $E_T$ Calo	
112	(left) and PF (right) jet, for low, medium and high pile-up conditions. . . . .	41
113	3.16. Fit values from an Exponentially Modified Gaussian (EMG) function fitted	
114	to the resolution plots of leading Calo jet $E_T$ measured as a function of	
115	$\frac{(L1\ E_T - \text{Offline}\ E_T)}{\text{Offline}\ E_T}$ for low, medium and high pile-up conditions. . . . .	43
116	3.17. Fit values from an EMG function fitted to the resolution plots of leading	
117	PF jet $E_T$ measured as a function of $\frac{(L1\ E_T - \text{Offline}\ E_T)}{\text{Offline}\ E_T}$ for low, medium and	
118	high pile-up conditions. . . . .	43
119	4.1. Reconstructed offline $H_T$ for $11.7\text{fb}^{-1}$ of data after a basic pre-selection. . . . .	47
120	4.2. The event topologies of background QCD dijet events (right) and a generic	
121	SUPERSYmmetry (SUSY) signature with genuine $Z_T$ (left). . . . .	48
122	4.3. The $\alpha_T$ distributions for the low 2-3 (left) and high $\geq 4$ (right) jet	
123	multiplicities after a full analysis selection and shown for $H_T > 375$ . . . . .	49
124	4.4. Pictorial depiction of the analysis strategy employed by the $\alpha_T$ search to	
125	increase sensitivity to a wide spectra of SUSY models. . . . .	52
126	4.5. Data/MC comparisons of key variables for the hadronic signal region. . . . .	57
127	4.6. Data/MC comparisons of key variables for the $\mu + \text{jets}$ selection. . . . .	60
128	4.7. Data/MC comparisons of key variables for the $\mu\mu + \text{jets}$ selection. . . . .	62
129	4.8. Data/MC comparisons of key variables for the $\gamma + \text{jets}$ selection. . . . .	63
130	4.9. QCD sideband regions, used for determination of $k_{QCD}$ . . . . .	65
131	4.10. Sets of closure tests overlaid on top of the systematic uncertainty used for	
132	each of the five $H_T$ regions. . . . .	76
133	5.1. The b-tagging (a), c-quark mis-tagging (b), and light-quark mis-tagging	
134	rate (c) as measured in simulation after the $\alpha_T$ analysis, $\mu + \text{jets}$ control	
135	sample selection in the region $H_T > 375$ . . . . .	80

---

136	B.1. Leading jet matching efficiency as a function of the offline CaloJet $E_T$ . . . . .	87
137	B.2. Resolution plots of the leading offline Calo $E_T$ measured as a function of $\frac{(L1\ E_T - \text{Offline}\ E_T)}{\text{Offline}\ E_T}$ for low (a), medium (b) and high (c) pile-up conditions. . . . .	89
139	B.3. Resolution plots of the leading off-line PF $E_T$ measured as a function of $\frac{(L1\ E_T - \text{Offline}\ E_T)}{\text{Offline}\ E_T}$ for low (a), medium (b) and high (c) pile-up conditions. . . . .	91
141	B.4. $\sum E_T$ resolution parameters in bins of Calo $\sum E_T$ measured for the defined low, medium and high pile up conditions. . . . .	92
143	B.5. $\sum E_T$ resolution parameters in bins of PF $\sum E_T$ measured for the defined low, medium and high pile up conditions. . . . .	92
145	B.6. $\cancel{E}_T$ resolution parameters in bins of Calo $\cancel{E}_T$ measured for the defined low, medium and high pile up conditions. . . . .	93
147	B.7. $\cancel{E}_T$ resolution parameters in bins of PF $\cancel{E}_T$ measured for the defined low, medium and high pile up conditions. . . . .	93
149	B.8. $H_T$ resolution parameters in bins of Calo $H_T$ measured for the defined low, medium and high pile up conditions. . . . .	94
151	B.9. $H_T$ resolution parameters in bins of PF $H_T$ measured for the defined low, medium and high pile up conditions. . . . .	94
153	B.10. $\cancel{H}_T$ resolution parameters in bins of $\cancel{H}_T$ measured for the defined low, medium and high pile up conditions. . . . .	95
155	B.11. $\cancel{H}_T$ resolution parameters in bins of PF $\cancel{H}_T$ measured for the defined low, medium and high pile up conditions. . . . .	95
157	C.1. $R_{\alpha_T}(H_T)$ and exponential fits for each of the data sideband regions. Fit is conducted between the $H_T$ region $275 < H_T < 575$ . . . . .	96
159	C.2. Sets of closure tests overlaid on top of the systematic uncertainty used for each of the five $H_T$ regions. . . . .	97
161	C.3. Sets of closure tests overlaid on top of the systematic uncertainty used for each of the five $H_T$ regions. . . . .	97

# <sup>163</sup> List of Tables

<sup>164</sup>	2.1. The fundamental particles of the Standard Model (SM), with spin, charge and mass displayed. . . . .	6
<sup>165</sup>		
<sup>166</sup>	3.1. Results of a cumulative EMG function fit to the turn-on curves for L1 single jet triggers in 2012 Run Period C. . . . .	37
<sup>167</sup>		
<sup>168</sup>	3.2. Results of a cumulative EMG function fit to the turn-on curves for L1 single jet triggers in the 2012 run period B and C. . . . .	39
<sup>169</sup>		
<sup>170</sup>	3.3. Results of a cumulative EMG function fit to the turn-on curves for $H_T$ in 2012 run period B and C. . . . .	41
<sup>171</sup>		
<sup>172</sup>	3.4. Results of a cumulative EMG function fit to the efficiency turn-on curves for L1 single jet triggers in the 2012 run period C, for low,medium and high pile-up conditions. . . . .	42
<sup>173</sup>		
<sup>174</sup>		
<sup>175</sup>	3.5. Results of a cumulative EMG function fit to the efficiency turn-on curves for Level-1 single jet triggers in the 2012 run period C, for low,medium and high pile-up conditions. . . . .	42
<sup>176</sup>		
<sup>177</sup>		
<sup>178</sup>	4.1. A summary of the Simplified Model Spectra (SMS) models interpreted in this analysis, involving both direct (D) and gluino-induced (G) production of squarks and their decays. . . . .	46
<sup>179</sup>		
<sup>180</sup>		
<sup>181</sup>	4.2. Muon Identification criteria used within the analysis for selection/veto purposes in the muon control/signal selections. . . . .	53
<sup>182</sup>		
<sup>183</sup>	4.3. Photon Identification criteria used within the analysis for selection/veto purposes in the $\gamma +$ jets control/signal selections. . . . .	54
<sup>184</sup>		
<sup>185</sup>	4.4. Electron Identification criteria used within the analysis for veto purposes.	54

---

186	4.5. Jet thresholds used in the three $H_T$ regions of the analysis. . . . .	55
187	4.6. Best fit values for the parameters $k_{QCD}$ obtained from sideband regions	
188	B,C <sub>1</sub> ,C <sub>2</sub> ,C <sub>3</sub> . . . . .	66
189	4.7. Measured efficiencies of the $H_T$ and $\alpha_T$ legs of the HT and HT_alphaT triggers in independent analysis bins. . . . .	67
190		
191	4.8. k-factors calculated for different Electroweak Sector (EWK) processes. .	68
192	4.9. place holder . . . . .	70
193	4.10. A summary of the results obtained from fits of zeroeth order polynomials (i.e. a constant) to five sets of closure tests performed in the $2 \leq n_{jet} \leq 3$ bin . . . . .	73
194		
195		
196	4.11. A summary of the results obtained from fits of zeroeth order polynomials (i.e. a constant) to five sets of closure tests performed in the $n_{jet} \geq 4$ bin	73
197		
198	4.12. A summary of the results obtained from fits of zeroeth order polynomials (i.e. a constant) to five sets of closure tests performed in the $2 \leq n_{jet} \leq 3$ bin . . . . .	74
199		
200		
201	4.13. Calculated systematic uncertainties for the five $H_T$ regions, determined from the closure tests. . . . .	75
202		
203	A.1. Criteria for a reconstructed jet to pass the loose calorimeter jet id. . . . .	83
204	A.2. Criteria for a reconstructed jet to pass the loose PF jet id. . . . .	84
205	A.3. Noise filters that are applied to remove spurious and non-physical $\cancel{E}_T$ signatures within the CMS detector. . . . .	85
206		
207	A.4. Criteria for a vertex in an event to be classified as a 'good' reconstructed primary vertex. . . . .	86
208		
209	B.1. Results of a cumulative EMG function fit to the turn-on curves for the matching efficiency of the leading jet in an event to a Level-1 jet in run	
210	2012C and 2012B data. . . . .	88
211		
212	C.1. . . . .	97

---

**213 Acronyms**

214	<b>ALICE</b>	A Large Ion Collider Experiment
215	<b>ATLAS</b>	A Toroidal LHC ApparatuS
216	<b>APD</b>	Avalanche Photo-Diodes
217	<b>BSM</b>	Beyond Standard Model
218	<b>CERN</b>	European Organization for Nuclear Research
219	<b>CMS</b>	Compact Muon Solenoid
220	<b>CMSSM</b>	Compressed Minimal SuperSymmetric Model
221	<b>CSC</b>	Cathode Stripe Chamber
222	<b>CSV</b>	Combined Secondary Vertex
223	<b>CSVM</b>	Combined Secondary Vertex Medium Working Point
224	<b>DT</b>	Drift Tube
225	<b>ECAL</b>	Electromagnetic CALorimeter
226	<b>EB</b>	Electromagnetic CALorimeter Barrel
227	<b>EE</b>	Electromagnetic CALorimeter Endcap
228	<b>ES</b>	Electromagnetic CALorimeter pre-Shower
229	<b>EMG</b>	Exponentially Modified Gaussian
230	<b>EPJC</b>	European Physical Journal C
231	<b>EWK</b>	Electroweak Sector
232	<b>GCT</b>	Global Calorimeter Trigger
233	<b>GMT</b>	Global MuonTrigger
234	<b>GT</b>	Global Trigger
235	<b>HB</b>	Hadron Barrel
236	<b>HCAL</b>	Hadronic CALorimeter

237	<b>HE</b>	Hadron Endcaps
238	<b>HF</b>	Hadron Forward
239	<b>HLT</b>	Higher Level Trigger
240	<b>HO</b>	Hadron Outer
241	<b>HPD</b>	Hybrid Photo Diode
242	<b>LUT</b>	Look Up Table
243	<b>L1</b>	Level 1 Trigger
244	<b>LHC</b>	Large Hadron Collider
245	<b>LHCb</b>	Large Hadron Collider Beauty
246	<b>LSP</b>	Lightest Supersymmetric Partner
247	<b>NNLO</b>	Next to Next Leading Order
248	<b>POGs</b>	Physics Object Groups
249	<b>PS</b>	Proton Synchrotron
250	<b>QED</b>	Quantum Electro-Dynamics
251	<b>QCD</b>	Quantum Chromo-Dynamics
252	<b>QFT</b>	Quantum Field Theory
253	<b>RBXs</b>	Readout Boxes
254	<b>RPC</b>	Resistive Plate Chamber
255	<b>RCT</b>	Regional Calorimeter Trigger
256	<b>RMT</b>	Regional Muon Trigger
257	<b>SUSY</b>	SUPerSYmmetry
258	<b>SM</b>	Standard Model
259	<b>SMS</b>	Simplified Model Spectra
260	<b>SPS</b>	Super Proton Synchrotron
261	<b>TF</b>	Transfer Factor

<sup>262</sup>	<b>TP</b>	Trigger Primitive
<sup>263</sup>	<b>VEV</b>	Vacuum Expectation Value
<sup>264</sup>	<b>VPT</b>	Vacuum Photo-Triodes
<sup>265</sup>	<b>WIMP</b>	Weakly Interacting Massive Particle

<sup>266</sup>

*“The Universe is about 1,000,000 years old.”*

— Matthew Kenzie, 1987-present : Discoverer of the Higgs Boson.

<sup>267</sup>

# Chapter 1.

## 268 Introduction

269 During the 20th century great advances have been made in our understanding of the  
270 universe, where it comes from, where it is going and what it is made of. The Standard  
271 Model (**SM**) first formulated in the 1960's is one of the crowning achievements in science's  
272 quest to explain the most fundamental processes and interactions that make up our  
273 universe. It has provided a highly successful explanation of a wide range of phenomena  
274 in Particle Physics and has stood up to extensive experimental scrutiny [1].

275 Despite its successes it is not a complete theory, with significant questions remaining  
276 unanswered. It describes only three of the four known forces with gravity not incorpo-  
277 rated within the framework of the **SM**. Cosmological experiments infer that just  $\sim 4\%$   
278 of the observable universe exists as matter, with elusive "Dark Matter" accounting for a  
279 further  $\sim 23\%$  [2]. However no particle predicted by the **SM** is able to account for it. At  
280 higher energy scales and small distances the (non-)unification of the fundamental forces  
281 point to problems with the **SM** at least at higher energies not yet probed experimentally.

282 Many theories exist as extensions to the **SM** and predict a range of observables  
283 that can be detected at the Large Hadron Collider (**LHC**) of which SUperSYmmetry  
284 (**SUSY**) is one such example. It predicts a new symmetry of nature in which all current  
285 particles in the **SM** would have a corresponding supersymmetric partner. Common to  
286 most Supersymmetric theories is a stable, weakly interacting Lightest Supersymmetric  
287 Partner (**LSP**), which has the properties of a possible dark matter candidate. The **SM**  
288 and the main principles of Supersymmetric theories are outlined in Chapter 2, with  
289 emphasis placed on how experimental signatures of **SUSY** may reveal themselves at  
290 the **LHC**.

291        The experimental goal of the **LHC** is to further test the framework of the **SM**,  
292   exploring the TeV mass scale for the first time, and to seek a connection between the  
293   particles produced in proton collisions and dark matter. The first new discovery by  
294   this extraordinary machine was announced on the 4th of July 2012. The long-awaited  
295   discovery was the culmination decades of experimental endeavours in the search for the  
296   Higgs boson, providing an answer to the mechanism of electroweak symmetry breaking  
297   within the **SM** [3][4].

298        This discovery was made possible through data taken by the two multi purpose  
299   detectors (**CMS** and A Toroidal LHC ApparatuS (**ATLAS**)) located on the **LHC** ring.  
300   An experimental description of the **CMS** detector and the **LHC** is described in Chapter 3,  
301   including some of the object reconstruction used by **CMS** in searches for **SUSY** signatures.  
302   The performance of the **CMS** Level-1 calorimeter trigger, benchmarked by the author is  
303   also included within this chapter.

304        The analysis conducted by the author is detailed within Chapter 4. This chapter  
305   contains a description of the search for evidence of the production of Supersymmetric  
306   particles at the **LHC**. The main basis of the search centres around the kinematic  
307   dimensionless  $\alpha_T$  variable, which provides strong rejection of backgrounds with fake  
308   missing energy signatures whilst maintaining good sensitivity to a variety of **SUSY**  
309   topologies. The author's work as an integral part of the analysis group is documented in  
310   detail, which has culminated in numerous publications over the past two years. The latest  
311   of which was published in the European Physical Journal C (**EPJC**) [5] and contains the  
312   results which are discussed within this and the sequential Chapter.

313        The author in particular has played a major role in the extension of the  $\alpha_T$  analysis into  
314   the additional b-tagged and jet multiplicity dimensions increasing the sensitivity of the  
315   analysis to a range of **SUSY** topologies. Additionally the author has worked extensively  
316   in both increasing the statistical precision of electroweak predictions measured from  
317   simulation through analytical techniques, and the derivation of a data driven systematic  
318   uncertainty through the establishment of closure tests within the control samples of the  
319   analysis.

320        Additionally a method to search for **SUSY** signatures which are rich in top and bottom  
321   flavoured jet final states is disscussd in Chapter 5. A parametrisation of the b-tagging  
322   distribution for different Electroweak processes is used to establish templates, which  
323   are then used to estimate the expected number of 3 or 4 b-tagged jet events from **SM**

324 processes. The  $\alpha_T$  search is used as a cross check for this template method to establish  
325 it's functionality.

326 Finally the interpretation of such results within the framework of a variety of Simplified  
327 Model Spectra (**SMS**), which describe an array of possible **SUSY** event topologies is  
328 documented in Chapter 6. A description of the statistical model used to derive these  
329 interpretations and the possible implications of the results presented in this thesis is  
330 discussed within this Chapter. Natural units are used throughout this thesis in which  $\hbar$   
331 = c = 1.

# Chapter 2.

## <sup>332</sup> A Theoretical Overview

<sup>333</sup> Within this chapter, a brief introduction and background to the **SM** is given. Its success  
<sup>334</sup> as a rigorously tested and widely accepted theory is discussed as well as the deficiencies  
<sup>335</sup> with this theory that hint there this theory is not a complete description of our universe.  
<sup>336</sup> The motivations for new physics at the TeV scale and in particular Supersymmetric  
<sup>337</sup> theories are outlined within Section (2.3), with the chapter concluding with how an  
<sup>338</sup> experimental signature of such theories can be produced and observed at the **LHC**,  
<sup>339</sup> Section (2.4).

### <sup>340</sup> 2.1. The Standard Model

<sup>341</sup> The **SM** is the name given to the relativistic Quantum Field Theory (**QFT**), where  
<sup>342</sup> particles are represented as excitations of fields, which describes the interactions and  
<sup>343</sup> properties of all the known elementary particles [6][7][8][9]. It is a renormalisable field  
<sup>344</sup> theory which contains three symmetries:  $SU(3)$  for colour charge,  $SU(2)$  for weak isospin  
<sup>345</sup> and  $U(1)$  relating to weak hyper charge, which require its Lagrangian  $\mathcal{L}_{SM}$  to be invariant  
<sup>346</sup> under local gauge transformation.

<sup>347</sup> Within the **SM** theory, matter is composed of spin  $\frac{1}{2}$  fermions, which interact with each  
<sup>348</sup> other via the exchange of spin-1 gauge bosons. A summary of the known fundamental  
<sup>349</sup> fermions and bosons is given in Table 2.1.

<sup>350</sup> Fermions are separated into quarks and leptons of which only quarks interact with  
<sup>351</sup> the strong nuclear force. Quarks unlike leptons are not seen as free particles in nature,  
<sup>352</sup> but rather exist only within baryons, composed of three quarks with an overall integer  
<sup>353</sup> charge, and quark-anti-quark pairs called mesons. Both leptons and quarks are grouped

Particle	Symbol	Spin	Charge	Mass (GeV)
<b>First Generation Fermions</b>				
Electron Neutrino	$\nu_e$	$\frac{1}{2}$	0	$< 2.2 \times 10^{-6}$
Electron	e	$\frac{1}{2}$	-1	$0.51 \times 10^{-3}$
Up Quark	u	$\frac{1}{2}$	$\frac{2}{3}$	$2.3^{+0.7}_{-0.5} \times 10^{-3}$
Down Quark	d	$\frac{1}{2}$	$-\frac{1}{3}$	$4.8^{+0.7}_{-0.3} \times 10^{-3}$
<b>Second Generation Fermions</b>				
Muon Neutrino	$\nu_\mu$	$\frac{1}{2}$	0	-
Muon	$\mu$	$\frac{1}{2}$	-1	$1.05 \times 10^{-3}$
Charm Quark	c	$\frac{1}{2}$	$\frac{2}{3}$	$1.275 \pm 0.025$
Strange Quark	s	$\frac{1}{2}$	$-\frac{1}{3}$	$95 \pm 5 \times 10^{-3}$
<b>Third Generation Fermions</b>				
Tau Neutrino	$\nu_\tau$	$\frac{1}{2}$	0	-
Tau	$\tau$	$\frac{1}{2}$	-1	1.77
Top Quark	t	$\frac{1}{2}$	$\frac{2}{3}$	$173.5 \pm 0.8$
Bottom Quark	b	$\frac{1}{2}$	$-\frac{1}{3}$	$4.65 \pm 0.03$
<b>Gauge Bosons</b>				
Photon	$\gamma$	1	0	0
W Boson	$W^\pm$	1	$\pm 1$	$80.385 \pm 0.015$
Z Boson	Z	1	0	$91.187 \pm 0.002$
Gluons	g	1	0	0
Higgs Boson	H	0	0	$125.3 \pm 0.5$ [4]

**Table 2.1.:** The fundamental particles of the SM, with spin, charge and mass displayed. Latest mass measurements taken from [1].

354 into three generations which have the same properties, but with ascending mass in each  
 355 subsequent generation.

356 The gauge bosons mediate the interactions between fermions. The field theories  
 357 of Quantum Electro-Dynamics (QED) and Quantum Chromo-Dynamics (QCD), yield  
 358 massless mediator bosons, the photon and eight coloured gluons which are consequences  
 359 of the gauge invariance of those theories, detailed in Section (2.1.1).

360 The unification of the electromagnetic and weak-nuclear forces into the current  
 361 Electroweak theory yield the weak gauge bosons,  $W^\pm$  and Z through the mixing of the  
 362 associated gauge fields. The force carriers of this theory were experimentally detected by  
 363 the observation of weak neutral current, discovered in 1973 in the Gargamelle bubble

<sup>364</sup> chamber located at European Organization for Nuclear Research (**CERN**) [10], with the  
<sup>365</sup> masses of and the weak gauge bosons measured by the UA1 and U2 experiments at the  
<sup>366</sup> Super Proton Synchrotron (**SPS**) collider in 1983 [11][12].

<sup>367</sup> **2.1.1. Gauge Symmetries of the SM**

<sup>368</sup> Symmetries are of fundamental importance in the description of physical phenomena.  
<sup>369</sup> Noether's theorem states that for a dynamical system, the consequence of any symmetry  
<sup>370</sup> is an associated conserved quantity [13]. Invariance under translations, rotations, and  
<sup>371</sup> Lorentz transformations in physical systems lead to conservation of momentum, energy  
<sup>372</sup> and angular momentum.

<sup>373</sup> In the **SM**, a quantum theory described by Lagrangian formalism, the weak, strong and  
<sup>374</sup> electromagnetic interactions are described in terms of “gauge theories”. A gauge theory  
<sup>375</sup> possesses invariance under a set of “local transformations”, which are transformations  
<sup>376</sup> whose parameters are space-time dependent. The requirement of gauge invariance within  
<sup>377</sup> the **SM** necessitates the introduction of force-mediating gauge bosons and interactions  
<sup>378</sup> between fermions and the bosons themselves. Given the nature of the topics covered by  
<sup>379</sup> this thesis, the formulation of **EWK** within the **SM** Lagrangian is reviewed within this  
<sup>380</sup> section.

<sup>381</sup> The simplest example of the application of the principle of local gauge invariance  
<sup>382</sup> within the **SM** is in Quantum Electro-Dynamics (**QED**), the consequences of which  
<sup>383</sup> require a massless photon field [14][15].

<sup>384</sup> Starting from the free Dirac Lagrangian written as

$$\mathcal{L} = \bar{\psi}(i\gamma^\mu \partial_\mu - m)\psi, \quad (2.1)$$

<sup>385</sup> where  $\psi$  represents a free non interacting fermionic field, with the matrices  $\gamma^\mu, \mu \in$   
<sup>386</sup>  $0, 1, 2, 3$  defined by the anti commutator relationship  $\gamma^\mu \gamma^\nu + \gamma^\nu \gamma^\mu = 2\eta^{\mu\nu} I_4$  where  $\eta^{\mu\nu}$  is  
<sup>387</sup> the flat space-time metric  $(+, -, -, -)$  and  $I_4$  is the  $4 \times 4$  identity matrix.

<sup>388</sup> Under a local  $U(1)$  abelian gauge transformation in which  $\psi$  transforms as:

$$\psi(x) \rightarrow \psi'(x) = e^{i\theta(x)}\psi(x) \quad \bar{\psi}(x) \rightarrow \bar{\psi}'(x) = e^{i\theta(x)}\bar{\psi}(x) \quad (2.2)$$

389 the kinetic term of the Lagrangian does not remain invariant, due to the partial  
390 derivative interposed between the  $\bar{\psi}$  and  $\psi$  yielding,

$$\partial_\mu \psi \rightarrow e^{i\theta(x)} \partial_\mu \psi + i e^{i\theta(x)} \psi \partial_\mu \theta. \quad (2.3)$$

391 To ensure that  $\mathcal{L}$  remains invariant, a modified derivative,  $D_\mu$ , that transforms  
392 covariantly under phase transformations is introduced. In doing this a vector field  $A_\mu$   
393 with transformation properties that cancel out the unwanted term in (2.3) must also be  
394 included,

$$D_\mu \equiv \partial_\mu - ieA_\mu, \quad A_\mu \rightarrow A_\mu + \frac{1}{e} \partial_\mu \theta. \quad (2.4)$$

395 Invariance of the Lagrangian is then achieved by replacing  $\partial_\mu$  by  $D_\mu$ :

$$\begin{aligned} \mathcal{L} &= i\bar{\psi}\gamma^\mu D_\mu \psi - m\bar{\psi}\psi \\ &= \bar{\psi}(i\gamma^\mu \partial_\mu - m)\psi + e\bar{\psi}\gamma^\mu \psi A_\mu \end{aligned} \quad (2.5)$$

396 An additional interaction term is now present in the Lagrangian, coupling the Dirac  
397 particle to this vector field, which is interpreted as the photon in QED. To regard this  
398 new field as the physical photon field, a term corresponding to its kinetic energy must be  
399 added to the Lagrangian from Equation (2.5). Since this term must also be invariant  
400 under the conditions of Equation (2.4), it is defined in the form  $F_{\mu\nu} = \partial^\mu A^\nu - \partial^\nu A^\mu$ .

401 This then leads to the Lagrangian of QED:

$$\mathcal{L}_{QED} = \underbrace{i\bar{\psi}\gamma^\mu\partial_\mu\psi - \frac{1}{4}F_{\mu\nu}F^{\mu\nu}}_{\text{kinetic term}} + \underbrace{m\bar{\psi}\psi}_{\text{mass term}} + \underbrace{e\bar{\psi}\gamma^\mu\psi A_\mu}_{\text{interaction term}} \quad (2.6)$$

402 Within the Lagrangian there remains no mass term of the form  $m^2A_\mu A^\mu$ , which is  
 403 prohibited by gauge invariance. This implies that the gauge particle, the photon, must  
 404 be massless.

### 405 2.1.2. The Electroweak Sector and Electroweak Symmetry 406 Breaking

407 The same application of gauge symmetry and the requirement of local gauge invariance  
 408 can be used to unify QED and the Weak force in the Electroweak Sector (EWK).  
 409 The nature of EWK interactions is encompassed within a Lagrangian invariant under  
 410 transformations of the group  $SU(2)_L \times U(1)_Y$ .

411 The weak interactions from experimental observation [16], are known to violate parity  
 412 and are therefore not symmetric under interchange of left and right helicity fermions.  
 413 Thus within the SM the left and right handed parts of these fermion fields are treated  
 414 separately. A fermion field is then split into two left and right handed chiral components,  
 415  $\psi = \psi_L + \psi_R$ , where  $\psi_{L/R} = (1 \pm \gamma^5)\psi$ .

416 The  $SU(2)_L$  group is the special unitary group of  $2 \times 2$  matrices  $U$  satisfying  $UU^\dagger = I$   
 417 and  $\det(U) = 1$ . It may be written in the form  $U = e^{-i\omega_i T_i}$ , with the generators of the  
 418 group  $T_i = \frac{1}{2}\tau_i$  where  $\tau_i$ ,  $i \in 1,2,3$  being the  $2 \times 2$  Pauli matrices

$$\tau_1 = \begin{pmatrix} 0 & 1 \\ 1 & 0 \end{pmatrix} \quad \tau_2 = \begin{pmatrix} 0 & -i \\ i & 0 \end{pmatrix} \quad \tau_3 = \begin{pmatrix} 1 & 0 \\ 0 & -1 \end{pmatrix}, \quad (2.7)$$

419 which form a non Abelian group obeying the commutation relation  $[T^a, T^b] \equiv$   
 420  $if^{abc}T^c \neq 0$ . The gauge fields that accompany this group are represented by  $\hat{W}_\mu =$   
 421  $(\hat{W}_\mu^1, \hat{W}_\mu^2, \hat{W}_\mu^3)$  and act only on the left handed component of the fermion field  $\psi_L$ .

<sup>422</sup> One additional generator  $Y$  which represents the hypercharge of the particle under  
<sup>423</sup> consideration is introduced through the  $U(1)_Y$  group acting on both components of the  
<sup>424</sup> fermion field, with an associated vector boson field  $\hat{B}_\mu$ .

<sup>425</sup> The  $SU(2)_L \times U(1)_Y$  transformations of the left and right handed components of  $\psi$   
<sup>426</sup> are summarised by,

$$\begin{aligned}\chi_L &\rightarrow \chi'_L = e^{i\theta(x) \cdot T + i\theta(x)Y} \chi_L, \\ \psi_R &\rightarrow \psi'_R = e^{i\theta(x)Y} \psi_R,\end{aligned}\tag{2.8}$$

<sup>427</sup> where the left handed fermions form isospin doubles  $\chi_L$  and the right handed fermions  
<sup>428</sup> are isosinglets  $\psi_R$ . For the first generation of leptons and quarks this represents

$$\begin{aligned}\chi_L &= \begin{pmatrix} \nu_e \\ e \end{pmatrix}_L, \quad \begin{pmatrix} u \\ d \end{pmatrix}_L \\ \psi_R &= e_R, \quad u_R, d_R\end{aligned}\tag{2.9}$$

<sup>429</sup> Imposing local gauge invariance within  $\mathcal{L}_{EWK}$  is once again achieved by modifying  
<sup>430</sup> the covariant derivative

$$D_\mu = \partial_\mu - \frac{ig}{2} \tau^i W_\mu^i - \frac{ig'}{2} Y B_\mu,\tag{2.10}$$

<sup>431</sup> where  $g$  and  $g'$  are the coupling constant of the  $SU(2)_L$  and  $U(1)_Y$  groups respectively.  
<sup>432</sup> Taking the example of the first generation of fermions defined in Equation.(2.9), with input  
<sup>433</sup> hypercharge values of -1 and -2 for  $\chi_L$  and  $e_R$  respectively, would lead to a Lagrangian  
<sup>434</sup>  $\mathcal{L}_1$  of the form,

$$\begin{aligned}\mathcal{L}_1 = &\bar{\chi}_L \gamma^\mu [i\partial_\mu - g \frac{1}{2} \tau \cdot W_\mu - g' (-\frac{1}{2}) B_\mu] \chi_L \\ &+ \bar{e}_R \gamma^\mu [i\partial_\mu - g' (-1) B_\mu] e_R - \frac{1}{4} W_{\mu\nu} \cdot W^{\mu\nu} - \frac{1}{4} B_{\mu\nu} B^{\mu\nu}.\end{aligned}\tag{2.11}$$

<sup>435</sup> As in **QED**, these additional gauge fields introduce field strength tensors  $B_{\mu\nu}$  and  
<sup>436</sup>  $W_{\mu\nu}$ ,

$$\hat{B}_{\mu\nu} = \partial_\mu \hat{B}_\nu - \partial_\nu \hat{B}_\mu \quad (2.12)$$

$$\hat{W}_{\mu\nu} = \partial_\mu \hat{W}_\nu - \partial_\nu \hat{W}_\mu - g \hat{W}_\mu \times \hat{W}_\nu \quad (2.13)$$

<sup>437</sup> corresponding to the kinetic energy and self coupling of the  $W_\mu$  fields and the kinetic  
<sup>438</sup> energy term of the  $B_\mu$  field.

<sup>439</sup> None of these gauge bosons are physical particles, and instead linear combinations of  
<sup>440</sup> these gauge bosons make up  $\gamma$  and the W and Z bosons, defined as

$$W^\pm = \frac{1}{\sqrt{2}} (W_\mu^1 \mp i W_\mu^2) \quad \begin{pmatrix} Z_\mu \\ A_\mu \end{pmatrix} = \begin{pmatrix} \cos\theta_W & -\sin\theta_W \\ \sin\theta_W & \cos\theta_W \end{pmatrix} \begin{pmatrix} W_\mu^3 \\ B_\mu \end{pmatrix} \quad (2.14)$$

<sup>441</sup> where the mixing angle,  $\theta_w = \tan^{-1} \frac{g'}{g}$ , relates the coupling of the neutral weak and  
<sup>442</sup> electromagnetic interactions.

<sup>443</sup> As in the case of the formulation of the **QED** Lagrangian there remains no mass term  
<sup>444</sup> for the photon. However this is also the case for the W, Z and fermions in the Lagrangian,  
<sup>445</sup> contrary to experimental measurement. Any explicit introduction of mass terms would  
<sup>446</sup> break the symmetry of the Lagrangian and instead mass terms can be introduced through  
<sup>447</sup> spontaneous breaking of the **EWK** symmetry via the Higgs mechanism.

<sup>448</sup> The Higgs mechanism induces spontaneous symmetry breaking through the introduc-  
<sup>449</sup> tion of a complex scalar SU(2) doublet field  $\phi$  which attains a non-zero Vacuum  
<sup>450</sup> Expectation Value (**VEV**) [17][18][19][20].

$$\phi = \begin{pmatrix} \phi^+ \\ \phi^0 \end{pmatrix} \quad \text{with} \quad \begin{aligned} \phi^+ &\equiv (\phi_1 + i\phi_2)/\sqrt{2} \\ \phi^0 &\equiv (\phi_3 + i\phi_4)/\sqrt{2} \end{aligned} \quad (2.15)$$

451 The Lagrangian defined in Equation (2.11) attains an additional term  $\mathcal{L}_{Higgs}$  of the  
 452 form

$$\mathcal{L}_{Higgs} = \overbrace{(D_\mu \phi)^\dagger (D^\mu \phi)}^{\text{kinetic}} - \overbrace{\mu^2 \phi^\dagger \phi - \lambda (\phi^\dagger \phi)^2}^{\text{potential } V(\phi)} \quad (\mu^2, \lambda) > 0 \in \mathbb{R},$$

$$\mathcal{L}_{SM} = \mathcal{L}_{EWK} + \mathcal{L}_{Higgs}, \quad (2.16)$$

453 where the covariant derivative  $D_\mu$  is that defined in Equation (2.10). The last two  
 454 terms of  $\mathcal{L}_{Higgs}$  correspond to the Higgs potential, in which positive real positive values  
 455 of  $\mu^2$  and  $\lambda$  are required to ensure the generation of masses for the bosons and leptons.  
 456 The minimum of this potential is found at  $\phi^\dagger \phi = \frac{1}{2}(\phi_1^2 + \phi_2^2 + \phi_3^2 + \phi_4^2) = \mu^2/\lambda = v^2$ ,  
 457 where  $v$  represents the **VEV**.

458 Defining the ground state of the  $\phi$  field to be consistent with the  $V(\phi)$  minimum, and  
 459 then expanding around a ground state chosen to maintain an unbroken electromagnetic  
 460 symmetry thus preserving a zero photon mass [21] leads to

$$\phi_0 = \sqrt{\frac{1}{2}} \begin{pmatrix} 0 \\ v \end{pmatrix}, \quad \phi(x) = e^{i\tau \cdot \theta(x)/v} \sqrt{\frac{1}{2}} \begin{pmatrix} 0 \\ v + h(x) \end{pmatrix}, \quad (2.17)$$

461 where the fluctuations from the vacuum  $\phi_0$  are parametrized in terms of four real  
 462 fields,  $\theta_1, \theta_2, \theta_3$  and  $h(x)$ .

463 Choosing to gauge away the three massless Goldstone boson fields by setting  $\theta(x)$  to  
 464 zero and substituting  $\phi(x)$  back into kinetic term of  $\mathcal{L}_{Higgs}$  from Equation (2.16) leads to  
 465 mass terms for the  $W^\pm$  and  $Z$  bosons

$$(D_\mu \phi)^\dagger (D^\mu \phi) = \frac{1}{2}(\partial_\mu h)^2 + \frac{g^2 v^2}{2} W_\mu^+ W^{-\mu} + \frac{v^2 g^2}{8 \cos^2 \theta_w} Z_\mu Z^\mu + 0 A_\mu A^\mu, \quad (2.18)$$

466 where the relations between the physical and electroweak gauge fields from Equation  
 467 (2.14) are used. The  $W^\pm$  and  $Z$  bosons can then be determined to be

$$M_W = \frac{1}{2}gv \quad M_Z = \frac{1}{2} \frac{gv}{\cos \theta_w}. \quad (2.19)$$

468 This mechanism is also used to generate fermion masses by introducing a Yukawa  
 469 coupling between the fermions and the  $\phi$  field [22], with the coupling strength of a particle  
 470 to the  $\phi$  field governing its mass. Additionally a scalar boson  $h$  with mass  $m_h = v\sqrt{\frac{\lambda}{2}}$ , is  
 471 also predicted as a result of this spontaneous symmetry breaking and became known as  
 472 the Higgs boson. Its discovery by the CMS and ATLAS experiments in 2012 is concrete  
 473 evidence to support this method of mass generation within the SM.

## 474 2.2. Motivation for Physics Beyond the Standard 475 Model

476 As has been described, the SM has proved to be a very successful theory, predicting the  
 477 existence of the  $W^\pm$  and  $Z$  bosons and the top quark long before they were experimentally  
 478 observed. However the theory does not accurately describe all observed phenomena and  
 479 has some fundamental theoretical flaws that hint at the need for additional extensions to  
 480 the current theory.

481 On a theoretical level, the SM is unable to incorporate the gravitational interactions  
 482 of fundamental particles within the theory. Whilst at the electroweak energy scales the  
 483 relative strength of gravity is negligible compared to the other three fundamental forces,  
 484 at much higher energy scales  $M_{planck} \sim 10^{18} GeV$  quantum gravitational effects become  
 485 increasingly dominant. The failure to reconcile gravity within the SM, demonstrates that  
 486 the SM must become invalid at some higher energy scale.

487 Some other deficiencies with the SM include the fact that the predicted rate of  
 488 Charge-Parity violation does not account for the matter dominated universe which we  
 489 inhabit, and the SM prediction of zero neutrino mass conflicts with the observation of  
 490 neutrino flavour mixing, attributed to mixing between neutrino mass eigenstates [23][24].

491 Perhaps one of the most glaring gaps in the predictive power of the SM is that there  
 492 exists no candidate to explain the cosmic dark matter observed in galactic structures  
 493 through indirect techniques including gravitational lensing and measurement of the  
 494 orbital velocity of stars in galactic edges. Any such candidate must be very weakly

495 interacting which must also be stable, owing to the lack of direct detection of the decay  
496 products of such an process. Providing a dark matter candidate is of the prime goals  
497 which be tackled by any Beyond Standard Model (**BSM**) physics model.

498 The recent discovery of the Higgs boson whilst a significant victory for the predictive  
499 power of the **SM**, brings with it still unresolved questions. This issue is commonly  
500 described as the “hierarchy problem”.

501 In the absence of new physics between the TeV and Planck scale, calculating beyond  
502 tree-level contributions to the Higgs mass term given by its self interaction, result in  
503 divergent terms that push the Higgs mass up to the planck mass  $M_{planck}$ .

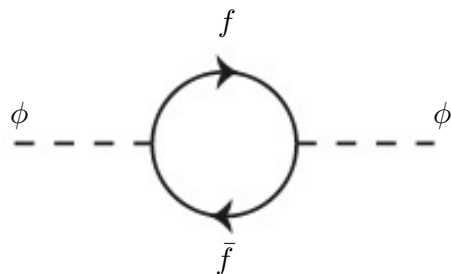


**Figure 2.1.:** One loop quantum corrections to the Higgs squared mass parameter  $m_h^2$  due to a fermion.

504 This can be demonstrated by considering the one loop quantum correction to the  
505 Higgs mass with a fermion  $f$ , shown in Figure 2.1 with mass  $m_f$ . The Higgs field couples  
506 to  $f$  with a term in the Lagrangian  $-\lambda_f h \bar{f} f$ , yielding a correction of the form [25],

$$\delta m_h^2 = -\frac{|\lambda_f|^2}{8\pi^2} \Lambda^2 + \dots, \quad (2.20)$$

507 where  $\lambda_f$  represents the coupling strength for each type of fermion  $\propto m_f$ , and  $\Lambda$  the  
508 cutoff energy scale at which the **SM** ceases to be a valid theory.

509 To recover the mass of the now discovered Higgs boson would require a fine-tuning of  
510 the parameters to cancel out these mass corrections the the Higgs mass to the scale of  
511 30 orders of magnitude. This appears as an unnatural solution to physicists and it is  
512 this hierarchy problem that provides one of the strongest motivations for the theory of  
513 SUperSYmmetry (**SUSY**).

### <sup>514</sup> 2.3. Supersymmetry Overview

<sup>515</sup> Supersymmetry provides potential solutions to many of the issues raised in the previous  
<sup>516</sup> section. It provides a dark matter candidate, can explain baryogenesis in the early  
<sup>517</sup> universe and also provides an elegant solution to the hierarchy problem [26][27][28][29].  
<sup>518</sup> At its heart it represents a new space-time symmetry that relates fermions and bosons.  
<sup>519</sup> This symmetry converts bosonic states into fermionic states, and vice versa, see Equation  
<sup>520</sup> (2.21) ,

$$Q|Boson\rangle = |Fermion\rangle \quad Q|Fermion\rangle = |Boson\rangle, \quad (2.21)$$

<sup>521</sup> where the operator  $Q$  is the generator of these transformations. Quantum field theories  
<sup>522</sup> which are invariant under such transformations are called supersymmetric.

<sup>523</sup> This symmetry operator therefore acts upon a particles spin altering it by a half integer  
<sup>524</sup> value. The consequences of the introduction of this additional space-time symmetry  
<sup>525</sup> introduce a new rich phenomenology. For example in supersymmetric theories, both  
<sup>526</sup> the left handed  $SU(2)$  doublet and right handed singlet of fermions will have a spin-0  
<sup>527</sup> superpartner, containing the same electric charge, weak isospin, and colour as its **SM**  
<sup>528</sup> partner. In the case of the leptons  $(\nu_l, l)_L$  will have two superpartners, a sneutrino  $\tilde{\nu}_l{}_L$   
<sup>529</sup> and a slepton  $\tilde{l}_L$ , whilst the singlet  $l_R$  also has a superpartner slepton  $\tilde{l}_R$ .

<sup>530</sup> Each particle in a supersymmetric theory is paired together with their superpartners  
<sup>531</sup> as a result of this supersymmetric transformations in a so called supermultiplet. These  
<sup>532</sup> superpartners will then consequently also contribute to the corrections to the Higgs mass.  
<sup>533</sup> Bosonic and fermionic loops contributing to the correction appear with opposite signs,  
<sup>534</sup> and therefore cancellation of these divergent terms will stabilise the Higgs mass, solving  
<sup>535</sup> the hierarchy problem [30][31].

<sup>536</sup> One of the simplest forms of **SUSY** would predict a whole set of supersymmetric  
<sup>537</sup> partners to their **SM** counterparts with the same mass and interactions. However the  
<sup>538</sup> currently lack of any experimental evidence for the predicted sparticle spectrum implies  
<sup>539</sup> **SUSY** must be a broken symmetry in which any sparticle masses must be greater than  
<sup>540</sup> their SM counterparts.

<sup>541</sup> There exist many techniques which can induce supersymmetric breaking [32][33][34].  
<sup>542</sup> Of particular interest to experimental physicists are those at which the breaking scale

<sup>543</sup> is of an order that is experimentally accessible to the LHC i.e.  $\sim$  TeV scale. Whilst  
<sup>544</sup> there is no requirement for supersymmetric breaking to occur at this energy scale, for  
<sup>545</sup> supersymmetry to provide a solution to the hierarchy problem, it is necessary for this  
<sup>546</sup> scale to not differ too drastically from the EWK scale [35][36].

### <sup>547</sup> 2.3.1. R-Parity

<sup>548</sup> Some supersymmetric theories also present a solution to the dark matter problem. Such  
<sup>549</sup> theories can contain a Lightest Supersymmetric Partner (LSP), which matches the criteria  
<sup>550</sup> of a Weakly Interacting Massive Particle (WIMP) required by cosmological observation  
<sup>551</sup> if R-parity is conserved.

<sup>552</sup> Baryon (B) and Lepton (L) number conservation is forbidden in the SM by renor-  
<sup>553</sup> malisability requirements. The violation of Baryon or Lepton number would result in  
<sup>554</sup> the proton lifetime much shorter than those set by experimental limits [37]. Another  
<sup>555</sup> symmetry called R-parity is then often introduced to SUSY theories to maintain baryon  
<sup>556</sup> and lepton conservation.

<sup>557</sup> R-parity is described by the equation

$$R_P = (-1)^{3(B-L)+2s}, \quad (2.22)$$

<sup>558</sup> where s represents the spin of the particles.  $B = \pm \frac{1}{3}$  for quarks/antiquarks and  $B = 0$   
<sup>559</sup> for all others,  $L = \pm 1$  for leptons/antileptons,  $L = 0$  for all others.

<sup>560</sup> R-parity ensures the stability of the proton in SUSY models, and also has other  
<sup>561</sup> consequences for the production and decay of supersymmetric particles. At particle  
<sup>562</sup> colliders supersymmetric particles can only be pair produced, and similarly the decay  
<sup>563</sup> of any produced supersymmetric particle is restricted to a SM particle and a lighter  
<sup>564</sup> supersymmetric particle as allowed by conservation laws. A further implication of R-  
<sup>565</sup> parity is that once a supersymmetric particle has decayed to the LSP it remains stable,  
<sup>566</sup> unable to decay into a SM particle.

<sup>567</sup> A LSP would not interact in a detector at a particle collider, leaving behind a missing  
<sup>568</sup> energy  $\cancel{E}_T$  signature. The assumption of R-parity and its consequences are used to  
<sup>569</sup> determine the physical motivation and search strategies for SUSY model at the LHC.

## 570 2.4. Experimental signatures of SUSY at the LHC

571 Should strongly interacting sparticles be within the experimental reach of the LHC, then  
572 it is expected that they can be produced in a variety of ways.

- 573 • squark/anti-squark and gluino pairs can be produced via both gluon fusion and  
574 quark/anti-quark scattering.
- 575 • a gluino and squark produced together via quark-gluon scattering
- 576 • squark pairs produced via quark-quark scattering

577 Whilst most SUSY searches invoke the requirement of R-parity to explore parameter  
578 phase space, there still exist a whole plethora of possible SUSY model topologies which  
579 could be discovered at the LHC.

580 During the 2011 run period at a  $\sqrt{s} = 7$  TeV particular models were used to benchmark  
581 performance and experimental reach of both CMS searches and previous experiments.  
582 The Compressed Minimal SuperSymmetric Model (CMSSM) was initially chosen for a  
583 number of reasons [38]. One of the most compelling being the reduction from the up to  
584 105 new parameters introduced by SUSY in addition to the existing 19 of the SM to that  
585 of just 5 free extra free parameters. It was this simplicity, combined with the theory not  
586 requiring any fine tuning of particle masses to produce the experimentally verified SM  
587 that made it an attractive model to interpret physics results.

588 However recent results from the LHC now strongly disfavour large swathes of CMSSM  
589 parameter space [39][40][41]. In the face of such results a more pragmatic model indepen-  
590 dent search strategy is now applied across most SUSY searches at the LHC, see Section  
591 (2.4.1).

592 As previously stated, a stable LSP that exhibits the properties of a dark matter would  
593 be weakly interacting and therefore will not be directly detected in a detector environment.  
594 Additionally the cascade decays of supersymmetric particles to the LSP would also result  
595 in significant hadronic activity. These signatures can then be characterised through  
596 large amounts of hadronic jets (see Section (3.3.1)), leptons and a significant amount of  
597 missing energy dependent upon the size of the mass splitting between the LSP and the  
598 supersymmetric particle it has decayed from.

599 Whilst the SM contains processes which can exhibit a similar event topology to that  
600 described above. The largest contribution of which comes in from the general QCD

601 environment of a hadron collider. A multitude of different analytical techniques are used  
602 by experimental physicists to reduce or estimate any reducible or irreducible backgrounds,  
603 allowing a possible **SUSY** signature to be extracted. The techniques employed within  
604 this thesis are described in great detail within Section (4.1).

605 **2.4.1. Simplified Models**

606 With such a variety of different ways for a **SUSY** signal to manifest itself, it is necessary  
607 to be able to interpret experimental reach through the masses of gluinos and squarks  
608 which can excluded by experimental searches rather than on a model specific basis.

609 This is accomplished through **SMS** models, which are defined by a set of hypothetical  
610 particles and a sequence of their production and decay [42][43]. In the **SMS** models  
611 considered within this thesis, only the production process for the two primary particles  
612 are considered. Each primary particle can undergo a direct or a cascade decay through  
613 an intermediate new particle. At the end of each decay chain there remains a neutral,  
614 undetected **LSP** particle, denoted  $\tilde{\chi}_{LSP}$  which can represent a neutralino or gravitino.  
615 Essentially it is easier to consider each **SMS** with branching ratios set to 100% The  
616 masses of the primary particle and the **LSP** remain as free parameters, in which the  
617 absolute value and relative difference between the primary and **LSP** particle alter the  
618 kinematics of the event.

619 Different **SMS** models are denoted with a T-prefix, with a summary of the types  
620 interpreted within this thesis listed below [44].

- 621 • **T1,T1xxxx**, models represent a simplified version of gluino pair production with  
622 each gluino (superpartner to the gluon) undergoing a three-body decay to a quark-  
623 antiquark pair and the **LSP** (i.e.  $\tilde{g} \rightarrow q\bar{q}\tilde{\chi}_{LSP}$ ). The resultant final state from this  
624 decay is typically 4 jets +  $\cancel{E}_T$  in the absence of initial/final state radiation and  
625 detector effects. xxxx denotes models in which the quarks are of a specific flavour,  
626 typically t or b quark-antiquarks.
- 627 • **T2,T2xx**, models represent a simplified version of squark anti-squark production  
628 with each squark undergoing a two-body decay into a light-flavour quark and **LSP**  
629 (i.e.  $\tilde{q} \rightarrow q\tilde{\chi}_{LSP}$ ). This results in final states with less jets than gluino mediated  
630 production, typically 2 jets +  $\cancel{E}_T$  when again ignoring the effect of initial/final state  
631 radiation and detector effects. xx models again represent decays in which both the  
632 quark and the squark within the decay is of a specific flavour, typically  $\tilde{t}/t$  or  $\tilde{b}/b$ .

Models rich in b and t quarks are interpreted within this thesis as they remain of particular interest within “Natural SUSY” scenarios [45][46]. The largest contribution to the quadratic divergence in the Higgs mass parameter comes from a loop of top quarks via the Yukawa coupling. Cancellation of these divergences can be achieved in supersymmetric theories by requiring a light right handed top squark,  $\tilde{t}_R$ , and left-handed double  $SU(2)_L$  doublet containing top and bottom squarks,  $(\tilde{\frac{t}{b}})_L$  [47].

These theories therefore solve the hierarchy problem by predicting light  $\sim$  EWK scale third generation sleptons, to be accessible at the LHC. Search strategies involving the requirement of b-tagging (see Section (3.3.2)) are used to give sensitivity to these type of SUSY scenarios and are discussed in greater detail within Chapter 6.

Two example decay chains are shown in Figure 2.2; the pair production of gluinos (T1) and the pair production of squarks (T2) decaying into SM particles and LSP’s.

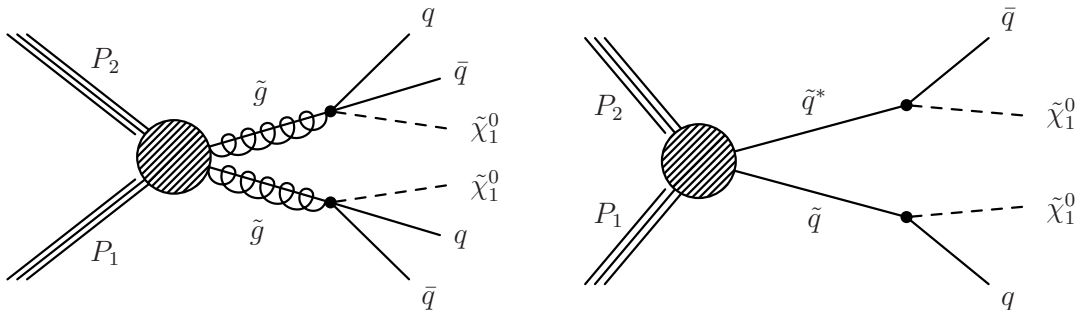


**Figure 2.2.:** Two example SMS model decays (T1 (left), T2 (right)), which are used in interpretations of physics reach by CMS.

# Chapter 3.

## 645 The LHC and the CMS Detector

646 Probing the SM for signs of new physics would not be possible without the immensely  
647 complex electronics and machinery that makes the TeV energy scale accessible for the  
648 first time. This chapter will cover the LHC based at European Organization for Nuclear  
649 Research (CERN) and the Compact Muon Solenoid (CMS) detector, being the experiment  
650 the author is a member of. Section (3.2) serves to introduce an overview of the different  
651 components of the CMS detector, with more detail spent on those that are relevant in  
652 the search for Supersymmetric particles. Section (3.3) will focus on event and object  
653 reconstruction again with more emphasis on jet level quantities which are most relevant  
654 to the author's analysis research. Finally Section (3.4) will cover work performed by  
655 the author, as service to the CMS Collaboration, in measuring the performance of the  
656 Global Calorimeter Trigger (GCT) component of the L1 trigger during the 2012-2013  
657 run period.

### 658 3.1. The LHC

659 The LHC is a storage ring, accelerator, and collider of circulating beams of protons or  
660 ions. Housed in the tunnel dug for the Large Electron-Positron collider (LEP), it is  
661 approximately 27 km in circumference, 100 m underground, and straddles the border  
662 between France and Switzerland outside of Geneva. It is currently the only collider  
663 in operation that is able to study physics at the TeV scale. A double-ring circular  
664 synchrotron, it was designed to collide both proton-proton (pp) and heavy ion (PbPb)  
665 with a centre of mass energy  $\sqrt{s} = 14$  TeV at a final design luminosity of  $10^{34}\text{cm}^{-2}\text{s}^{-1}$ .

666

These counter-circulating beams of protons/Pb ions are merged in four sections around the ring to enable collisions of the beams, with each interaction point being home to one of the four major experiments; A Large Ion Collider Experiment (**ALICE**) [48], A Toroidal LHC ApparatuS (**ATLAS**) [49], Compact Muon Solenoid (**CMS**) [50] and Large Hadron Collider Beauty (**LHC-B**) [51] which record the resultant collisions. The layout of the **LHC** ring is shown in Figure 3.1. The remaining four sections contain acceleration, collimation and beam dump systems. In the eight arc sections, the beams are steered by magnetic fields of up to 8 T provided by super conduction dipole magnets, which are maintained at temperatures of 2 K using superfluid helium. Additional magnets for focusing and corrections are also present in straight sections within the arcs and near the interaction regions where the detectors are situated.

678

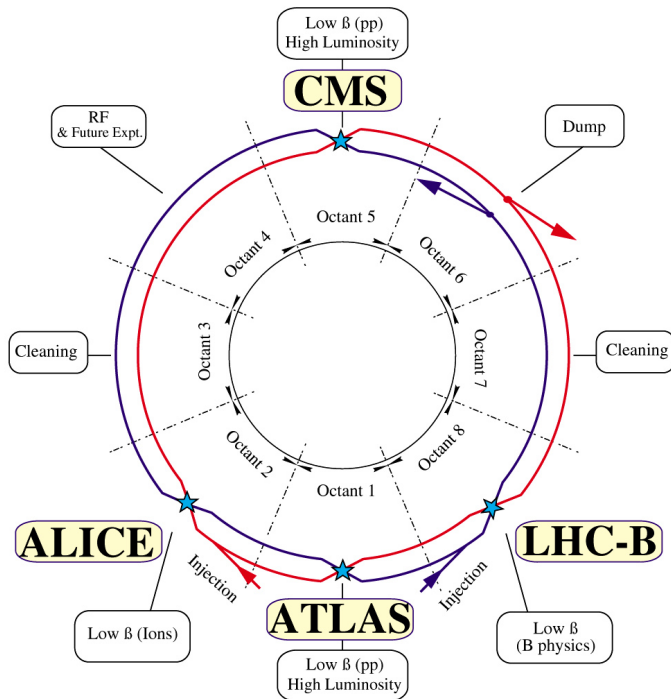


**Figure 3.1.:** A top down layout of the LHC. [52], with the position of the four main detectors labelled.

Proton beams are formed inside the Proton Synchrotron (**PS**) from bunches of protons 50 ns apart with an energy of 26 GeV. The protons are then accelerated in the Super Proton Synchrotron (**SPS**) to 450 GeV before being injected into the **LHC**. These **LHC** proton beams consists of many “bunches” i.e. approximately  $1.1 \times 10^{11}$  protons localized into less than 1 ns in the direction of motion. Before collision the beams are ramped to 4

683

684 TeV (2012) per beam in a process involving increasing the current passing through the  
 685 dipole magnets. Once the desired  $\sqrt{s}$  energy is reached then the beams are allowed to  
 686 collide at the interaction points. The luminosity falls regularly as the run progresses as  
 687 protons are lost in collisions, and eventually the beam is dumped before repeating the  
 688 process again.

689

690 Colliding the beams produced an instantaneous luminosity of approximately  $5 \times$   
 691  $10^{33} \text{ cm}^{-2}\text{s}^{-1}$  during the 2012 run. The high number of protons in each bunch increases  
 692 the likelihood of multiple interactions with each crossing of the counter-circulating  
 693 beams. This leads to isotropic energy depositions within the detectors positioned at these  
 694 interaction points, increasing the energy scale of the underlying event. This is known as  
 695 pile-up and the counteracting of it's effects are important to the many measurements  
 696 performed at the LHC.

697 In the early phase of prolonged operation after the initial shutdown the machine  
 698 operated in 2010-2011 at 3.5 TeV per beam,  $\sqrt{s} = 7 \text{ TeV}$ , delivering  $6.13 \text{ fb}^{-1}$  of data  
 699 [53]. During the 2012-2013 run period, data was collected at an increased  $\sqrt{s} = 8 \text{ TeV}$   
 700 improving the sensitivity of searches for new physics. Over the whole run period  $23.3$   
 701  $\text{fb}^{-1}$  of data was delivered of which  $21.8 \text{ fb}^{-1}$  was recorded by the CMS detector as shown  
 702 in Figure 3.2 [53]. A total of  $12 \text{ fb}^{-1}$  of 8 TeV certified data was collected by October  
 703 2012, and it is this data which forms the basis of the results discussed within this thesis.

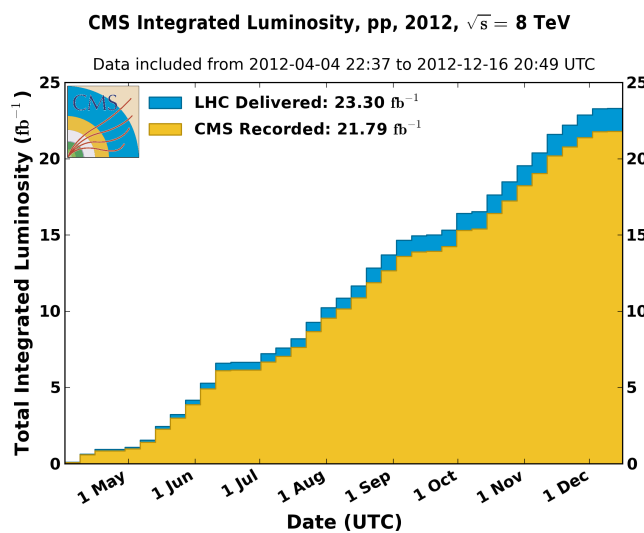


**Figure 3.2.:** The total integrated luminosity delivered to and collected by CMS during the 2012 8 TeV  $pp$  runs.

704 **3.2. The CMS detector**

705 The Compact Muon Solenoid (**CMS**) detector is one of two general purpose detectors  
706 at the **LHC** designed to search for new physics. The detector is designed to provide  
707 efficient identification and measurement of many physics objects including photons,  
708 electrons, muons, taus, and hadronic showers over wide ranges of transverse momentum  
709 and direction. Its nearly  $4\pi$  coverage in solid angle allows for accurate measurement of  
710 global transverse momentum imbalance. These design factors give **CMS** the ability to  
711 search for direct production of **SUSY** particles at the TeV scale, making the search for  
712 Supersymmetric particles one of the highest priorities among the wide range of physics  
713 programmes at **CMS**.

714

715 **CMS** uses a right-handed Cartesian coordinate system with the origin at the interaction  
716 point and the z-axis pointing along the beam axis, the x-axis points radially inwards to  
717 the centre of the collider ring, with the y-axis points vertically upward. The azimuthal  
718 angle,  $\phi$  ranging between  $[-\pi, \pi]$  is defined in the x-y plane starting from the x-axis. The  
719 polar angle  $\theta$  is measured from the z axis. The common convention in particle physics is  
720 to express an out going particle in terms of  $\phi$  and its pseudorapidity defined as

$$\eta = -\log \tan \left( \frac{\theta}{2} \right). \quad (3.1)$$

721 The variable  $\Delta R = \sqrt{\Delta\phi^2 + \Delta\eta^2}$  is commonly used to define angular distance  
722 between objects within the detector and additionally energy and momentum is typically  
723 measured in the transverse plane perpendicular to the beam line. These values are  
724 calculated from the x and y components of the object and are denoted as  $E_T = E \sin \theta$   
725 and  $p_T = \sqrt{p_x^2 + p_y^2}$ .

726 **3.2.1. Detector Subsystems**

727 As the range of particles produced in  $pp$  collisions interact in different ways with mat-  
728 ter, **CMS** is divided into subdetector systems, which perform complementary roles to  
729 identify the identity, mass and momentum of the different physics objects present in  
730 each event. These detector sub-systems contained inside **CMS** are wrapped in layers

731 around a central 13 m long 4 T super conducting solenoid as shown in Figure 3.3. With  
 732 the endcaps closed , CMS is a cylinder of length 22 m, diameter 15 m, and mass 12.5  
 733 kilotons. A more detailed complete description of the detector can be found elsewhere [50].

734

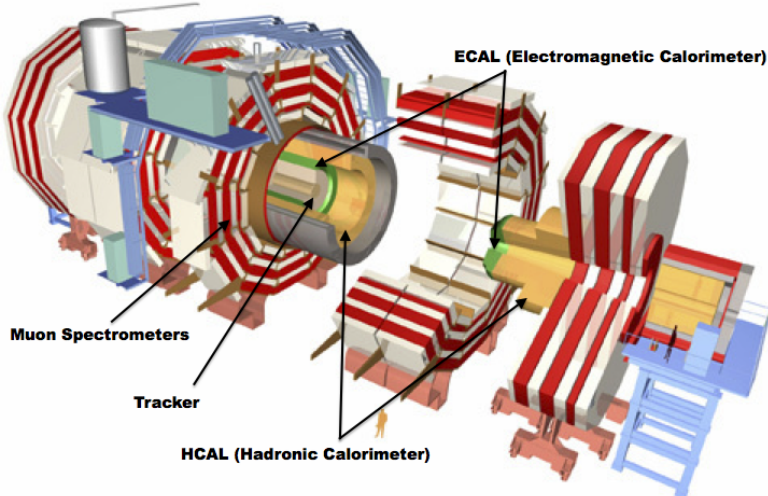


**Figure 3.3.:** A pictorial depiction of the CMS detector with the main detector subsystems labelled. [54]

### 735 3.2.2. Tracker

736 The inner-most subdetector of the barrel is the multi-layer silicon tracker, formed of a  
 737 pixel detector component encased by layers of silicon strip detectors. The pixel detector  
 738 consists of three layers of silicon pixel sensors providing measurements of the momentum,  
 739 position coordinates of the charged particles as they pass, and the location of primary  
 740 and secondary vertices between 4cm and 10cm transverse to the beam. Outside the pixel  
 741 detector, ten cylindrical layers of silicon strip detectors extend the tracking system out to  
 742 a radius of 1.20m from the beam line. The tracking system provides efficient and precise  
 743 determination of the charges, momenta, and impact parameters of charged particles with  
 744 the geometry of the tracker extending to cover a rapidity range up to  $|\eta| < 2.5$ .

745

746 The tracking system also plays a crucial part in the identification of jets originating  
 747 from b-quarks through measurement of displaced secondary vertices, which is covered in  
 748 more detail in Section (3.3.2). The identification of b-jets is important in many searches

749 for natural SUSY models and forms an important part of the inclusive search strategy  
750 described within Section (4.2).

751 **3.2.3. Electromagnetic Calorimeter**

752 Immediately outside of the tracker, but still within the magnet core, sits the Electromag-  
753 netic CALorimeter (**ECAL**). Covering a pseudorapidity up to  $|\eta| < 3$  and comprising  
754 of over 75,000 PbWO<sub>4</sub> (lead tungstate) crystals that scintillate as particles deposit energy,  
755 the **ECAL** provides high resolution measurements of the electromagnetic showers from  
756 photons, electrons in the detector.

757

758 Lead tungstate is used because of its short radiation length ( $X_0 \sim 0.9\text{cm}$ ) and small  
759 Molieré radius ( $\sim 2.1\text{cm}$ ) leading to high granularity and resolution. It's fast scintillation  
760 time ( $\sim 25\text{ns}$ ) reduces the effects of pile-up due to energy from previous collisions still  
761 being read out, and its radiation hardness gives it longevity. The crystals are arranged  
762 in modules which surround the beam line in a non-projective geometry, angled at  $3^\circ$   
763 with respect to the interaction point to minimise the risk of particles escaping down the  
764 cracks between the crystals.

765

766 The **ECAL** is primarily composed of two sections, the Electromagnetic CALorime-  
767 ter Barrel (**EB**) which extends in pseudo-rapidity to  $|\eta| < 1.479$  with a crystal front  
768 cross section of  $22 \times 22\text{ mm}^2$  and a length of 230 mm corresponding to 25.8 radia-  
769 tion lengths, and the Electromagnetic CALorimeter Endcap (**EE**) covering a rapidity  
770 range of  $1.479 < |\eta| < 3.0$ , which consists of two identical detectors on either side of  
771 the **EB**. A lead-silicon sampling ‘pre-shower’ detector Electromagnetic CALorimeter  
772 pre-Shower (**ES**) is placed before the endcaps to aid in the identification of neutral pions.  
773 Their arrangement are shown in Figure 3.4.

774

775 Scintillation photons from the lead tungstate crystals are instrumented with Avalanche  
776 Photo-Diodes (**APD**) and Vacuum Photo-Triodes (**VPT**) located in the **EB** and **EE**  
777 respectively, converting the scintillating light into an electric signal which is consequently  
778 used to determine the amount of energy deposited within the crystal . These instruments  
779 are chosen for their resistance under operation to the strong magnetic field of **CMS**. The  
780 scintillation of the **ECAL** crystals as well as the response of the **APDs** varies as a function

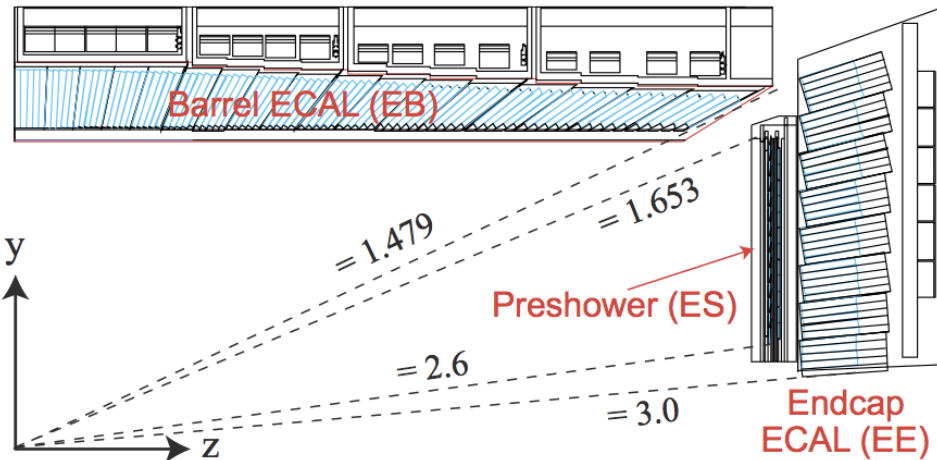


**Figure 3.4.:** Illustration of the **ECAL** showing the arrangement of the lead tungstate crystals in the **EB** and **EE**. The **ES** is also shown and is located in front of the **EE** [55].

781 of temperature and so cooling systems continually maintain an overall constant **ECAL**  
 782 temperature  $\pm 0.05^\circ C$ .

### 783 3.2.4. Hadronic Calorimeter

784 Beyond the **ECAL** lies the Hadronic CALorimeter (**HCAL**) which is responsible for  
 785 the accurate measurement of hadronic showers, crucial for analyses involving jets or  
 786 missing energy signatures. The **HCAL** is a sampling calorimeter which consists of al-  
 787 ternating layers of brass absorber and plastic scintillator, except in the hadron forward  
 788 ( $3.0 < |\eta| < 5.0$ ) region in which steel absorbers and quartz fibre scintillators are used  
 789 because of their increased radiation tolerance. Hadron showers are initiated in the  
 790 absorber layers inducing scintillation in the plastic scintillator tiles. These scintillation  
 791 photons are converted by wavelength shifting fibres for read-out by hybrid photodiodes.  
 792

793 The **HCAL**'s size is constrained to a compact size by the presence of the solenoid,  
 794 requiring the placement of an additional outer calorimeter on the outside of the solenoid  
 795 to increase the sampling depth of the **HCAL**. A schematic of the **HCAL** can be seen in  
 796 Figure 3.5.  
 797

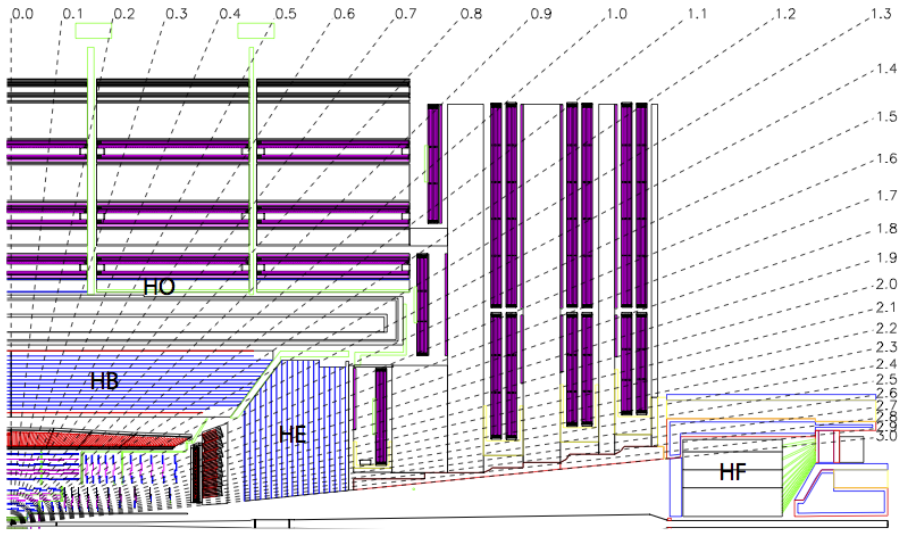


**Figure 3.5.:** Schematic of the hadron calorimeters in the r-z plane, showing the locations of the **HCAL** components and the **HF**. [50].

798     The **HCAL** covers the range  $|\eta| < 5$  and consists of four subdetectors: the Hadron  
 799     Barrel (**HB**)  $|\eta| < 1.3$ , the Hadron Outer (**HO**), the Hadron Endcaps (**HE**)  $1.3 < |\eta| < 3.0$   
 800     and the Hadron Forward (**HF**). The **HB** is contained between the outer edge of the **ECAL**  
 801     and the inner edge of the solenoid, formed of 36 azimuthal wedges it is split between  
 802     two half-barrel segments. Each wedge is segmented into four azimuthal angle ( $\phi$ ) sectors,  
 803     and each half-barrel is further segmented into 16  $\eta$  towers. The electronic readout chain,  
 804     channels the light from the active scintillator layers from one  $\phi$ -segment and all  $\eta$ -towers  
 805     of a half-barrel to a Hybrid Photo Diode (**HPD**).

806     The relatively short number of interaction lengths ( $\lambda_l$ , the distance a hadron will  
 807     travel through the absorber material before it has lost  $\frac{1}{e}$  of its energy) within the **HB**,  
 808     the lowest being  $\lambda_l = 5.82$  for  $|\eta| = 0$ , facilitates the need for the ‘tail catching’ **HO**  
 809     to increase the sampling depth in the central barrel rapidity region  $|\eta| < 1.3$  to 11  
 810     interaction lengths . Significant fractions of the hadrons energy will be deposited in the  
 811     **ECAL** as it passed through the detector. Therefore measurements of hadron energies  
 812     in the central regions  $|\eta| < 3.0$  use both the **ECAL** and **HCAL** to reconstruct the true  
 813     energy from showering hadrons.

814 **3.2.5. Muon Systems**

815 Muons being too massive to radiate away energy via Bremsstrahlung, interact little in  
816 the calorimeters and mostly pass through the detector until they reach the system of  
817 muon detectors which forms the outer most part of the **CMS** detector.

818 Outside of the superconducting solenoid are four muon detection layers interleaved  
819 with the iron return yokes which measure the muons energy via ionisation of gas within  
820 detector elements. Three types of gaseous chamber are used. The Drift Tube (**DT**),  
821 Cathode Stripe Chamber (**CSC**), and Resistive Plate Chamber (**RPC**) systems provide  
822 efficient detection of muons with pseudo-rapidity  $|\eta| < 2.4$ . The best reconstruction  
823 performance is obtained when the muon chamber is combined with the inner tracking  
824 information to determine muon trajectories and their momenta [56].

825

826 **3.3. Event Reconstruction and Object Definition**

827 The goal of event reconstruction is to take the raw information recorded by the detector  
828 and to compute from it higher-level quantities which can be used at an analysis level.  
829 These typically correspond to an individual particle’s energy and momenta, or groups of  
830 particles which shower in a narrow cone and the overall global energy and momentum  
831 balance of the event. The reconstruction of these objects are described in great detail in  
832 [57], however covered below are brief descriptions of those which are most relevant to the  
833 analysis detailed in Chapter 4.

834 **3.3.1. Jets**

835 Quarks and gluons are produced copiously at the LHC in the hard scattering of partons.  
836 As these quarks and gluons fragment, they hadronise and decay into a group of strongly  
837 interactive particles and their decay products. These streams of particles travel in the  
838 same direction, as they have been “boosted” by the momentum of the primary hadron.  
839 These collections of decay products are reconstructed and identified together as a “jet”.

840 At **CMS** jets are reconstructed from energy deposits in the detector using the anti-kt  
841 algorithm [58] with size parameter  $\Delta R = 0.5$ . The anti-kt jet algorithm clusters jets by  
842 defining a distance between hard (high  $p_T$ ) and soft (low  $p_T$ ) particles such that soft

843 particles are preferentially clustered with hard particles before being clustered between  
844 themselves. This produces jets which are robust to soft particle radiation from the pile-up  
845 conditions experienced at the **LHC**.

846

847 There are two main type of jet reconstruction used at **CMS**, Calorimeter (Calo) and  
848 Particle Flow (PF) jets [59]. Calorimeter jets are reconstructed using both the **ECAL**  
849 and **HCAL** cells, combined into calorimeter towers . These calorimeter towers consist of  
850 geometrically matched **HCAL** cells and **ECAL** crystals. Electronics noise is suppressed by  
851 applying a threshold to the calorimeter cells, with pile-up effects reduced by a requirement  
852 placed on the tower energy [60]. Calorimter jets are the jets used within the analyses  
853 described in this thesis.

854 PF jets are formed from combining information from all of the **CMS** subdetectors  
855 systems to determine which final state particles are present in the event. Generally,  
856 any particle is expected to produce some combination of a track in the silicon tracker,  
857 a deposit in the calorimeters, or a track in the muon system. The PF jet momentum  
858 and spatial resolutions are greatly improved with respect to calorimeter jets, as the use  
859 of the tracking detectors and of the high granularity of **ECAL** allows resolution and  
860 measurement of charged hadrons and photons inside a jet, which together constitute  $\sim$   
861 85% of the jet energy [61].

862 The jets reconstructed by the clustering algorithm in **CMS** typically have an energy  
863 that differs to the ‘true’ energy measured by a perfect detector. This stems from the  
864 non-linear and nonuniform response of the calorimeters as well as other residual effects  
865 including pile-up and underlying events, and therefore additional corrections are applied  
866 to recover a uniform relative response as a function of pseudo-rapidity. These are applied  
867 as separate sub corrections [62].

- 868 • A PU correction is first applied to the jet. It subtracts the average extra energy  
869 deposited in the jet that comes from other vertices present in the event and is  
870 therefore not part of the hard jet itself.
- 871 •  $p_T$  and  $\eta$  dependant corrections derived from Monte Carlo simulations are used to  
872 account for the non-uniform response of the detector.
- 873 •  $p_T$  and  $\eta$  residual corrections are applied to data only to correct for difference  
874 between data and Monte Carlo. The residual is derived from QCD dijet samples  
875 and the  $p_T$  residual from  $\gamma+$  jet and  $Z+$  jets samples in data.

---

### 876 3.3.2. B-tagging

877 The decays of b quarks are suppressed by small CKM matrix elements. As a result, the  
 878 lifetimes of b-flavoured hadrons, produced in the fragmentation of b quarks, are relatively  
 879 long;  $\mathcal{O}$  1ps. The identification of jets origination from b quarks is very important for  
 880 searches for new physics and for measurements of standard model processes.

881

882 Many different algorithms developed by CMS select b-quark jets based on variables  
 883 such as the impact parameters of the charged-particle tracks, the properties of recon-  
 884 structed decay vertices, and the presence or absence of a lepton, or combinations thereof  
 885 [63]. One of the most efficient of which is the Combined Secondary Vertex (CSV) which  
 886 operates based on secondary vertex and track-based lifetime information, benchmarked  
 887 in ‘Loose’, ‘Medium’ and ‘Tight’ working points, of which the medium point is the tagger  
 888 used within the  $\alpha_T$  search detailed in Section (4.1).

889 Using the CSV tagger, a likelihood-based discriminator distinguishes between jets  
 890 from b-quarks, and those from charm or light quarks and gluons, which is shown in Figure  
 891 3.6. The minimum thresholds on the discriminator for each working point correspond to  
 892 the misidentification probability for light-parton jets of 10%, 1%, and 0.1%, respectively,  
 893 in jets with an average  $p_T$  of about 80 GeV.

894 The b-tagging performance is evaluated to measure the b-jet tagging efficiency  $\epsilon_b$ ,  
 895 and the misidentification probability of charm  $\epsilon_c$  and light-parton jets  $\epsilon_s$ . The tagging  
 896 efficiencies for each of these three jet flavours are compared between data and MC  
 897 simulation, from which a series of  $p_T$  and  $|\eta|$  binned jet corrections are determined,

$$898 SF_{b,c,s} = \frac{\epsilon_{b,c,s}^{data}}{\epsilon_{b,c,s}^{MC}}. \quad (3.2)$$

899 These are collectively named ‘Btag Scale Factors’ and allow MC simulation to accu-  
 900 rately reflect the running conditions and performance of the tagging algorithm in data.  
 901 Understanding of the b-tagging efficiency is essential in order to minimise systematic  
 902 uncertainties in physics analyses that employ b-tagging.

902

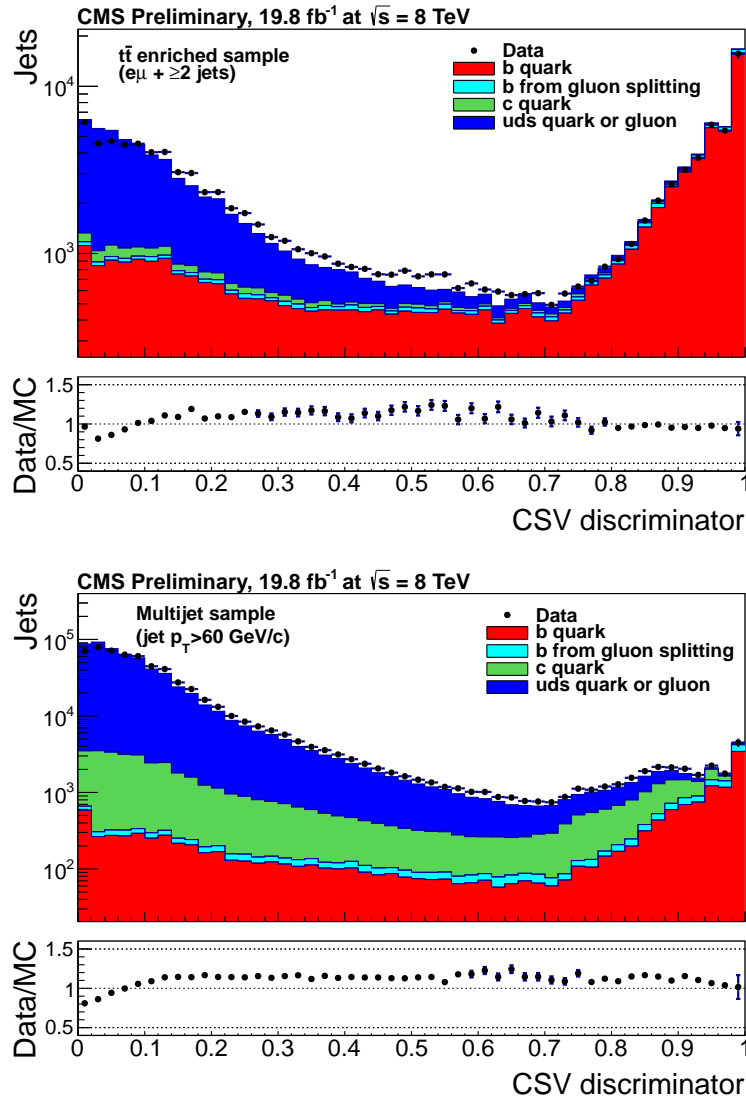


**Figure 3.6.:** CSV algorithm discriminator values in enriched  $t\bar{t}$ bar (top) and inclusive multi jet samples (bottom) for b,c and light flavoured jets [64]. Working points are determined from the misidentification probability for light-parton jets to be tagged as a b-jet and are given as 0.244, 0.679 and 0.898 for L,M and T working points respectively.

903        The b-tagging efficiency is measured in data using several methods applied to multi  
 904        jet events, primarily based on a sample of jets enriched in heavy flavour content. One  
 905        method requires the collection of events with a soft muon within a cone  $\Delta R < 0.4$  around  
 906        the jet axis. Because the semileptonic branching fraction of b hadrons is significantly  
 907        larger than that for other hadrons, these jets are more likely to arise from b quarks than  
 908        from another flavour, with the resultant momentum component of the muon transverse  
 909        to the jet axis larger for muons from b-hadron decays than from light or charm jets.

Additionally the performance of the tagger can also be benchmarked in  $t\bar{t}$  events where in the SM, the top quark is expected to decay to a W boson and a b quark about 99.8% of the time [1]. Further selection criteria is applied to these events to further enrich the b quark content of these events. The methods to identify b-jets in data are discussed in great detail at [65]. The jet flavours are determined in simulation using truth level information and are compared to data to determine the correction scale factors ( $SF_b$ ), which are displayed for the CSVM tagger in Figure 3.7.

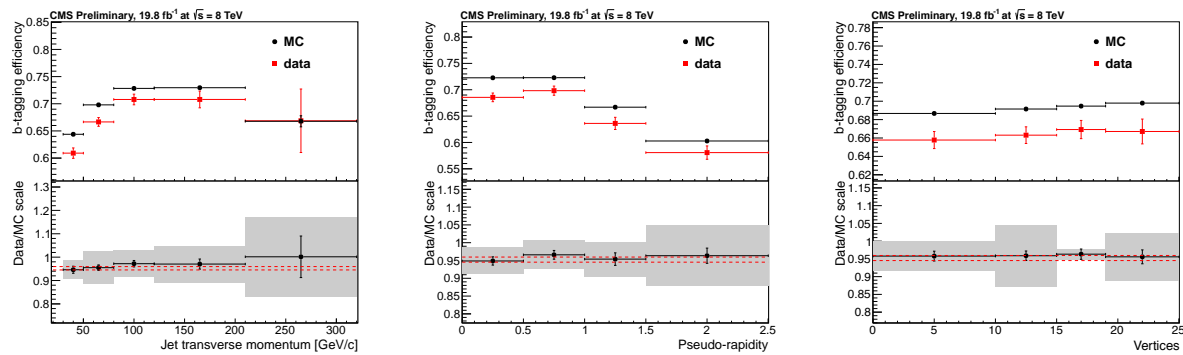


**Figure 3.7.:** Measured in  $t\bar{t} \rightarrow$  di-lepton events using the CSVM tagger: (upper panels) b-tagging efficiencies and (lower panels) data/MC scale factor  $SF_b$  as a function of (left) jet  $p_T$ , (middle) jet  $|\eta|$  and (right) number of primary vertices. In the lower panels, the grey filled areas represent the total statistical and systematic uncertainties, whereas the dotted lines are the average  $SF_b$  values within statistical uncertainties.

The measurement of the misidentification probability for light-parton jets relies on the inversion of tagging algorithms, selecting non-b jets using the same variables and techniques used in benchmarking the b-tagging efficiency. The scale factors ( $SF_s$ ) to be applied to MC are shown in Figure 3.8 for the CSVM tagger.

### 3.4. Triggering System

With bunch crossings separated by just 25 ns, the rate at which data from all collisions would have to be written out and processed would be unfeasible. A two-tiered triggering system is applied at CMS in order to cope with the high collision rate of protons. The CMS trigger is designed to use limited information from each event to determine whether to record the event, reducing the rate of data taking to manageable levels whilst ensuring a high efficiency of interesting physics object events are selected.

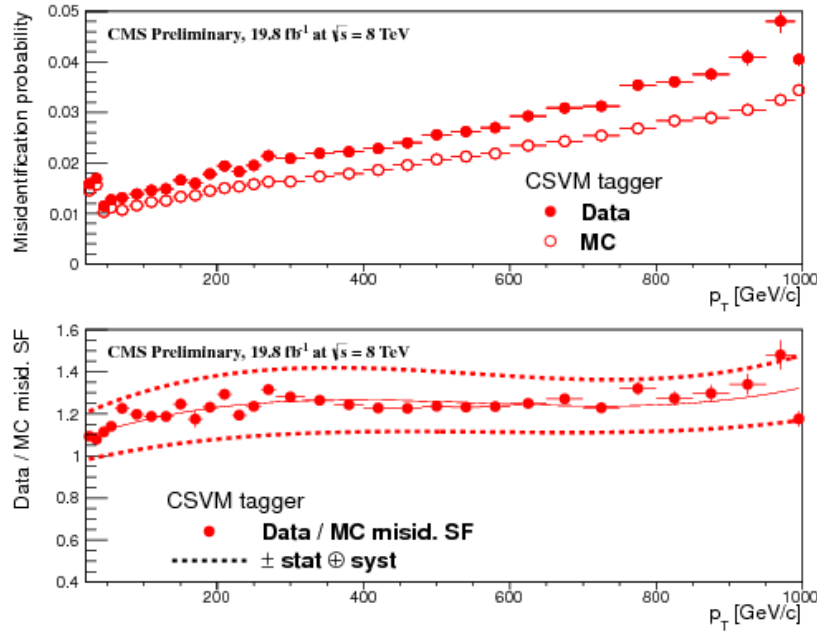


**Figure 3.8.:** For the **CSVM** tagging criterion: (top) misidentification probability in data (filled circles) and simulation (open circles); (bottom) scale factor for the misidentification probability. The last  $p_T$  bin in each plot includes all jets with  $p_T > 1000$  GeV. The solid curve is the result of a polynomial fit to the data points. The dashed curves represent the overall statistical and systematic uncertainties on the measurements.

928        The **L1** is a pipelined, dead-timeless system based on custom-built electronics [66],  
 929        and is a combination of several sub systems which is shown pictorially in Figure 3.9. The  
 930        **L1** system is covered in more detail within the following section along with a description  
 931        of the service work undertaken by the author to benchmark the performance of the **L1**  
 932        calorimeter trigger during the 2012 8 TeV run period.

933        The Higher Level Trigger (**HLT**) is a large farm of commercial computers [67]. The  
 934        **HLT** processes events with software reconstruction algorithms that are more detailed,  
 935        giving performance more similar to the reconstruction used offline. The **HLT** reduces  
 936        the event rate written to disk by a factor of  $\sim 500$  ( $\sim 200$ Hz). The recorded events are  
 937        transferred from **CMS** to the **CERN** computing centre, where event reconstruction is  
 938        performed, and then distributed to **CMS** computing sites around the globe for storage  
 939        and analysis.

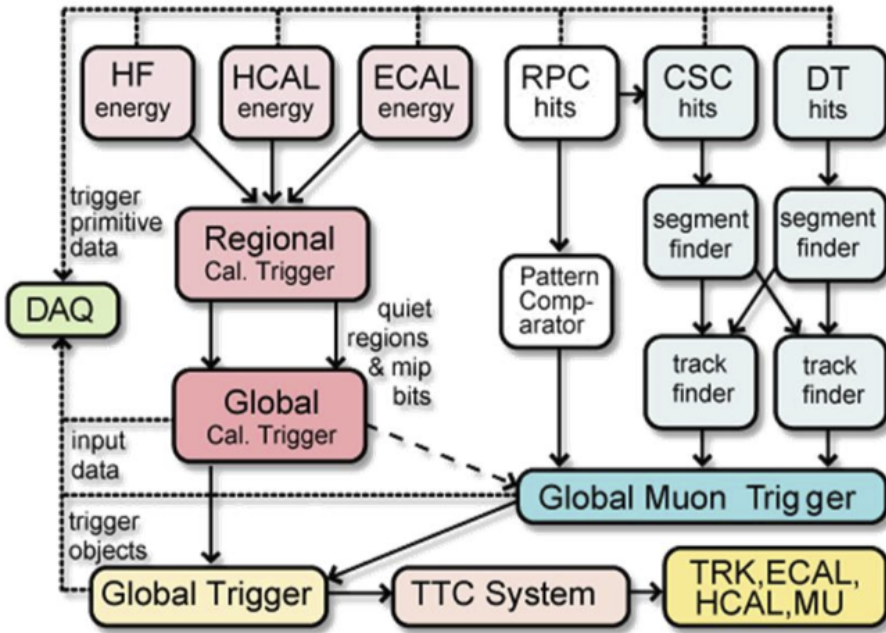


Figure 3.9.: The CMS L1 Trigger system.

### 3.4.1. The Level-1 Trigger

The L1 trigger reduces the rate of events collected from 40 MHz to  $\sim 100$  kHz using information from the calorimeters and muon chambers, but not the tracker. A tree system of triggers is used to decide whether to pass on an event to the HLT for further reconstruction. Firstly the calorimeter and muon event information is kept separate, with local reconstruction of objects ( $\mu, e, \gamma, \text{jets}$ ) performed by the Regional Calorimeter Trigger (RCT) and Regional Muon Trigger (RMT) respectively. The RCT generates up to 72 isolated and non-isolated electromagnetic objects. These are sorted by rank, which is equivalent to transverse energy  $E_T$ , with the four highest ranked electromagnetic objects being passed via the Global Calorimeter Trigger (GCT) and Global MuonTrigger (GMT) to the Global Trigger (GT).

In the L1 GCT, coarse measurements of the energy deposited in the electromagnetic and hadronic calorimeters are combined and by using sophisticated algorithms the following physics objects are formed:

- isolated and non-isolated electromagnetic objects ( $e$  and  $\gamma$ );
- hadronic jets in the central and forward sections of the hadronic calorimeters;

- 956     • hadronically decaying tau leptons;
- 957     • total transverse energy ( $E_T$ ), the scalar sum of the energy measured at L1, and
- 958       missing transverse energy ( $\cancel{E}_T$ ), defined as the vector sum of the energy of L1
- 959       objects;
- 960     • total transverse jet energy ( $H_T$ ), the scalar sum of the energy of all L1 jet objects,
- 961       and missing transverse jet energy ( $\cancel{H}_T$ ), defined as the vector sum of the energy of
- 962       L1 jets, are calculated from uncorrected L1 jets.

963     In addition quantities suitable for triggering minimum bias events, forward physics and  
 964     beam background events are calculated. Additionally relevant muon isolation information  
 965     is also passed on to the **GMT** for decisions involving the muon triggers where it is  
 966     combined with information from across the three muon sub-systems. The resultant final  
 967     accept/reject decision at **L1** is then performed by the **GT** based on the objects received  
 968     from the **GCT** and **GMT** ( $e/\gamma$ ,  $\mu$ , jets,  $E_T$ ,  $\cancel{E}_T$ ,  $H_T$ ).

969     The L1 trigger is therefore of upmost importance to the functioning of the detector.  
 970     Without a high-performing trigger and a good understanding of it's performance, there  
 971     would be no data to analyse. Observations of how the L1 trigger performance is affected  
 972     by changing **LHC** running conditions over the 2012 run period and also the introduction  
 973     of a jet seed threshold to the L1 jet trigger algorithm is presented in the following Sections  
 974     (3.4.2 - 3.4.6).

### 975     3.4.2. L1 Trigger Jet Algorithm

976     The L1 jet trigger uses the transverse energy sums computed in the calorimeter (both  
 977     hadronic and electromagnetic) trigger regions. Each region consists of  $4 \times 4$  trigger tower  
 978     windows, spanning a region of  $\Delta\eta \times \Delta\phi = 0.087 \times 0.087$  in pseudorapidity-azimuth. The  
 979     jet trigger uses a  $3 \times 3$  calorimeter region (112 trigger towers) sliding window technique  
 980     which spans the full  $(\eta, \phi)$  coverage of the **CMS** calorimeter as shown in Figure 3.10.

981     In forming a L1 jet is it required that the central region to be higher than the eight  
 982     neighbouring regions  $E_{T\text{central}} > E_{T\text{surround}}$ . Additionally a minimum threshold of 5 GeV  
 983     on  $E_{T\text{central}}$  was introduced during the 2012 run period to suppress noise from pile-up,  
 984     the effects of which are shown in Section (3.4.4).

985     The L1 jets are characterised by the  $E_T$ , summed over the  $3 \times 3$  calorimeter regions,  
 986     which corresponds to  $12 \times 12$  trigger towers in barrel and endcap or  $3 \times 3$  larger **HF**

987 towers in the **HF**. The  $\phi$  size of the jet window is the same everywhere, whilst the  $\eta$   
988 binning gets somewhat larger at high  $\eta$  due to calorimeter and trigger tower segmentation.  
989 The jets are labelled by  $(\eta, \phi)$  indexes of the central calorimeter region.

990 Jets with  $|\eta| > 3.0$  are classified as forward jets, whereas those with  $|\eta| < 3.0$  are  
991 classified as central. The four highest energy central, forward and  $\tau$  jets in the calorimeter  
992 are passed through Look Up Table (**LUT**)'s, which apply a programmable  $\eta$ -dependent  
993 jet energy scale correction. These are then used to make L1 trigger decisions.

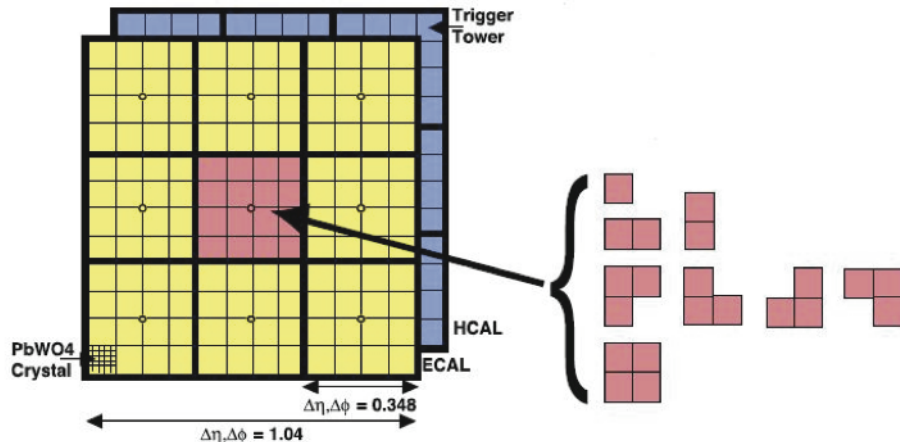


**Figure 3.10.:** Illustration of the Level-1 jet finding algorithm.

994 The performance of the L1 jets is evaluated with respect to offline jets, which are  
995 taken from the standard Calo jet and the PF jet reconstruction algorithms of **CMS**.  
996 Jets are corrected for pile-up and detector effects as described in [3.3.1](#). A moderate  
997 level of noise rejection is applied to the offline jets by selecting jets passing the “loose  
998 identification criteria for both Calo and PF. These criteria are summarised in Appendix  
999 [\(A\)](#).

### 1000 3.4.3. Measuring L1 Jet Trigger Efficiencies

1001 The L1 jet efficiency is defined as the fraction of leading offline jets which were matched  
1002 with a L1 tau or central jet above a certain trigger threshold, divided by all the leading  
1003 offline jets in the event. This quantity is then plotted as a function of the offline jet  $E_T$ ,  
1004  $\eta$  and  $\phi$ .

1005 The efficiency is determined by matching the L1 and reconstructed offline jets spatially  
1006 in  $\eta - \phi$  space. This is done by calculating the minimum separation in  $\Delta R$  between the

Trigger	Calo		PF	
	$\mu$	$\sigma$	$\mu$	$\sigma$
L1_SingleJet16	21.09 $\pm$ 0.03	7.01 $\pm$ 0.02	22.17 $\pm$ 0.04	7.83 $\pm$ 0.03
L1_SingleJet36	41.15 $\pm$ 0.05	5.11 $\pm$ 0.02	39.16 $\pm$ 0.06	8.04 $\pm$ 0.03
L1_SingleJet92	95.36 $\pm$ 0.13	5.62 $\pm$ 0.03	90.85 $\pm$ 0.19	11.30 $\pm$ 0.10

**Table 3.1.:** Results of a cumulative [EMG](#) function fit to the turn-on curves for L1 single jet triggers in run 2012 Run Period C, measured in an isolated  $\mu$  data sample. The turn-on point,  $\mu$ , and resolution,  $\sigma$ , of the L1 jet triggers are measured with respect to offline Calo Jets (left) and PF Jets (right).

highest offline reconstructed jet in  $E_T$  ( $E_T > 10$  GeV,  $|\eta| < 3$ ) and any L1 jet. A jet will be matched if this value is found to be  $< 0.5$ . Should more than one jet satisfy this, the jet closest in  $\Delta R$  is taken as the matched jet. The matching efficiency is close to 100%, above ? 30(45) GeV for run 2012B(C) data (see Appendix (??)).

Each efficiency curve is fitted with a function which is the cumulative distribution function of an Exponentially Modified Gaussian ([EMG](#)) distribution:

$$f(x; \mu, \sigma, \lambda) = \frac{\lambda}{2} \cdot e^{\frac{\lambda}{2}(2\mu + \lambda\sigma^2 - 2x)} \cdot \text{erfc}\left(\frac{\mu + \lambda\sigma^2 - x}{\sqrt{2}\sigma}\right) \quad (3.3)$$

where erfc is the complementary error function defined as:

$$\text{erfc}(x) = 1 - \text{erf}(x) = \frac{2}{\sqrt{\pi}} \int_x^\infty e^{-t^2} dt.$$

In this functional form, the parameter  $\mu$  determines the point of 50% of the plateau efficiency and the  $\sigma$  gives the resolution. This parametrisation is used to benchmark the efficiency at the plateau, the turn-on points and resolution for each L1 Jet trigger. The choice of function is purely empirical. Previous studies used the error function alone, which described the data well at high threshold values but could not describe the efficiencies well at lower thresholds [68].

The efficiency turn-on curves for various L1 jet thresholds are evaluated as a function of the offline reconstructed jet  $E_T$  for central jets with  $|\eta| < 3$ . These are measured using single isolated  $\mu$  triggers which have high statistics, and are orthogonal and therefore unbiased to the hadronic triggers under study. The efficiency is calculated with respect to offline Calo and PF Jets in Figure 3.11. Table 3.1 shows the values of these parameters, calculated for three example L1 single jet triggers taken from 2012 8 TeV data.

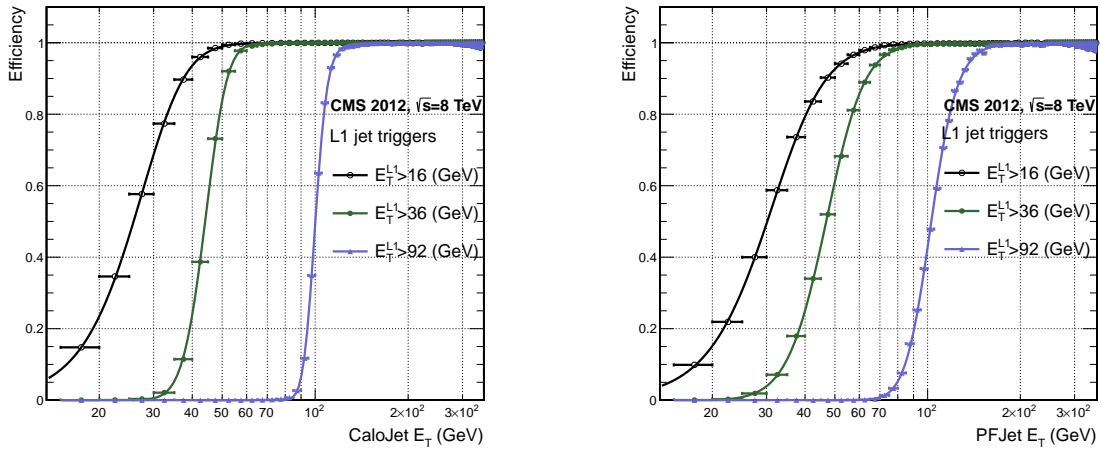


**Figure 3.11.:** L1 jet efficiency turn-on curves as a function of the offline CaloJet  $E_T$  (left) and PFJet  $E_T$  (right), measured in 2012 Run Period C data and collected with an isolated single  $\mu$  data sample.

1026        The results from the L1 single jet triggers shows good performance for both Calo and  
 1027        PF jets. A better resolution for Calo jets with respect to L1 jets quantities is observed.  
 1028        This effect is due to Calo jet reconstruction using the same detector systems as in L1 jets,  
 1029        whereas with PF jet construction using tracker and muon information, a more smeared  
 1030        resolution when compared to L1 is expected.

### 1031        3.4.4. Effects of the L1 Jet Seed

1032        Between run period B and C of the 2012 data taking period, a jet seed threshold was  
 1033        introduced into the L1 trigger jet algorithm. There was previously no direct requirement  
 1034        made on the energy deposited in the central region. The introduction of a jet seed  
 1035        threshold required that the central region have  $E_T \geq 5$  GeV, and was introduced to  
 1036        counteract the effects of high pile up running conditions which create a large number of  
 1037        soft non-collimated jets, that are then added to the jets from the primary interaction or  
 1038        other soft jets from other secondary interactions [69]. This in turn causes a large increase  
 1039        in trigger rate due to the increase in the likelihood that the event causes the L1 trigger to  
 1040        fire. This was implemented to maintain trigger thresholds by cutting the rate of events  
 1041        recorded without significant reduction in the efficiency of physics events of interest.

1042        The effect of the introduction of this jet seed threshold between these two run periods  
 1043        is benchmarked through a comparison of the efficiency of the L1 jet triggers with respect

1044 to offline Calo jets shown in Figure 3.12, and the L1  $H_T$  trigger efficiency in Figure 3.14  
1045 which is compared to offline  $H_T$  constructed from Calo jets with  $E_T \geq 40\text{GeV}$ .

1046 To negate any effects from different pile-up conditions in the run periods, the efficiencies  
1047 are measured in events which contain between 15 and 20 primary vertices as defined in  
1048 Appendix (A.2).

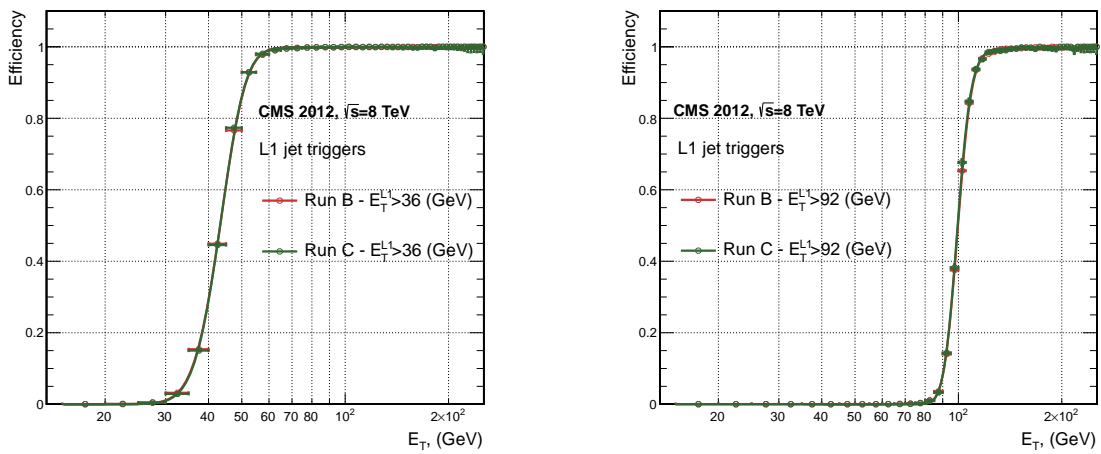


**Figure 3.12.:** L1 jet efficiency turn-on curves as a function of the offline CaloJet  $E_T$ , measured for the L1 SingleJet 36 and 92 trigger in 2012 run period B and C collected with an isolated single  $\mu'$  sample.

1049 It can be seen that the performance of the  $E_T > 36, 92$  single jet are almost identical,  
1050 with the jet seed having no measurable effect on these triggers as shown in Table 3.2 .

Trigger	2012B		2012C	
	$\mu$	$\sigma$	$\mu$	$\sigma$
L1_SingleJet36	$40.29 \pm 0.04$	$5.34 \pm 0.02$	$40.29 \pm 0.11$	$5.21 \pm 0.05$
L1_SingleJet92	$94.99 \pm 0.09$	$5.93 \pm 0.06$	$94.82 \pm 0.29$	$5.74 \pm 0.18$

**Table 3.2.:** Results of a cumulative EMG function fit to the turn-on curves for L1 single jet triggers in the 2012 run period B and C, preselected on an isolated muon trigger. The turn-on point  $\mu$  and resolution  $\sigma$  of the L1 jet triggers are measured with respect to offline Calo Jets in run B (left) and run C (right).

1051 For the  $H_T$  triggers, a large increase in rate during high pile-up conditions is expected.  
1052 This is due to the low energy threshold required for a jet to be added to the L1  $H_T$  sum,  
1053 which is compiled from all uncorrected L1 jets formed in the RCT. The introduction  
1054 of the jet seed threshold removes the creation of many of these soft low  $E_T$  jets, thus

lowering the  $H_T$  calculation at L1. The effect on the trigger cross section for L1  $H_T$  150 trigger can be seen in Figure 3.13.

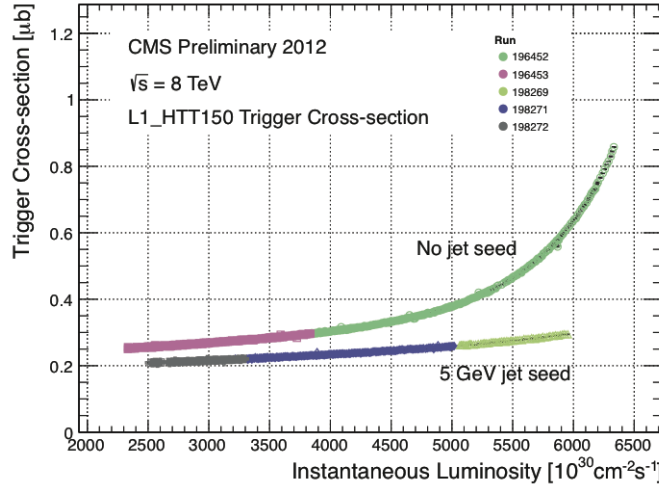


**Figure 3.13.:** Trigger cross section for the L1HTT150 trigger path. Showing that a 5 GeV jet seed threshold dramatically reduces the dependance of cross section on the instantaneous luminosity for L1  $H_T$  triggers [70].

Different behaviours for the trigger turn ons between these run periods are therefore expected. The turn on point is observed to shift to higher  $H_T$  values after the introduction of the jet seed threshold, whilst having a sharper resolution due to less pile-up jets being included the  $H_T$  sum, the results are shown in Table 3.3.

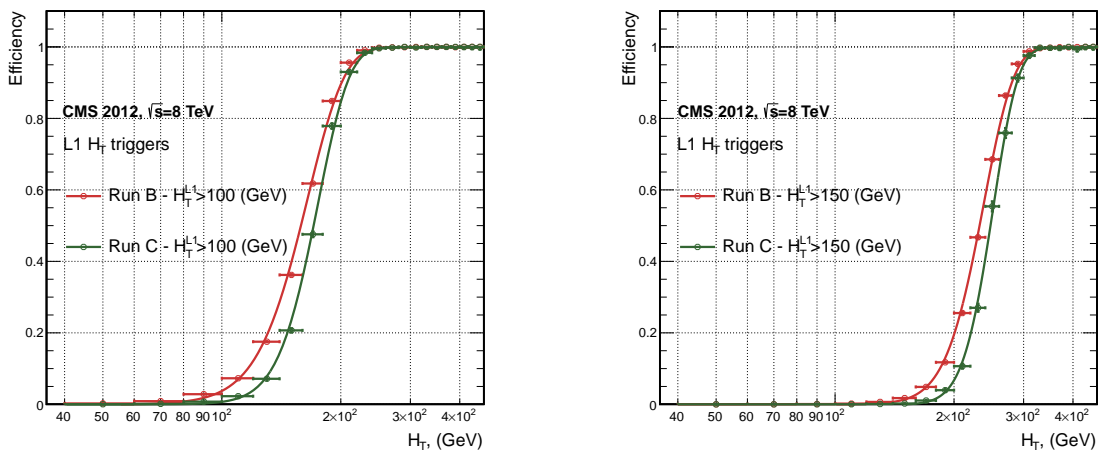


**Figure 3.14.:** L1  $H_T$  efficiency turn-on curves as a function of the offline CaloJet  $H_T$ , measured for the L1  $H_T$  100 and 150 trigger during the run 2012 B and C collected using an isolated single  $\mu$  triggered sample.

Trigger	2012B		2012C	
	$\mu$	$\sigma$	$\mu$	$\sigma$
L1 HT-100	$157.5 \pm 0.08$	$32.9 \pm 0.08$	$169.8 \pm 0.08$	$28.7 \pm 0.03$
L1 H1-150	$230.9 \pm 0.02$	$37.3 \pm 0.01$	$246.4 \pm 0.16$	$31.8 \pm 0.05$

**Table 3.3.:** Results of a cumulative EMG function fit to the turn-on curves for  $H_T$  in run 2012 B and C, preselected on an isolated single  $\mu$  trigger. The turn-on point  $\mu$ , resolution  $\sigma$  of the L1  $H_T$  triggers are measured with respect to offline  $H_T$  formed from CaloJets with a  $E_T \geq 40$  in run period B (left) and C (right).

### 1061 3.4.5. Robustness of L1 Jet Performance against Pile-up

1062 The performance of the L1 single jet triggers is evaluated in different pile-up conditions  
 1063 to benchmark any dependence on pile-up. Three different pile-up bins of 0-10, 10-20 and  
 1064 >20 vertices are defined, reflecting the low, medium and high pile-up running conditions  
 1065 at CMS in 2012. This is benchmarked relative to Calo and PF jets for the run 2012 C  
 1066 period where the jet seed threshold is applied, with L1 single jet thresholds of 16, 36 and  
 1067 92 GeV, shown in Figure 3.15. The results of fits to these efficiency turn-on curves are  
 1068 given in Table 3.4 and Table 3.5 for Calo and PF jets respectively.

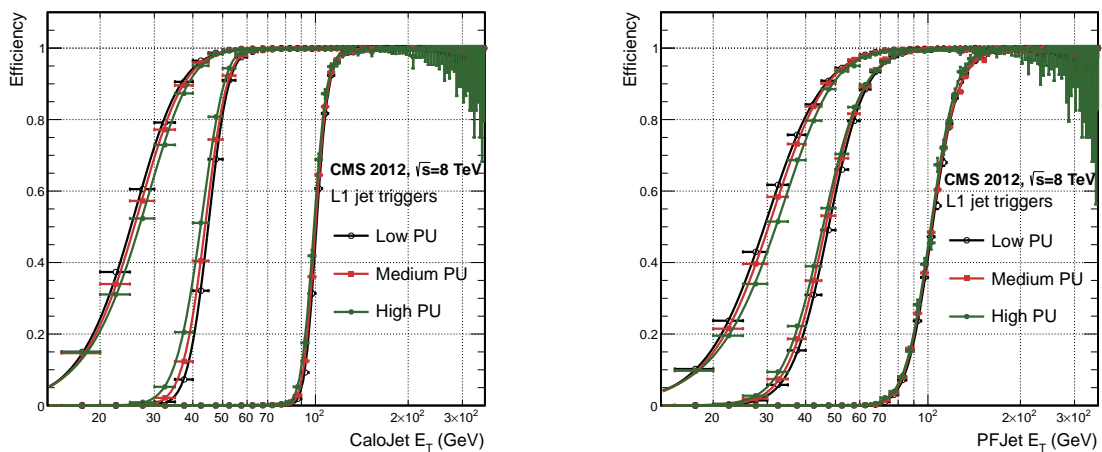


**Figure 3.15.:** L1 jet efficiency turn-on curves as a function of the leading offline  $E_T$ Calo (left) and PF (right) jet, for low, medium and high pile-up conditions.

1069 No significant drop in efficiency is observed in the presence of a high number of  
 1070 primary vertices. The increase in hadronic activity in higher pile-up conditions, combined  
 1071 with the absence of pile-up subtraction for L1 jets, results in the expected observation of  
 1072 a decrease in the  $\mu$  value of the efficiency turn-ons as a function of pile-up, while the

Vertices	0-10		11-20		> 20	
	$\mu$	$\sigma$	$\mu$	$\sigma$	$\mu$	$\sigma$
L1_SingleJet16	19.9 $\pm$ 0.1	6.1 $\pm$ 0.3	20.8 $\pm$ 0.1	6.5 $\pm$ 0.1	22.3 $\pm$ 0.2	7.5 $\pm$ 0.1
L1_SingleJet36	41.8 $\pm$ 0.1	4.6 $\pm$ 0.1	40.9 $\pm$ 0.1	5.1 $\pm$ 0.1	40.6 $\pm$ 0.6	5.9 $\pm$ 0.2
L1_SingleJet92	95.9 $\pm$ 0.2	5.4 $\pm$ 0.1	95.2 $\pm$ 0.2	5.6 $\pm$ 0.1	94.5 $\pm$ 0.6	6.2 $\pm$ 0.3

**Table 3.4.:** Results of a cumulative **EMG** function fit to the efficiency turn-on curves for L1 single jet triggers in the 2012 run period C, measured from isolated  $\mu$  triggered data. The turn-on point,  $\mu$ , and resolution,  $\sigma$ , of the L1 jet triggers are measured with respect to offline Calo jets in low (left), medium (middle) and high (right) pile-up conditions.

Vertices	0-10		11-20		> 20	
	$\mu$	$\sigma$	$\mu$	$\sigma$	$\mu$	$\sigma$
L1_SingleJet16	21.1 $\pm$ 0.1	7.16 $\pm$ 0.05	22.34 $\pm$ 0.1	7.9 $\pm$ 0.1	24.6 $\pm$ 0.2	9.5 $\pm$ 0.1
L1_SingleJet36	39.6 $\pm$ 0.1	7.4 $\pm$ 0.1	38.4 $\pm$ 0.1	7.4 $\pm$ 0.1	37.1 $\pm$ 0.2	7.5 $\pm$ 0.1
L1_SingleJet92	91.6 $\pm$ 0.3	11.3 $\pm$ 0.2	90.4 $\pm$ 0.3	11.2 $\pm$ 0.1	92.0 $\pm$ 0.9	12.1 $\pm$ 0.4

**Table 3.5.:** Results of a cumulative **EMG** function fit to the efficiency turn-on curves for Level-1 single jet triggers in the 2012 run period C, measured from isolated  $\mu$  triggered data. The turn-on point,  $\mu$ , and resolution,  $\sigma$ , of the L1 jet triggers are measured with respect to offline PF jets in low (left), medium (middle) and high (right) pile-up conditions.

1073 resolution,  $\sigma$  of the turn-ons are found to gradually worsen as expected with increasing  
1074 pile-up.

1075 These features are further emphasised when shown as a function of

$$\frac{(L1 E_T - \text{Offline } E_T)}{\text{Offline } E_T} \quad (3.4)$$

1076 in bins of matched leading offline jet  $E_T$ , of which the individual fits can be found in  
1077 Appendix (B.2). Each of these distributions are fitted with an **EMG** function as defined  
1078 in Equation (3.3).

1079 The  $\mu$ ,  $\sigma$  and  $\lambda$  values extracted for the low, medium and high pile-up conditions are  
1080 shown for Calo and PF jets in Figure 3.16 and Figure 3.17 respectively. The central value  
1081 of  $\frac{(L1 E_T - \text{Offline } E_T)}{\text{Offline } E_T}$  is observed to increases as a function of jet  $E_T$ , whilst the resolution  
1082 is also observed to improve at higher offline jet  $E_T$ .

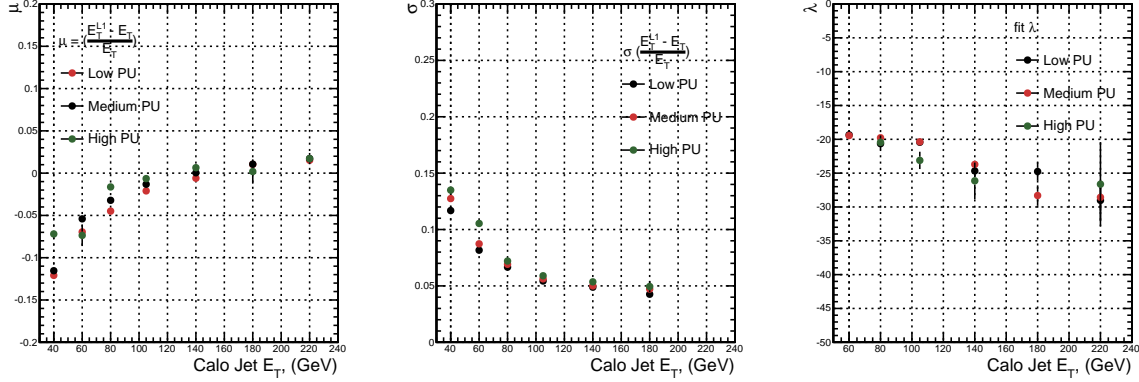


**Figure 3.16.:** Fit values from an EMG function fitted to the resolution plots of leading Calo jet  $E_T$  measured as a function of  $\frac{(L1 E_T - \text{Offline } E_T)}{\text{Offline } E_T}$  for low, medium and high pile-up conditions. The plots show the mean  $\mu$  (left), resolution  $\sigma$  (middle) of the Gaussian as well as the decay term  $\lambda$  (right) of the exponential.

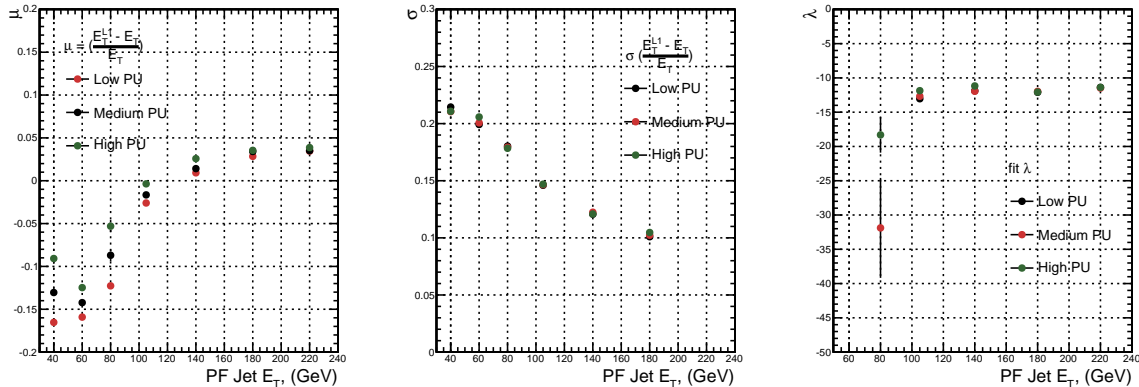


**Figure 3.17.:** Fit values from an EMG function fitted to the resolution plots of leading PF jet  $E_T$  measured as a function of  $\frac{(L1 E_T - \text{Offline } E_T)}{\text{Offline } E_T}$  for low and medium pile-up conditions. The plots show the mean  $\mu$  (left), resolution  $\sigma$  (middle) of the Gaussian as well as the decay term  $\lambda$  (right) of the exponential.

1083      The resolution of other L1 energy sum quantities,  $H_T$ ,  $Z_T$  and  $\sum E_T$  parameterised  
 1084      as in Equation (3.4), can be found in Appendix (B.3). The same behaviour observed for  
 1085      the single jet triggers is also found for these quantities, where in the presence of higher  
 1086      pile-up the  $\mu$  values are shifted to higher values, with a worsening resolution,  $\sigma$  again  
 1087      due to the increase in soft pile-up jets and the absence of pile-up subtraction at L1.

**1088 3.4.6. Summary**

1089 The performance of the CMS Level-1 Trigger has been studied and evaluated for jets and  
1090 energy sum quantities using data collected during the 2012 LHC 8TeV run. These studies  
1091 include the effect of introduction of a 5 GeV jet seed threshold into the jet algorithm  
1092 configuration, the purpose of which is to mitigate the effects of pile-up on the rate of  
1093 L1 triggers whilst not adversely affecting the efficiency of these triggers. No significant  
1094 change in performance is observed with this change and good performance is observed  
1095 for a range of L1 quantities.

# Chapter 4.

## <sup>1096</sup> SUSY searches in Hadronic Final

### <sup>1097</sup> States

<sup>1098</sup> In this chapter a model independent search for **SUSY** in hadronic final states with  $\cancel{E}_T$   
<sup>1099</sup> using the  $\alpha_T$  variable and b-quark multiplicity is introduced and described in detail. The  
<sup>1100</sup> results presented are based on a data sample of pp collisions collected in 2012 at  $\sqrt{s} = 8$   
<sup>1101</sup> TeV, corresponding to an integrate luminosity of  $11.7 \pm 0.5 \text{ fb}^{-1}$ .

<sup>1102</sup> The kinematic variable  $\alpha_T$  is motivated as a variable to provide strong rejections  
<sup>1103</sup> of QCD backgrounds, whilst maintaining sensitivity to possible a **SUSY** signal within  
<sup>1104</sup> Section (4.1). The search and trigger strategy in addition to the event reconstruction  
<sup>1105</sup> and selection are outlined within Sections (4.2-4.3).

<sup>1106</sup> The method in which the **SM** background is estimated using an analytical technique  
<sup>1107</sup> to improve statistical precision at higher b-tag multiplicities is detailed within Section  
<sup>1108</sup> (4.5), with a discussion on the impact of b-tagging and mis-tagging scale factors between  
<sup>1109</sup> data and MC on any background predictions. Finally a description of the formulation of  
<sup>1110</sup> appropriate systematic uncertainties applied to the background predictions to account for  
<sup>1111</sup> theoretical uncertainties and limitations in the simulation modelling of event kinematics  
<sup>1112</sup> and instrumental effects is covered in Section (4.6).

<sup>1113</sup> The experimental reach of the analysis discussed within this thesis is interpreted in  
<sup>1114</sup> two classes of **SMS** models, the topologies of which are detailed in Section (2.4.1). The  
<sup>1115</sup> **SMS** models considered in this analysis are summaries in Table 4.1. For each model, the  
<sup>1116</sup> **LSP** is assumed to be the lightest neutralino.

<sup>1117</sup> Within Table 4.1 is also defined reference points, parameterised in terms of parent  
<sup>1118</sup> gluino/squark and **LSP** sparticle masses,  $m_{parent}$  and  $m_{LSP}$ , respectively, which are used

<sub>1119</sub> within the following two chapters to demonstrate potential yields within the signal region  
<sub>1120</sub> of the search. The masses are chosen to reflect parameter space which is within the  
<sub>1121</sub> expect sensitivity reach of the search.

Model	Production/decay mode	Reference model	
		$m_{parent}$	$m_{LSP}$
G1 (T1)	$pp \rightarrow \tilde{g}\tilde{g}^* \rightarrow q\bar{q}\tilde{\chi}_1^0 q\bar{q}\tilde{\chi}_1^0$	700	300
G2 (T1bb)	$pp \rightarrow \tilde{g}\tilde{g}^* \rightarrow b\bar{b}\tilde{\chi}_1^0 b\bar{b}\tilde{\chi}_1^0$	900	500
G3 (T1tt)	$pp \rightarrow \tilde{g}\tilde{g}^* \rightarrow t\bar{t}\tilde{\chi}_1^0 t\bar{t}\tilde{\chi}_1^0$	850	250
D1 (T2)	$pp \rightarrow \tilde{q}\tilde{q}^* \rightarrow q\tilde{\chi}_1^0 q\tilde{\chi}_1^0$	600	250
D2 (T2bb)	$pp \rightarrow \tilde{b}\tilde{b}^* \rightarrow b\tilde{\chi}_1^0 b\tilde{\chi}_1^0$	500	150
D3 (T2tt)	$pp \rightarrow \tilde{t}\tilde{t}^* \rightarrow t\tilde{\chi}_1^0 t\tilde{\chi}_1^0$	400	0

**Table 4.1.:** A summary of the **SMS** models interpreted in this analysis, involving both direct (D) and gluino-induced (G) production of squarks and their decays. Reference models are also defined in terms of parent and **LSP** sparticle mass

## <sub>1122</sub> 4.1. An introduction to the $\alpha_T$ search

<sub>1123</sub> The experimental signature of **SUSY** signal in the hadronic channel would manifest as a  
<sub>1124</sub> final state containing energetic jets and  $\cancel{E}_T$ . The search focuses on topologies where new  
<sub>1125</sub> heavy supersymmetric, R-parity conserving particles are pair-produced in pp collisions.  
<sub>1126</sub> These particles decaying to a **LSP** escape the detector undetected, leading to significant  
<sub>1127</sub> missing energy and missing hadronic transverse energy,

$$\cancel{H}_T = \left| \sum_{i=1}^n p_T^{jet_i} \right|, \quad (4.1)$$

<sub>1128</sub> defined as the vector sum of the transverse energies of jets selected in an event.  
<sub>1129</sub> Energetic jets produced in the decay of these supersymmetric particles also can produce  
<sub>1130</sub> significant visible transverse energy,

$$H_T = \sum_{i=1}^n E_T^{jet_i}, \quad (4.2)$$

1131 defined as the scalar sum of the transverse energies of jets selected in an event.

1132 A search within this channel is greatly complicated in a hadron collider environment,  
1133 where the overwhelming background comes from inherently balanced multi-jet (“QCD”)  
1134 events which are produced with an extremely large cross section as demonstrated within  
1135 Figure 4.1.  $\cancel{E}_T$  can appear in such events with a substantial mis-measurement of jet  
1136 energy or missed objects due to detector miscalibration or noise effects.

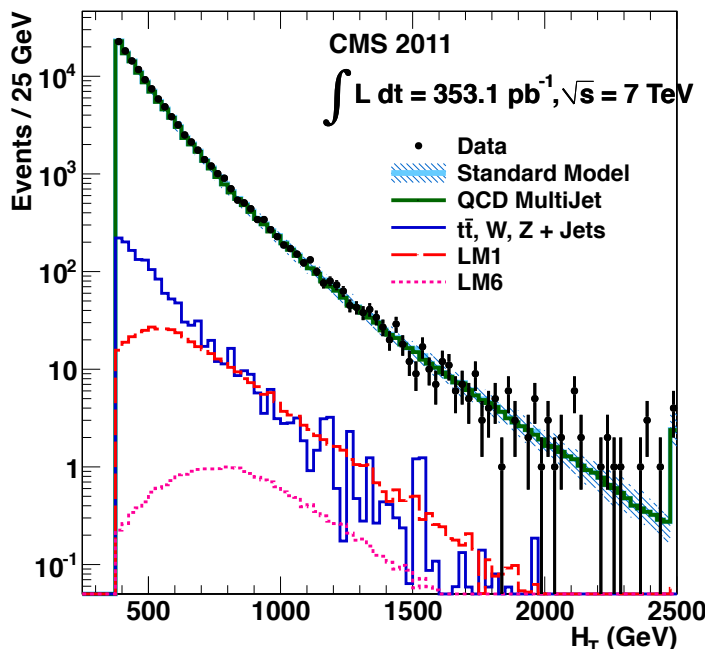


**Figure 4.1.:** Reconstructed offline  $H_T$  for  $11.7\text{fb}^{-1}$  of data after a basic pre-selection. Sample is collected from prescaled  $H_T$  triggers. Overlaid are expectations from MC simulation of EWK processes as well as a reference signal model (labelled D2 from Table 4.1).

1137 Additional SM background from EWK processes with genuine  $\cancel{E}_T$  from escaping  
1138 neutrinos comprise the irreducible background within this search and come mainly from:

- 1139 •  $Z \rightarrow \nu\bar{\nu} + \text{jets}$ ,
- 1140 •  $W \rightarrow l\nu + \text{jets}$  in which a lepton falls outside of detector acceptance, or the lepton  
1141 decays hadronically  $\tau \rightarrow \text{had}$ ,
- 1142 •  $t\bar{t}$  with at least one leptonic W decay,
- 1143 • small background contributions from DY, single top and Diboson (WW,ZZ,WZ)  
1144 processes.

<sub>1145</sub> The search is designed to have a strong separation between events with genuine and  
<sub>1146</sub> “fake”  $\cancel{E}_T$  which is achieved primarily through the dimensionless kinematic variable,  $\alpha_T$   
<sub>1147</sub> [71][72].

### <sub>1148</sub> 4.1.1. The $\alpha_T$ variable

<sub>1149</sub> For a perfectly measured di-jet QCD event, conservation laws dictate that they must be  
<sub>1150</sub> produced back-to-back and of equal magnitude. However in di-jet events with real  $\cancel{E}_T$ ,  
 both of these jets are produced independently of one another, depicted in Figure 4.2.

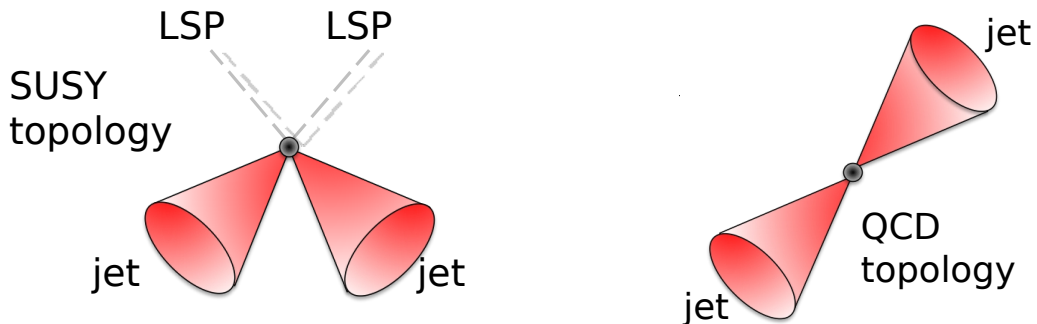


**Figure 4.2.:** The event topologies of background QCD dijet events (right) and a generic SUSY signature with genuine  $\cancel{E}_T$  (left).

<sub>1151</sub>

<sub>1152</sub> Exploiting this feature leads to the formulation of  $\alpha_T$  in di-jet systems defined as,

$$\alpha_T = \frac{E_T^{j2}}{M_T}, \quad (4.3)$$

<sub>1153</sub> where  $E_T^{j2}$  is the transverse energy of the least energetic of the two jets and  $M_T$   
<sub>1154</sub> defined as:

$$M_T = \sqrt{\left(\sum_{i=1}^2 E_T^{ji}\right)^2 - \left(\sum_{i=1}^2 p_x^{ji}\right)^2 - \left(\sum_{i=1}^2 p_y^{ji}\right)^2} \equiv \sqrt{H_T^2 - \cancel{H}_T^2}. \quad (4.4)$$

1155 A perfectly balanced di-jet event i.e.  $E_T^{j_1} = E_T^{j_2}$  would give an  $\alpha_T = 0.5$ , where as  
 1156 events with jets which are not back-to-back, for example in events in which a W or Z  
 1157 recoils off a system of jets,  $\alpha_T$  can achieve values in excess of 0.5.

1158  $\alpha_T$  can be extended to apply to any arbitrary number of jets, undertaken by modelling  
 1159 a system of  $n$  jets as a di-jet system, through the formation of two pseudo-jets [73].  
 1160 The two pseudo-jets are built by merging the jets present in the event such that the 2  
 1161 pseudo-jets are chosen to be as balanced as possible, i.e the  $\Delta H_T \equiv |E_T^{pj_1} - E_T^{pj_2}|$  is  
 1162 minimised between the two pseudo jets. Using Equation (4.4),  $\alpha_T$  can be rewritten as,

$$\alpha_T = \frac{1}{2} \frac{H_T - \Delta H_T}{\sqrt{H_T^2 - \Delta H_T^2}} = \frac{1}{2} \frac{1 - \Delta H_T/H_T}{\sqrt{1 - (\Delta H_T/H_T)^2}}. \quad (4.5)$$

1163 The distribution of  $\alpha_T$  for the two jet categories used within this analysis, 2,3 and  
 1164  $\geq 4$  jets, is shown in the Figure 4.3, demonstrating the ability of the  $\alpha_T$  variable to  
 1165 discriminate between multi jet events and EWK processes with genuine  $\cancel{E}_T$  in the final  
 1166 state.

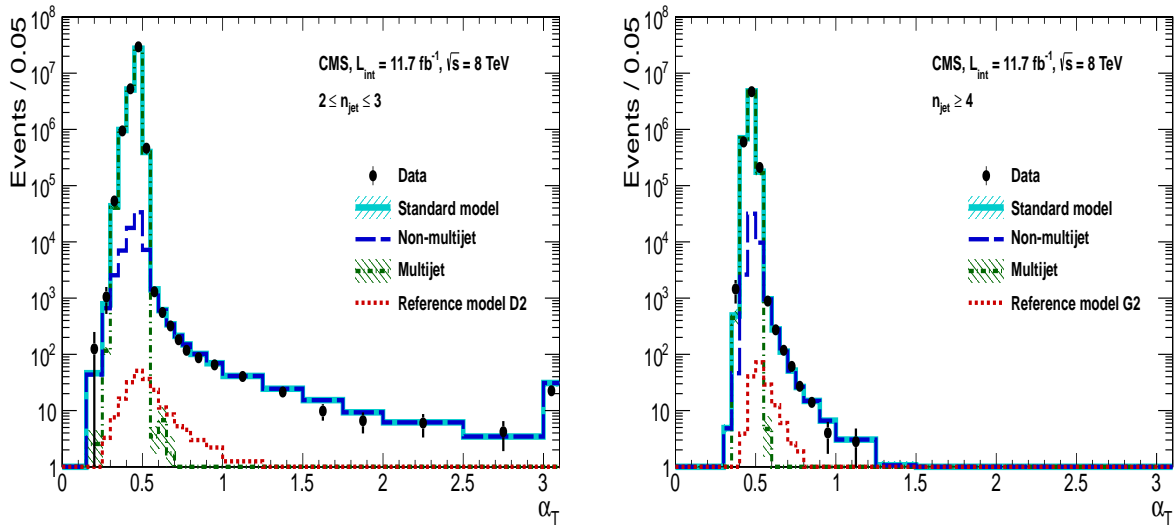


**Figure 4.3.:** The  $\alpha_T$  distributions for the low 2-3 (left) and high  $\geq 4$  (right) jet multiplicities after a full analysis selection and shown for  $H_T > 375$ . Data is collected using both prescaled  $H_T$  triggers and dedicated  $\alpha_T$  triggers for below and above  $\alpha_T = 0.55$  respectively. Expected yields as given by simulation are also shown for multijet events (green dash-dotted line), EWK backgrounds with genuine  $\cancel{E}_T$  (blue long-dashed line), the sum of all SM processes (cyan solid line) and the reference signal model D2 (left, red dotted line) or G2 (right, red dotted line).

1167 The  $\alpha_T$  requirement used within the search is chosen to be  $\alpha_T > 0.55$  to ensure  
1168 that the QCD multijet background is negligible even in the presence of moderate jet  
1169 mis-measurement. There still remains other effects which can cause multijet events to  
1170 artificially have a large  $\alpha_T$  value, which are discussed in detail in Section (4.2.2).

## 1171 4.2. Search Strategy

1172 The aim of the analysis presented in this thesis is to identify an excess of events in data  
1173 over the **SM** background expectation in multi-jet final states and significant  $\cancel{E}_T$ . The  
1174 essential suppression of the dominant QCD background for such a search is addressed by  
1175 the  $\alpha_T$  variable described in the previous section. For estimation of the remaining **EWK**  
1176 backgrounds, three independent data control samples are used to predict the different  
1177 processes that compose the background :

- 1178 •  $\mu + \text{jets}$  to determine  $W + \text{jets}$ ,  $t\bar{t}$  and single top backgrounds,
- 1179 •  $\gamma + \text{jets}$  to determine the irreducible  $Z \rightarrow \nu\bar{\nu} + \text{jets}$  background,
- 1180 •  $\mu\mu + \text{jets}$  to determine the irreducible  $Z \rightarrow \nu\bar{\nu} + \text{jets}$  background.

1181 These control samples are chosen to both be rich in specific **EWK** processes, be free of  
1182 QCD multi-jet events and to also be kinematically similar to the hadronic signal region  
1183 that they are estimating the backgrounds of, see Section (4.2.3).

1184 To remain inclusive to a large range of possible **SUSY** models, the signal region is  
1185 binned in the following categories to allow for increased sensitivity in the interpretation  
1186 of results for different **SUSY** topologies:

### 1187 Sensitivity to a range of **SUSY** mass splittings

1188 The hadronic signal region is defined by  $H_T > 275$ , divided into eight bins in  $H_T$ .

- 1189 – Two bins of width 50 GeV in the range  $275 < H_T < 375$  GeV,
- 1190 – five bins of width 100 GeV in the range  $375 < H_T < 875$  GeV,
- 1191 – and a final open bin,  $H_T > 875$  GeV.

1192 The choice at low  $H_T$  is driven primarily by trigger constraints. The mass difference  
1193 between the **LSP** and the particle that it decays from is an important factor in the  
1194 amount of hadronic activity in the event.

1195 A large mass splitting will lead to hard high  $p_T$  jets which contribute to the  $H_T$   
1196 sum. From Figure 4.1 it can be seen that the **SM** background falls sharply at high  
1197  $H_T$  values, therefore a large number of  $H_T$  bins will lead to easier identification  
1198 of such signals. Conversely smaller mass splittings lead to softer jet  $p_T$ 's which will  
1199 subsequently fall into the lower  $H_T$  range.

### 1200 Sensitivity to production method of **SUSY** particles

1201 The production mechanism of any potential **SUSY** signal can lead to different event  
1202 topologies. One such way to discriminate between gluino ( $g\tilde{g}$  - “high multiplicity”),  
1203 and direct squark ( $q\tilde{q}$  - “low multiplicity”) induced production of **SUSY** particles is  
1204 realised through the number of reconstructed jets in the final state.

1205 The analysis is thus split into two jet categories : 2-3 jets ,  $\geq 4$  jets to give sensitivity  
1206 to both of these mechanisms.

### 1207 Sensitivity to “Natural **SUSY**” via tagging jets from b-quarks

1208 Jets originating from bottom quarks (b-jets) are identified through vertices that  
1209 are displaced with respect to the primary interaction. The algorithm used to tag  
1210 b-jets is the Combined Secondary Vertex Medium Working Point (**CSVM**) tagger,  
1211 described within Section (3.3.2). A cut is placed on the discriminator variable of  
1212  $> 0.679$ , leading to a gluon/light-quark mis-tag rate of 1% and a jet  $p_T$  dependant  
1213 b-tagging efficiency of 60-70% [64].

1214 Natural **SUSY** models would be characterised through final-state signatures rich  
1215 in bottom quarks. A search relying on methods to identify jets originating from  
1216 bottom quarks through b-tagging, will significantly improve the sensitivity to this  
1217 class of signature.

1218 This is achieved via the binning of events in the signal region according to the  
1219 number of b-tagged jets reconstructed in each event, in the following: 0,1,2,3, $\geq 4$   
1220 b-tag categories . In the highest  $\geq 4$  b-tag category due to a limited number of  
1221 expected signal and background, just three  $H_T$  bins are employed: 275-325 GeV,  
1222 325-375 GeV,  $\geq 375$  GeV.

1223 This characterisation is identically mirrored in all control samples, with the infor-  
1224 mation from all samples and b-tag categories used simultaneously in the likelihood  
1225 model (see Chapter 6) in order to interpret the results in a coherent and powerful  
1226 way.

1227 The combination of the  $H_T$ , jet multiplicity and b-tag categorisation of the signal  
1228 region as described above, resultantly leads to 67 different bins in which the analysis is  
1229 interpreted in, which is depicted in Figure 4.4.

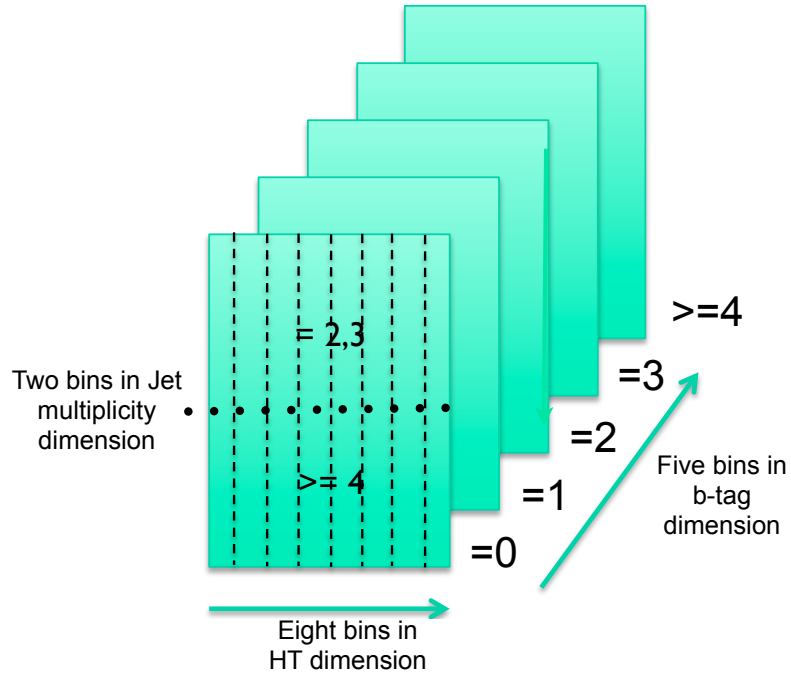


**Figure 4.4.:** Pictorial depiction of the analysis strategy employed by the  $\alpha_T$  search to increase sensitivity to a wide spectra of **SUSY** models.

### 1230 4.2.1. Physics Objects

1231 The physics objects used in the analysis defined below, follow the recommendation of  
1232 the various **CMS** Physics Object Groups (**POGs**).

#### 1233 • Jets

1234 The jets used in this analysis are CaloJets, reconstructed as described in Section  
1235 (3.3.1) using the anti- $k_T$  jet clustering algorithm.

1236 To ensure the jet object falls within the calorimeter systems a pseudo-rapidity  
1237 requirement of  $|\eta| < 3$  is applied. Each jet must pass a “loose” identification criteria  
1238 to reject jets resulting from unphysical energy, the criteria of which are detailed in  
1239 Table A.1 of Appendix (A) [74].

#### 1240 • Muons

1241 Muons are selected in the  $\mu + \text{jets}$  and  $\mu\mu + \text{jets}$  control samples, and vetoed in  
1242 the signal region. The same cut based identification criteria is applied to muons in  
1243 both search regions and is summarised in Table 4.2 [75].

Categories	Criteria
Global Muon	True
PFMuon	True
$\chi^2$	< 10
Muon chamber hits	> 0
Muon station hits	> 1
Transvere impact $d_{xy}$	< 0.2mm
Longitudinal distance $d_z$	< 0.5mm
Pixel hits	> 0
Track layer hits	> 5
PF Isolation (DeltaB corrected)	< 0.12

**Table 4.2.:** Muon Identification criteria used within the analysis for selection/veto purposes in the muon control/signal selections.

1244 Additionally muons are required to be within the acceptance of the muon tracking  
1245 systems. For the muon control samples, trigger requirements necessitate a  $|\eta| <$   
1246 2.1 for the selection of muons. In the signal region where muons are vetoed these  
1247 conditions are relaxed to  $|\eta| < 2.5$  and a minimum threshold of  $p_T > 10$  GeV is  
1248 required of muon objects.

### **• Photons**

1250 Photons are selected within the  $\gamma + \text{jets}$  control sample and vetoed in all other  
1251 selections. Photons are identified in both cases according to the cut based criteria  
1252 listed in Table 4.3 [76].

1253 Photon objects are also required to have a minimum momentum of  $p_T > 25$  GeV.

### **• Electrons**

1255 Electron identification is defined for veto purposes. They are selected according to  
1256 the following cut-based criteria listed in Table 4.4, utilising PF-based isolation.

1257 Electrons are required to be identified at  $|\eta| < 2.5$ , with a minimum  $p_T > 10$  GeV  
1258 threshold to ensure that the electron falls within the tracking system of the detector.

Variable	Definition
$H/E < 0.05$	The ratio of hadronic energy in the <b>HCAL</b> tower directly behind the <b>ECAL</b> super-cluster and the <b>ECAL</b> super-cluster itself.
$\sigma_{i\eta i\eta} < 0.011$	The log energy weighted width ( $\sigma$ ), of the extent of the shower in the $\eta$ dimension.
$R9 < 1.0$	The ratio of the energy of the $3 \times 3$ crystal core of the super-cluster compared to the total energy stored in the $5 \times 5$ super-cluster.
Combined Isolation $< 6$ GeV	The photons are required to be isolated with no electromagnetic or hadronic activity within a radius $\Delta R = 0.3$ of the photon object. A combination of the pileup subtracted [77], <b>ECAL</b> , <b>HCAL</b> and tracking isolation sums are used to determine the combined total isolation value.

**Table 4.3.:** Photon Identification criteria used within the analysis for selection/veto purposes in the  $\gamma +$  jets control/signal selections.

Categories	Barrel	EndCap
$\Delta\eta_{In}$	0.007	0.009
$\Delta\phi_{In}$	0.15	0.10
$\sigma_{i\eta i\eta}$	0.01	0.03
$H/E$	0.12	0.10
$d0$ (vtx)	0.02	0.02
$dZ$ (vtx)	0.20	0.20
$ (1/E_{ECAL} - 1/p_{track}) $	0.05	0.05
PF Combined isolation/ $p_T$	0.15	0.15
Vertex fit probability	$10^{-6}$	$10^{-6}$

**Table 4.4.:** Electron Identification criteria used within the analysis for veto purposes.

1259

- **Noise and  $E_T$  Filters**

1260

A series of Noise filters are applied to veto events which contain spurious non-physical jets that are not picked up by the jet id, and events which give large unphysical  $\cancel{E}_T$  values. These filters are listed within Table A.3 of Appendix (A).

1261

1262

---

### 1263 4.2.2. Event Selection

1264 The selection criteria for events within the analysis are detailed below. A set of common  
1265 cuts are applied to both signal (maximise acceptance to a range of **SUSY** signatures), and  
1266 control samples (retain similar jet kinematics for background predictions), with additional  
1267 selection cuts applied to each control sample to enrich the sample in a particular **EWK**  
1268 processes, see Section (4.2.3).

1269 The jets considered in the analysis are required to have a transverse momentum  $p_T >$   
1270 50 GeV, with a minimum of two jets required in the event. The highest  $E_T$  jet is required  
1271 to lie within the central tracker acceptance  $|\eta| < 2.5$ , and the two leading  $p_T$  jets must  
1272 each have  $p_T > 100$  GeV. Any event which has a jet with  $p_T > 50$  GeV that either fails  
1273 the “loose” identification criteria described in Section(4.2.1) or has  $|\eta| > 3.0$ , is rejected.  
1274 Similarly events in which an electron, muon or photon fails object identification but pass  
1275  $\eta$  and  $p_T$  restrictions are identified as an “odd” lepton/photon and the event is vetoed.

1276 At low  $H_T$ , the jet threshold requirements applied to be considered as part of the  
1277 analysis and enter the  $H_T$  sum are scaled downwards. These are scaled down in order to  
1278 not restrict phase space, preserving jet multiplicities and background admixture in the  
1279 lower  $H_T$  bins, as listed in Table 4.5.

$H_T$ bin	minimum jet $p_T$	second leading jet $p_T$
$275 < H_T < 325$	36.7	73.3
$325 < H_T < 375$	43.3	86.6
$375 < H_T$	50.0	100.0

**Table 4.5.:** Jet thresholds used in the three  $H_T$  regions of the analysis.

1280 Within the signal region to suppress **SM** processes with genuine  $\cancel{E}_T$  from neutrinos,  
1281 events containing isolated electrons or muons are vetoed. Furthermore to ensure a pure  
1282 multi-jet topology, events are vetoed if an isolated photon is found with  $p_T > 25$  GeV.

1283 An  $\alpha_T$  requirement of  $> 0.55$  is required to reduce the QCD multi-jet background  
1284 to a negligible amount. Finally additional cleaning cuts are applied to protect against  
1285 pathological deficiencies such as reconstruction failures or severe energy mis-measurements  
1286 due to detector inefficiencies:

- Significant  $H_T$  can arise in events with no real  $\cancel{E}_T$  due to multiple jets falling below  
the  $p_T$  threshold used for selecting jets. This in turn leads to events which can then

incorrectly pass the  $\alpha_T$  requirements of the analysis. This effect can be negated by requiring that the missing transverse momentum reconstructed from jets alone does not greatly exceed the missing transverse momentum reconstructed from all of the detector's calorimeter towers,

$$R_{miss} = \cancel{H}_T / \cancel{E}_T < 1.25.$$

- Fake  $\cancel{E}_T$  and  $\cancel{H}_T$  can arise due to significant jet mis-measurements caused by a small number of non-functioning **ECAL** regions. These regions absorb electromagnetic showers which are subsequently not added to the jet energy sum. To circumvent this problem the following procedure is employed : For each jet in the event, the angular separation

$$\Delta\phi_j^* \equiv \Delta\phi(p_j^\rightarrow - \sum_{i \neq j} p_i^\rightarrow), \quad (4.6)$$

is calculated where that jet is itself removed from the event. Here  $\Delta\phi^*$  is a measure of how aligned the  $\cancel{H}_T$  of an event is with a jet, a small value is compatible with the hypothesis of an inherently balanced event in which a jet has been mis-measured. For every jet in an event with  $\Delta\phi^* < 0.5$ , if the  $\Delta R$  distance between the selected jet and the closest dead **ECAL** region is also  $< 0.3$ , then the event is rejected. Similarly events are rejected if the jet points within  $\Delta R < 0.3$  of the **ECAL** barrel-endcap gap at  $|\eta| = 1.5$ .

Some of the key distributions of the data used in this analysis compared to MC simulation are shown in Figure 4.5. The MC samples are normalised to a luminosity of  $11.7 \text{ fb}^{-1}$ , with no requirement placed upon the number of b-tagged jets or number of jets in the events.

The distributions shown are presented for purely illustrative purposes, with the MC simulation itself not used in absolute term to estimate the yields from background processes, see Sections (4.2.3,4.5). However it is nevertheless important to demonstrate that good agreement exists between simulation and observation in data.

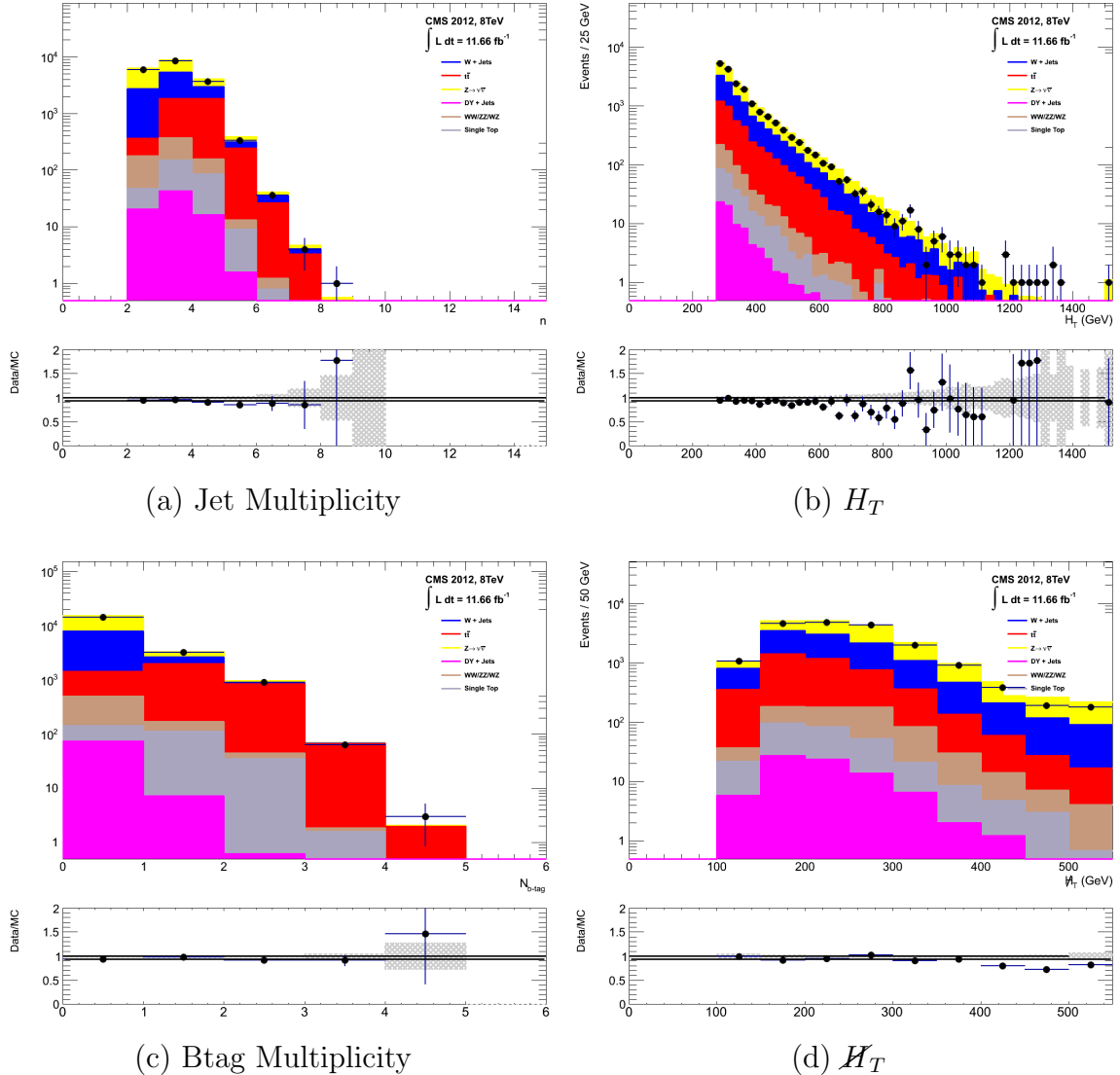


**Figure 4.5.:** Data/MC comparisons of key variables for the hadronic signal region, following the application of the hadronic selection criteria and the requirements of  $H_T > 275$  GeV and  $\alpha_T > 0.55$ . Bands represent the uncertainties due to the statistical size of the MC samples. No requirement is made upon the number of b-tagged jets or jet multiplicity in these distributions.

### 4.2.3. Control Sample Definition and Background Estimation

The method used to estimate the background contributions in the hadronic signal region relies on the use of a Transfer Factor (TF). This is determined from MC simulation in both the control,  $N_{MC}^{control}$ , and signal,  $N_{MC}^{signal}$ , region to transform the observed yield measured in data for a control sample,  $N_{obs}^{control}$ , into a background prediction,  $N_{pred}^{signal}$ , via Equation (4.7),

$$N_{\text{pred}}^{\text{signal}} = \frac{N_{\text{MC}}^{\text{signal}}}{N_{\text{MC}}^{\text{control}}} \times N_{\text{obs}}^{\text{control}}. \quad (4.7)$$

1314 All MC samples are normalised to the luminosity of the data samples,  $11.7 \text{ fb}^{-1}$ .  
1315 Through this method, “vanilla” predictions for the **SM** background in the signal region  
1316 can be made by considering separately the sum of the prediction from either the  $\mu + \text{jets}$   
1317 and  $\gamma + \text{jets}$  or  $\mu + \text{jets}$  and  $\mu\mu + \text{jets}$  samples. However the final background estimation  
1318 from which results are interpreted, is calculated via a fitting procedure defined formally  
1319 by the likelihood model described in Chapter 6.

1320 The sum of the expected yields from all MC processes, in each control sample enter  
1321 the denominator,  $N_{\text{MC}}^{\text{control}}$ , of the **TF** defined in Eq (4.7). However for the numerator  
1322,  $N_{\text{MC}}^{\text{signal}}$ , only the relevant processes that the control sample is used in estimating a  
1323 background for, enter into the **TF**.

1324 For the  $\mu + \text{jets}$  sample the simulated MC processes which enter the numerator of  
1325 the **TF** are,

$$N_{\text{MC}}^{\text{signal}}(H_T, n_{\text{jet}}) = N_W + N_{t\bar{t}} + N_{DY} + N_t + N_{di-boson}, \quad (4.8)$$

1326 whilst for both the  $\mu\mu + \text{jets}$  and  $\gamma + \text{jets}$  samples the only MC process used in the  
1327 numerator is,

$$N_{\text{MC}}^{\text{signal}}(H_T, n_{\text{jet}}) = N_{Z \rightarrow \nu\bar{\nu}}. \quad (4.9)$$

1328 The control samples and the **EWK** processes they are specifically tuned to select  
1329 are defined below, with distributions of key variables for each of the control samples  
1330 shown for illustrative purposes in Figures 4.6, 4.7 and 4.8. No requirement is placed  
1331 upon the number of b-tagged jets or jet multiplicity in the distributions shown. The  
1332 MC distributions highlight the background compositions of each control sample, where  
1333 in general, good agreement is observed between data and simulation, giving confidence

1334 that the samples are well understood. The contribution from QCD multi-jet events is  
1335 expected to be negligible :

1336 **The  $\mu +$  jets control sample**

1337 Events from  $W +$  jets and  $t\bar{t}$  processes enter into the hadronic signal sample due to  
1338 unidentified leptons from acceptance or threshold effects and hadronic tau decays.  
1339 These leptons originate from the decay of high  $p_T$   $W$  bosons.

1340 The control samples specifically identifies  $W \rightarrow \mu\bar{\nu}$  decays within the same phase-  
1341 space of the signal region, where the muon is subsequently ignored in the calculation  
1342 of event level variables, i.e.  $H_T$ ,  $\mathcal{H}_T$ ,  $\alpha_T$ . All kinematic jet-based cuts are identical  
1343 to those applied in the hadronic search region detailed in Section (4.2.2), with the  
1344 same  $H_T$ , jet multiplicity and b-jet multiplicity binning described above.

- 1345 – Muons originating from  $W$  boson decays are selected by requiring one tightly  
1346 isolated muon defined in Table 4.2, with a  $p_T > 30$  GeV and  $|\eta| < 2.1$ . Both of  
1347 these threshold arise from trigger restrictions.
- 1348 – The transverse mass of the  $W$  candidate must satisfy  $M_T(\mu, \cancel{E}_T) < 30$  GeV ( to  
1349 suppress QCD multi-jet events).
- 1350 – Events which contain a jet overlapping with a muon  $\Delta R(\mu, \text{jet}) < 0.5$  are vetoed  
1351 to remove events from muons produced as part of a jet’s hadronisation process.
- 1352 – Events containing a second muon candidate which has failed id, but passed  $p_T$   
1353 and  $|\eta|$  requirements, are checked to have an invariant mass that satisfies  $m_Z - 25 < M_{\mu_1\mu_2} > m_Z + 25$ , thus removing  $Z \rightarrow \mu\mu$  contamination.

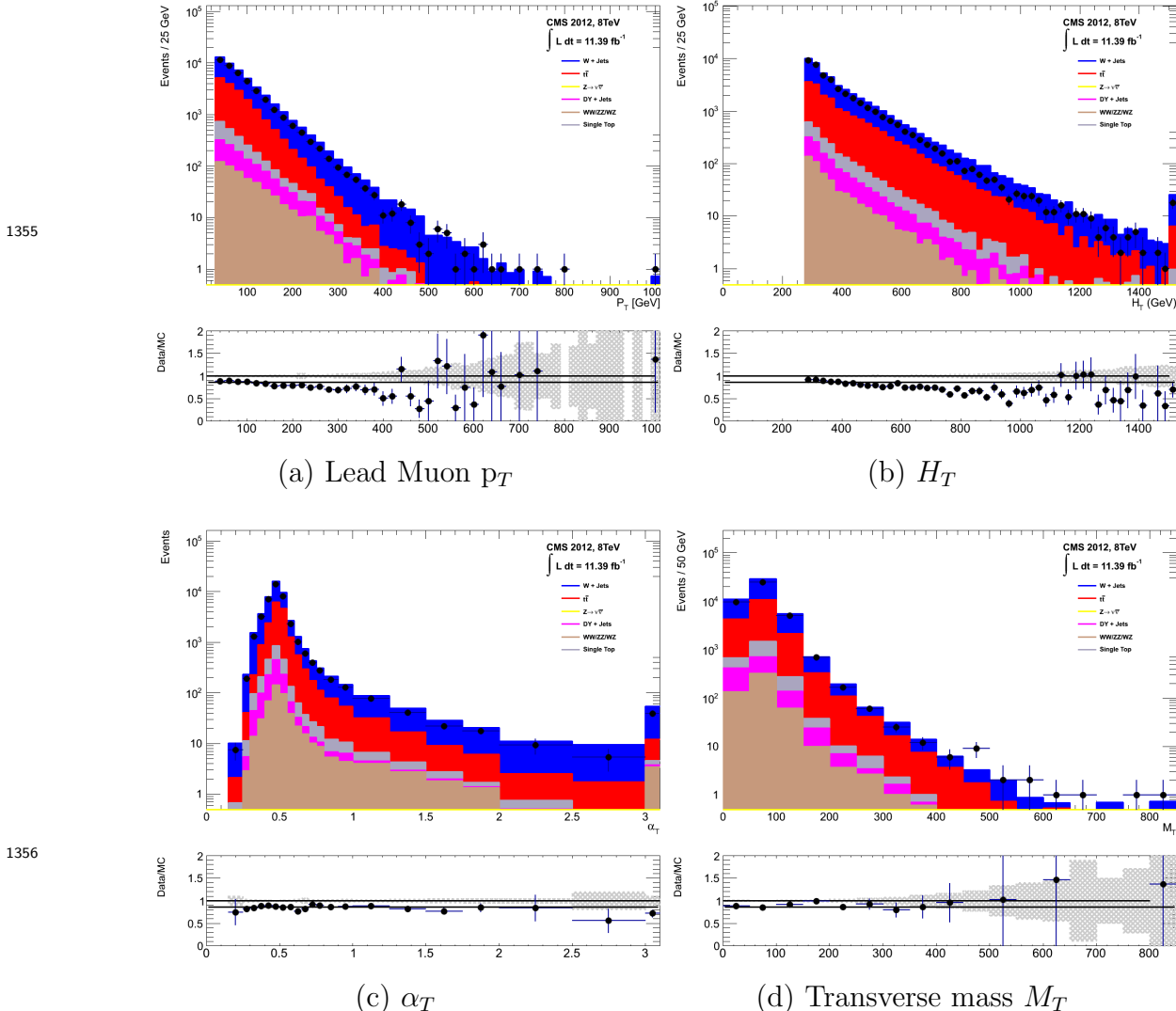


**Figure 4.6.:** Data/MC comparisons of key variables for the  $\mu + \text{jets}$  selection, following the application of selection criteria and the requirements that  $H_T > 275$  GeV. Bands represent the uncertainties due to the statistical size of the MC samples. No requirement is made upon the number of b-tagged jets or jet multiplicity in these distributions.

### The $\mu\mu + \text{jets}$ control sample

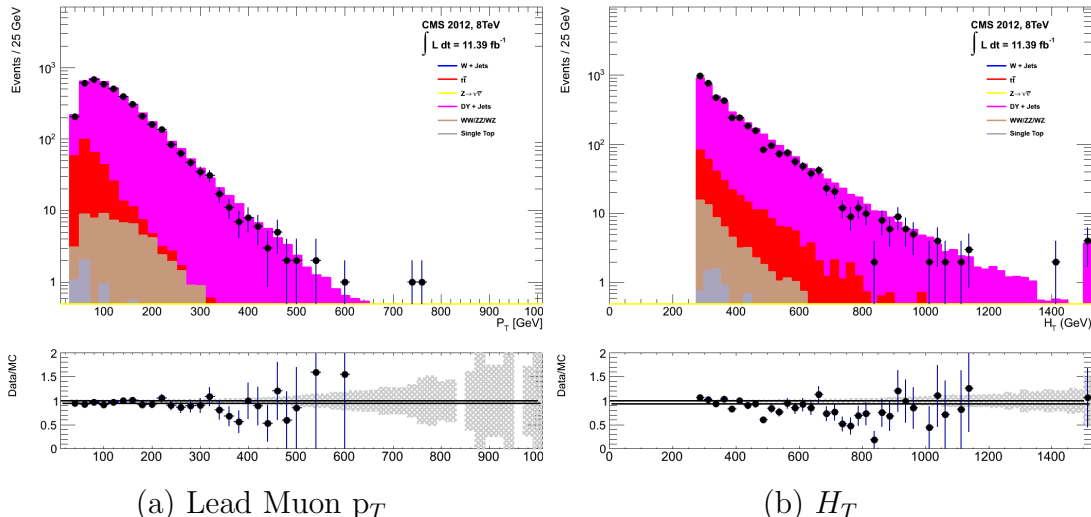
The  $Z \rightarrow \nu\bar{\nu} + \text{jets}$  background enters into the signal region from genuine  $\cancel{E}_T$  from the escaping neutrinos. This background is estimated using two control samples, the first of which is the  $Z \rightarrow \mu\bar{\mu} + \text{jets}$  process, which posses identical kinematic properties, but with different acceptance and branching ratio [1].

The same acceptance requirements as the  $\mu + \text{jets}$  selection for muons is applied, as defined in Table 4.2. Muons in the event are ignored for the purpose of the

calculation of event level variables. Kinematic jet-based cuts and phase space binning identical to the hadronic search region are also applied.

- Muons origination from a Z boson decay are selected requiring exactly two tightly isolated muons. Due to trigger requirements the leading muon is required to have  $p_T > 30$  GeV and  $|\eta| < 2.1$ . The requirement of the  $p_T$  on the second muon is relaxed to 10 GeV.
- Events are vetoed if containing a jet overlapping with a muon  $\Delta R(\mu, \text{jet}) < 0.5$ .
- In order to specifically select two muons both originating from a single Z boson decay, the invariant mass of the two muons must satisfy  $m_Z - 25 > M_{\mu_1\mu_2} < m_Z + 25$ .

The  $\mu\mu + \text{jets}$  sample is used to make predictions in the signal region in the two lowest  $H_T$  bins, providing coverage where the  $\gamma + \text{jets}$  sample is unable to, due to trigger requirements. In higher  $H_T$  bins, the higher statistics of the  $\gamma + \text{jets}$  sample is instead used to determine the  $Z \rightarrow \nu\bar{\nu}$  estimation.



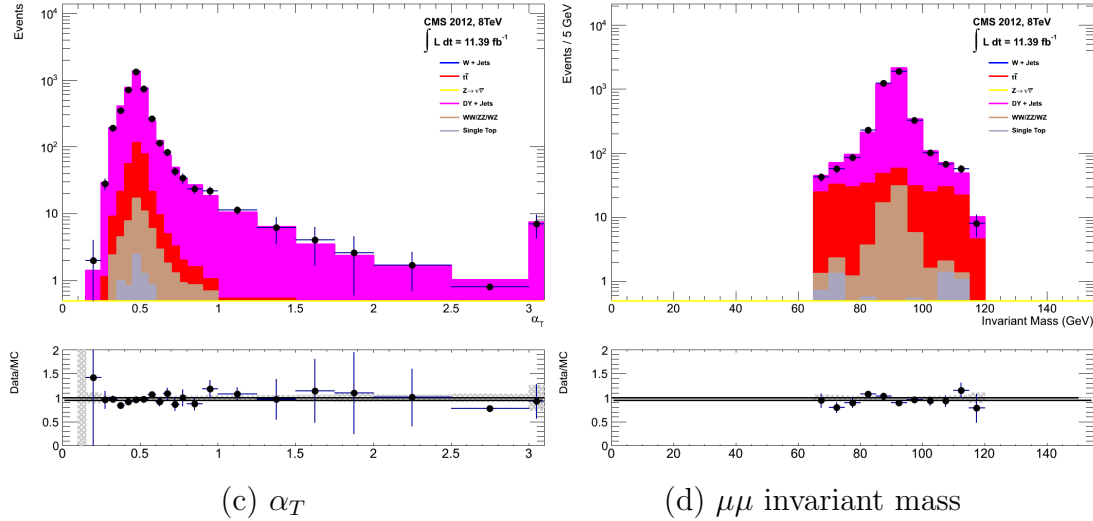


**Figure 4.7.:** Data/MC comparisons of key variables for the  $\mu\mu + \text{jets}$  selection, following the application of selection criteria and the requirements that  $H_T > 275$  GeV. Bands represent the uncertainties due to the statistical size of the MC samples. No requirement is made upon the number of b-tagged jets or jet multiplicity in these distributions.

### The $\gamma + \text{jets}$ control sample

The  $Z \rightarrow \nu\bar{\nu} + \text{jets}$  background is also estimated from a  $\gamma + \text{jets}$  control sample, which possesses a larger cross section and kinematic properties similar to those of  $Z \rightarrow \mu\bar{\mu}$  events where the photon is ignored [78][79]. The photon is ignored for the purpose of the calculation of event level variables, and identical selection cuts to the hadronic signal region are applied.

- Exactly one photon is selected, satisfying identification criteria as detailed in Table 4.3, with a minimum  $p_T > 165$  GeV to satisfy trigger thresholds and  $|\eta| < 1.45$  to ensure the photon remains in the barrel of the detector.
- A selection criteria of  $\Delta R(\gamma, \text{jet}) < 1.0$ , between the photon and all jets is applied to ensure the acceptance of only well isolated  $\gamma + \text{jets}$  events.
- Given that the photon is ignored, this control sample can only be applied in the  $H_T$  region  $> 375$  GeV, due to the trigger thresholds on the minimum  $p_T$  of the photon, and the  $H_T$  requirement of an  $\alpha_T > 0.55$  cut from Equation (4.5).

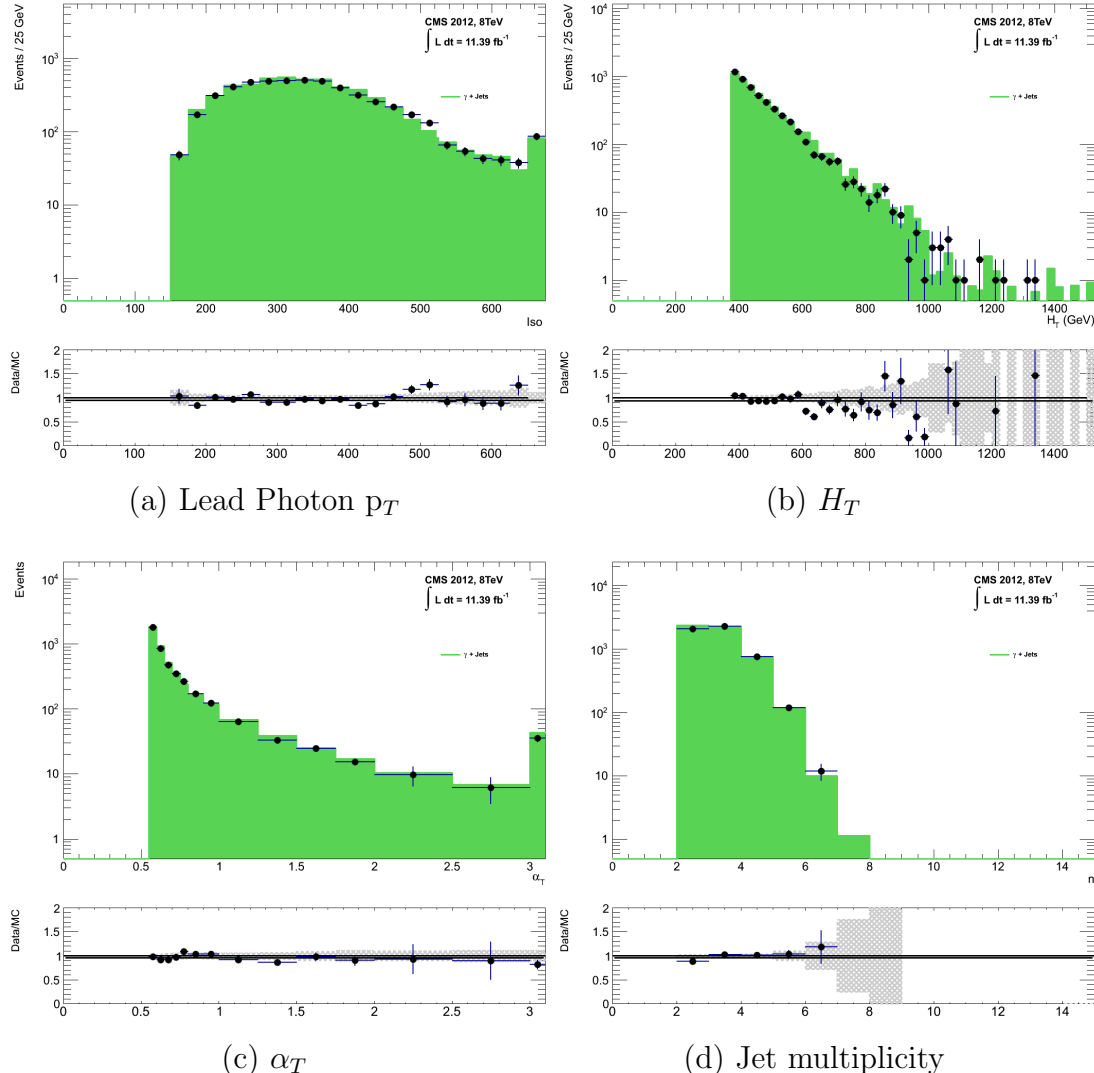


**Figure 4.8.:** Data/MC comparisons of key variables for the  $\gamma + \text{jets}$  selection, following the application of selection criteria and the requirements that  $H_T > 375 \text{ GeV}$  and  $\alpha_T > 0.55$ . Bands represent the uncertainties due to the statistical size of the MC samples. No requirement is made upon the number of b-tagged jets or jet multiplicity in these distributions.

The selection criteria of the three control samples are defined to ensure background composition and event kinematics mirror closely the signal region. This is done in order to minimise the reliance on MC simulation to model correctly the backgrounds and event kinematics in the control and signal samples.

However in the case of the  $\mu + \text{jets}$  and  $\mu\mu + \text{jets}$  samples, the  $\alpha_T$  requirement is relaxed in the selection criteria of these samples. This is made possible as contamination from QCD multi-jet events is suppressed to a negligible level by the other kinematic selection criteria within the two control samples, to select pure EWK processes. Thus in

1403 this way, the acceptance of the two muon control samples can be significantly increased,  
1404 which simultaneously improves their predictive power and further reduces the effect of  
1405 any potential signal contamination.

1406 The modelling of the  $\alpha_T$  variable is probed through a dedicated set of closure tests,  
1407 described in Section (4.6), which demonstrate that the different  $\alpha_T$  acceptances for the  
1408 control and signal samples have no significant systematic bias on the prediction.

#### 1409 4.2.4. Estimating the QCD Background Multi-jet Background

1410 A negligible background from QCD multi-jet events within the hadronic signal region  
1411 is expected due to the selection requirement, and additional cleaning filters applied.  
1412 However a conservative approach is still adopted and the likelihood model (see Section  
1413 (6.1)), is given the freedom to estimate any potential QCD multi-jet contamination.

1414 Any potential contamination can be identified through the variable  $R_{\alpha_T}$ , defined as  
1415 the ratio of events above and below the  $\alpha_T$  threshold value used in the analysis. This is  
1416 modelled by a  $H_T$  dependant falling exponential function which takes the form,

$$R_{\alpha_T}(H_T) = A \exp^{-k_{QCD} H_T}, \quad (4.10)$$

1417 where the parameters  $A$  and  $k_{QCD}$  are the normalisation and exponential decay  
1418 constants respectively.

1419 For QCD event topologies this exponential behaviour is expected as a function of  $H_T$   
1420 for several reasons. The improvement of jet energy resolution at higher  $H_T$  due to higher  
1421  $p_T$  jets leads to a narrower peaked distribution, causing  $R_{\alpha_T}$  to fall. Similarly at higher  
1422  $H_T$  values  $> 375$  GeV, the jet multiplicity rises slowly with  $H_T$ . As shown in Figure 4.3,  
1423 at higher jet multiplicities, the result of the combinatorics used in the determination of  
1424  $\alpha_T$ , also lead to a narrower  $\alpha_T$  distribution.

1425 The value of the decay constant  $k_{QCD}$  is constrained via measurements within data  
1426 sidebands to the signal region. This is also done to validate the falling exponential  
1427 assumption for QCD multi-jet topologies. The sidebands are enriched in QCD multi-jet  
1428 background and defined as regions where  $\alpha_T$  is relaxed or that the  $R_{miss}$  cut is inverted.

1429 Figure 4.9 depicts the definition of these data sidebands used to constrain the value of  
1430  $k_{QCD}$ .

1431

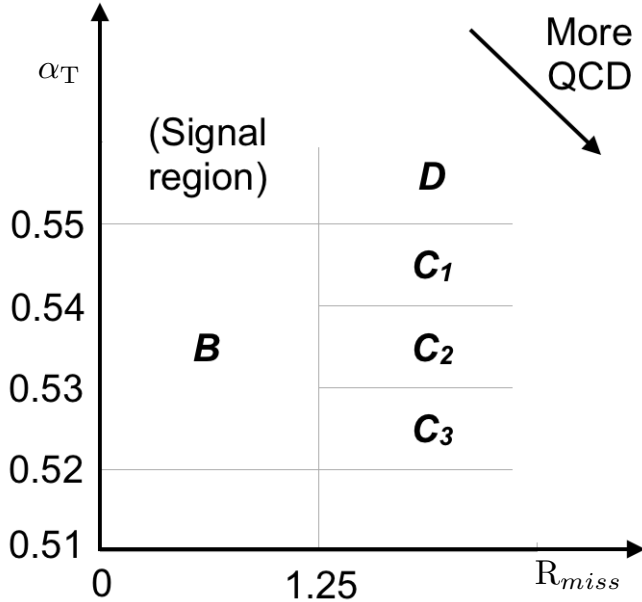


**Figure 4.9.:** QCD sideband regions, used for determination of  $k_{QCD}$ .

1432 The fits to determine the value of  $k_{QCD}$  are shown in Appendix (C.1), for which the best  
1433 fit value obtained from sideband region B is determined to be  $k_{QCD} = 2.96 \pm 0.64 \times 10^{-2}$   
1434  $\text{GeV}^{-1}$ .

1435 The best fit values of the remaining three C sideband regions are used to estimate  
1436 the systematic uncertainty on the central value obtained from sideband region B. The  
1437 variation of these measured values is used to determine the error on the determined  
1438 central value, and is calculated to be  $1.31 \pm 0.26 \times 10^{-2} \text{GeV}^{-1}$ . This relative error of  $\sim$   
1439 20% gives an estimate of the systematic uncertainty of the measurement to be applied to  
1440  $k_{QCD}$ .

1441 Finally the same procedure is performed for sideband region D to establish that the  
1442 value of  $k_{QCD}$  extracted from a lower  $\alpha_T$  slice can be applied to the signal region  $\alpha_T >$   
1443 0.55. The likelihood fit is performed across all  $H_T$  bins within the QCD enriched region  
1444 with no constraint applied to  $k_{QCD}$ . The resulting best fit value for  $k_{QCD}$  shows good  
1445 agreement between that and the weighted mean determined from the three C sidebands  
1446 regions. This demonstrates that the assumption of using the central value determined  
1447 from sideband region B, to provide an unbiased estimator for  $k_{QCD}$  in the signal region  
1448 ( $\alpha_T > 0.55$ ) is valid.

1449 Table 4.6, summarises the best fit  $k_{QCD}$  values determined for each of the sideband  
1450 regions to the signal region.

Sideband region	$k_{QCD} (\times 10^{-2} GeV^{-1})$	p-value
B	$2.96 \pm 0.64$	0.24
C <sub>1</sub>	$1.19 \pm 0.45$	0.93
C <sub>2</sub>	$1.47 \pm 0.37$	0.42
C <sub>3</sub>	$1.17 \pm 0.55$	0.98
C(weighted mean)	$1.31 \pm 0.26$	-
D(likelihood fit)	$1.31 \pm 0.09$	0.57

**Table 4.6.:** Best fit values for the parameters  $k_{QCD}$  obtained from sideband regions B,C<sub>1</sub>,C<sub>2</sub>,C<sub>3</sub>. The weighted mean is determined from the three measurements made within sideband region C. The maximum likelihood value of  $k_{QCD}$  given by the simultaneous fit using sideband region D. Quotes errors are statistical only.

### 1451 4.3. Trigger Strategy

1452 A cross trigger based on the quantities  $H_T$  and  $\alpha_T$ , labelled is used with varying thresholds  
1453 across  $H_T$  bins to record the events used in the hadronic signal region. The  $\alpha_T$  legs of the  
1454  $HT\_alphaT$  triggers used in the analysis are chosen to fully suppress QCD multi-jet events,  
1455 whilst maintaining a sustainable trigger rate. To further maintain an acceptable rate for  
1456 these analysis specific triggers, only calorimeter information is used in the reconstruction  
1457 of the  $H_T$  sum, leading to the necessity for Calo jets to be used within the analysis.

1458 A single object prescaled  $H_T$  trigger is used to collect events for the hadronic control  
1459 region described above in Section (4.2.4).

1460 The performance of the  $\alpha_T$  and  $H_T$  triggers used to collect data for the signal and  
1461 hadronic control region is measured with respect to a reference sample collected using the  
1462 muon system. This allows measurement of both the Level 1 seed and higher level triggers  
1463 simultaneously, as the reference sample is collected independent of any jet requirements.

1464 The selection for the trigger efficiency measurement is identical to that described in  
1465 Section (4.2.2), with the requirement of exactly one well identified muon with  $p_T > 30$   
1466 GeV which is subsequently ignored.

1467 The efficiencies measure for the  $HT\_alphaT$  triggers in bins individual  $H_T$  and  $\alpha_T$  legs,  
1468 is summarised in Table 4.7.

$H_T$ range (GeV)	$\epsilon$ on $H_T$ leg (%)	$\epsilon$ on $\alpha_T$ leg (%)
275-325	$87.7^{+1.9}_{-1.9}$	$82.8^{+1.0}_{-1.1}$
325-375	$90.6^{+2.9}_{-2.9}$	$95.9^{+0.7}_{-0.9}$
375-475	$95.7^{+0.1}_{-0.1}$	$98.5^{+0.5}_{-0.9}$
475- $\infty$	$100.0^{+0.0}_{-0.0}$	$100.0^{+0.0}_{-4.8}$

**Table 4.7.:** Measured efficiencies of the  $H_T$  and  $\alpha_T$  legs of the HT and  $HT\_alphaT$  triggers in independent analysis bins. The product of the two legs gives the total efficiency of the trigger in a given offline  $H_T$  bin.

1469 Data for the control samples of the analysis, detailed in Section (4.2.3), are collected  
1470 using single object photon trigger for the  $\gamma +$  jets sample, and a single object muon  
1471 trigger for both the  $\mu +$  jets and  $\mu\mu +$  jets control samples. The photon trigger is  
1472 measured to be full efficient for the threshold  $p_T^{photon} > 150 GeV$ , whilst the single muon  
1473 efficiency satisfying  $p_T^{muon} > 30 GeV$  is measured to have an efficiency of  $(88 \pm 2)\%$  that  
1474 is independent of  $H_T$ . In the case of the  $\mu\mu +$  jets control sample, the efficiency is  
1475 measured to be  $(95 \pm 2)\%$  for the lowest  $H_T$  bin, rising to  $(98 \pm 2)\%$  for the highest  $H_T$   
1476 bin.

## 1477 4.4. Measuring MC normalisation factors via $H_T$ 1478 sidebands

1479 The theoretical cross sections of different SM processes at Next to Next Leading Order  
1480 (NNLO) and the number of MC simulated events generated for that particular process,  
1481 is typically used to determine the appropriate normalisation for a MC sample. However  
1482 within the particular high- $H_T$  and high- $\cancel{E}_T$  corners of kinematic phase space probed  
1483 within this search, the theoretical cross sections for various processes are far less well  
1484 understood.

1485 To mitigate the problem of theoretical uncertainties and arbitrary choices of cross  
1486 sections, the normalisation of MC samples used in the analysis are determined through  
1487 the use data sidebands. The sidebands are used to calculated sample specific correct  
1488 factors (k-factors) that are appropriate for the  $H_T$ - $\cancel{E}_T$  phase space covered by this analysis.

1489 They are defined within the  $\mu +$  jets and  $\mu\mu +$  jets control sample, by the region  $200 <$   
1490  $H_T < 275$ , using the same jet  $p_T$  thresholds as the adjacent first analysis bin. Individual

1491 **EWK** processes are isolated within each of these control samples via requirements on  
1492 jet multiplicity and the requirement on b-tags, summarised in Table 4.8. The purity of  
1493 the samples are typically  $> 90\%$  with any residual contamination corrected for. The  
1494 resultant k-factor for each process is determined by then taking ratio of the data yield  
1495 over the MC expectation in the sideband. Subsequently these k-factors are then applied  
1496 to the processes within the phase space of the analysis.

Process	Selection	Observation	MC expectation	k-factor
W + jets	$\mu + \text{jets}, n_b=0, n_{jet} = 2,3$	26950	$29993.2 \pm 650.1$	$0.90 \pm 0.02$
$Z \rightarrow \mu\mu + \text{jets}$	$\mu\mu + \text{jets}, n_b=0, n_{jet} = 2,3$	3141	$3402.0 \pm 43.9$	$0.92 \pm 0.02$
$t\bar{t}$	$\mu + \text{jets}, n_b=2, n_{jet} = \geq 4$	2190	$1967.8 \pm 25.1$	$1.11 \pm 0.02$

**Table 4.8.:** k-factors calculated for different **EWK** processes. All k-factors are derived relative to theoretical cross sections calculated in **NNLO**. The k-factors measured for the  $Z \rightarrow \mu\mu + \text{jets}$  processes, are also applied to the  $Z \rightarrow \nu\bar{\nu} + \text{jets}$  and  $\gamma + \text{jets}$  MC samples.

## 1497 4.5. Determining MC Yields With Higher 1498 Statistical Precision

1499 Reconstructing events from **EWK** processes with many b-tagged jets ( $\geq 3$ ),  $n_b^{reco}$ , is largely  
1500 driven by the mis-tagging of light jets within the event. This is clear when considering  
1501 the main **EWK** backgrounds in the analysis, such as  $t\bar{t} + \text{jets}$  events, which typically  
1502 contain two b-flavoured jets from the decay of the top quarks, whilst W + jets and  
1503 Z  $\rightarrow \mu\mu + \text{jets}$  events will typically contain no b-flavoured jets.

1504 When the expectation for the number of  $n_b^{reco}$  is taken directly from simulation, the  
1505 statistical uncertainty at large b-tag multiplicities becomes relatively large. In order to  
1506 reduce this uncertainty one approach is to use the information encoded throughout all  
1507 events in the simulation sample, to measure each of the four ingredients:

- 1508 1. the b-tagging efficiency in the event selection,
- 1509 2. the charm-tagging efficiency in the event selection
- 1510 3. the mis-tagging rate in the event selection,
- 1511 4. the underlying flavour distribution of the jets in the events,

1512 that determine the  $n_b^{reco}$  distribution of the process being measured. This method  
1513 allows the determination of higher b-tag multiplicities to a higher degree of accuracy  
1514 reducing the statical uncertainties of the MC which enter into the TF's. For the discussion  
1515 that follows, these predictions are determined on average (i.e not on an event-by-event  
1516 basis), and is known as the formula method.

### 1517 4.5.1. The formula method

1518 The assigning of jet flavours to reconstruction level jets in simulation is achieved via an  
1519 algorithmic method defined as:

- 1520 • Try to find the parton that most likely determines the properties of the jet and  
1521 assign that flavour as true flavour,
- 1522 • Here, the “final state” partons (after showering, radiation) are analysed (also within  
1523  $\Delta R < 0.3$  of reconstructed jet cone),
- 1524 • Jets from radiation are matched with full efficiency,
- 1525 • If there is a b/c flavoured parton within the jet cone: label as b/c flavoured jet,
- 1526 • Otherwise: assign flavour of the hardest parton.

1527 Within each individual MC process and each  $H_T$ - $n_{jet}$  bin in the analysis, the  $n_b^{reco}$   
1528 distribution is constructed in the following way:

1529 Let  $N(n_b^{gen}, n_c^{gen}, n_q^{gen})$  represent the yield in simulation of events with  $b$  underlying  
1530 b-quarks,  $c$  underlying c-quarks and  $q$  underlying light quarks which are matched to  
1531 reconstructed jets. Light quarks are defined as those which originate from a  $u,d,s,g$  and  
1532  $\tau$  jets which are grouped together having similar mis-tagging rates. Similarly defining  $\epsilon$ ,  
1533  $\beta$  and  $m$ , which represent the measured b-tagging,c-tagging and mis-tagging efficiency  
1534 averaged over all the jets within that particular analysis bin.

1535 Using this information the expected number of jets which have been b-tagged can be  
1536 analytically calculated using the formula :

$$N(n_b) = \sum_{n_b^{gen} + n_c^{gen} + n_q^{gen} = n_{jet}} \sum_{n_b^{tag} + n_c^{tag} + n_q^{tag} = n_b} N(n_b^{gen}, n_c^{gen}, n_q^{gen}) \times P(n_b^{tag}, n_b^{gen}, \epsilon) \times \\ P(n_c^{tag}, n_c^{gen}, \beta) \times P(n_q^{tag}, n_q^{gen}, m), \quad (4.11)$$

with  $N(n_b)$  representing the event yield where  $n_b$  jets have been b-tagged,  $n_b^{tag}$ ,  $n_c^{tag}$  and  $n_q^{tag}$  represent the number of times that a particular jet flavour results in a b-tagged jet, and  $P(n_b^{tag}, n_b^{gen}, \epsilon)$ ,  $P(n_c^{tag}, n_c^{gen}, \beta)$  and  $P(n_q^{tag}, n_q^{gen}, m)$  represent the binomial probabilities for that to happen.

This approach ultimately results in a more precise  $n_b^{reco}$  distribution prediction as information from throughout the entire MC sample is used to estimate the high  $n_b^{reco}$  bins.

### 4.5.2. Establishing proof of principle

In order to validate the procedure, the predictions obtained from the formula method summarised in Eq (4.11), are compared directly to those obtained directly from simulation. These results for the  $\mu +$  jets control sample are summarised in Table 4.9, for the 0,1,2 and 3  $n_b^{reco}$  bins.

Process	Selection	Observation	MC expectation	k-factor
---------	-----------	-------------	----------------	----------

**Table 4.9.:** place holder

### 4.5.3. Correcting Measured Efficiencies In Simulation To Data

As detailed in Section (3.3.2), it is necessary for certain  $p_T$  and  $\eta$  dependant corrections, to be applied to both the b-tagging efficiency and mis-tagging rates in order correct the efficiencies from simulation to the distributions seen in data. These corrections are factored in.

Show plot of before and after correction to btag/mistag rate.

These corrections come with uncertainties..

show plot of effect of scaling correction factor up and down. 2

## 1557 4.6. Systematic Uncertainties On Transfer Factors

1558 Since the TF's used to establish the background prediction are obtained from simulation,  
1559 an appropriate systematic uncertainty is assigned to each factor to account for theoretical  
1560 uncertainties [80] and limitations in the simulation modelling of event kinematics and  
1561 instrumental effects.

1562 The magnitudes of these systematic uncertainties are established through a set of data  
1563 driven method, in which the three independent control samples of the analysis ( $\mu + \text{jets}$ ,  
1564  $\mu\mu + \text{jets}$ ,  $\gamma + \text{jets}$ ) are used to in a series of closure tests. The yields from one of these  
1565 control samples, along with the corresponding TF obtained from simulation, are used to  
1566 predict the yields in another control sample, using the same method of establishing a  
1567 background prediction for the signal region as described in Section (4.2.3).

1568 The level of agreement between the predicted and observed yields is expressed as the  
1569 ratio

$$\frac{(N_{obs} - N_{pred})}{N_{pred}}, \quad (4.12)$$

1570 while considering only the statistical uncertainties on  $N_{pred}$ , the prediction, and  $N_{obs}$ ,  
1571 the observation. No systematic uncertainty is assigned to the prediction, and resultantly  
1572 the level of closure is defined by the statistical significance of a deviation from the ratio  
1573 from zero.

1574 This ratio is measured for each  $H_T$  bin in the analysis, allowing these closure tests to  
1575 be sensitive to both the presence of any significant biases or any possible  $H_T$  dependence  
1576 on the level of closure.

1577 Eight sets of closure tests are defined between the three data control samples, con-  
1578 ducted independently between the two jet multiplicity ( $2 \leq n_{jets} \leq 3$ ,  $n_{jet} \geq 4$  ) bins.  
1579 Each of these tests are specifically chosen to probe each of the different key ingredients  
1580 of the simulation modelling that can affect the background prediction.

1581 Each of the different modelling components and the relevant closure tests are described  
1582 below :

1583  **$\alpha_T$  modelling**

1584 The modelling of the  $\alpha_T$  distribution in genuine  $Z_T$  events is probed with the  $\mu +$   
1585 jets control sample. This test is important to verify the approach of remove the  $\alpha_T$   
1586  $> 0.55$  requirement from the  $\mu +$  jets and  $\mu\mu +$  jets samples to increase the precision  
1587 of the background prediction. The test uses the  $\mu +$  jets sample without an  $\alpha_T$  cut  
1588 to make a prediction into the  $\mu +$  jets sample defined with the requirement  $\alpha_T >$   
1589  $0.55$ .

### 1590 **Background admixture**

1591 The sensitivity of the translation factors to the relative admixture of events from  
1592  $W +$  jets and  $t\bar{t}$  processes is probed by two closure tests. These tests represent  
1593 an extremely conservative approach as the admixture of the background remains  
1594 similar between the  $\mu +$  jets sample and the signal region, contrary to the defined  
1595 closure tests which make predictions between two very different admixtures of  $W +$   
1596 jets and  $t\bar{t}$  events.

1597 Within the  $\mu +$  jets sample, a  $W$  boson enriched sub-sample ( $n_b = 0$ ) is used to  
1598 predict yields in a  $t\bar{t}$  enriched sub-sample ( $n_b = 1$ ). Similarly the  
1599  $t\bar{t}$  enriched sub-sample ( $n_b = 1$ ) is also used to predict yields for a further enriched  
1600  $t\bar{t}$  sub-sample ( $n_b = 2$ ).

1601 Similarly a further closure test probes the relative contribution of  $Z +$  jets to  $W +$  jets  
1602 and  $t\bar{t}$  events, through the use of the  $\mu +$  jets sample to predict yields for the  $\mu\mu +$   
1603 jets control sample. This closure test, also at some level probes the muon trigger  
1604 and reconstruction efficiencies, given that exactly one and two muons are required  
1605 by the different selections.

### 1606 **Consistency between control samples**

1607 An important consistency check between the  $\mu\mu +$  jets jets and  $\gamma +$  jets, which are  
1608 both used in the prediction of the  $Z \rightarrow \nu\bar{\nu}$  in the signal region, is measured by using  
1609 the  $\gamma +$  jets sample to predict yields for the  $\mu\mu +$  jets control sample.

### 1610 **Modelling of jet multiplicity**

1611 The simulation modelling of the jet multiplicity within each control sample is  
1612 important due to the exclusive jet multiplicity binning within the analysis. This is  
1613 probed via the use of each of the three control samples to independently predict  
1614 from the lower jet multiplicity category  $2 \leq n_{jet} \leq 3$ , to the high jet category  $\geq 4$ .

1615 For the case of the  $\mu + \text{jets}$  and  $\mu\mu + \text{jets}$  control samples this test this is also a  
1616 further probe of the admixture between  $W + \text{jets}/Z + \text{jets}$  and  $t\bar{t}$ .

1617 To test for the assumption that no  $H_T$  dependences exist within the background  
1618 predictions of the analysis, the first five closure tests defined above are taken, with zeroeth  
1619 and first order polynomial fits are applied to each. This is summarised in Table 4.10 and  
1620 Table 4.11 which show the results for both the  $2 \leq n_{jet} \leq 3$  and  $\geq 4$  jet multiplicity bins  
1621 respectively.

Closure test	Symbol	Constant fit		Linear fit	
		Best fit value	p-value	Slope ( $10^{-4}$ )	p-value
$\alpha_T < 0.55 \rightarrow \alpha_T > 0.55 (\mu + \text{jets})$	Circle	$-0.06 \pm 0.02$	0.93	$-1.3 \pm 2.2$	0.91
$0 \text{ b-jets} \rightarrow 1 \text{ b-jet } (\mu + \text{jets})$	Square	$0.07 \pm 0.02$	0.98	$-1.6 \pm 1.6$	1.00
$1 \text{ b-jets} \rightarrow 2 \text{ b-jet } (\mu + \text{jets})$	Triangle	$-0.07 \pm 0.03$	0.76	$-2.7 \pm 3.0$	0.76
$\mu + \text{jets} \rightarrow \mu\mu + \text{jets}$	Cross	$0.10 \pm 0.03$	0.58	$-1.1 \pm 2.3$	0.49
$\mu\mu + \text{jets} \rightarrow \gamma + \text{jets}$	Star	$-0.06 \pm 0.04$	0.31	$4.2 \pm 4.3$	0.29

**Table 4.10.:** A summary of the results obtained from fits of zeroeth order polynomials (i.e. a constant) to five sets of closure tests performed in the  $2 \leq n_{jet} \leq 3$  bin. The final two columns show the best fit value for the slope obtained when performing a linear fit and the p-value for the linear fit.

Closure test	Symbol	Constant fit		Linear fit	
		Best fit value	p-value	Slope ( $10^{-4}$ )	p-value
$\alpha_T < 0.55 \rightarrow \alpha_T > 0.55 (\mu + \text{jets})$	Circle	$-0.05 \pm 0.03$	0.21	$3.0 \pm 2.9$	0.21
$0 \text{ b-jets} \rightarrow 1 \text{ b-jet } (\mu + \text{jets})$	Square	$-0.03 \pm 0.03$	0.55	$-1.0 \pm 1.9$	0.47
$1 \text{ b-jets} \rightarrow 2 \text{ b-jet } (\mu + \text{jets})$	Triangle	$-0.02 \pm 0.03$	0.39	$1.1 \pm 2.2$	0.31
$\mu + \text{jets} \rightarrow \mu\mu + \text{jets}$	Cross	$0.08 \pm 0.07$	0.08	$4.8 \pm 4.3$	0.07
$\mu\mu + \text{jets} \rightarrow \gamma + \text{jets}$	Star	$-0.03 \pm 0.10$	0.72	$-4.0 \pm 7.0$	0.64

**Table 4.11.:** A summary of the results obtained from fits of zeroeth order polynomials (i.e. a constant) to five sets of closure tests performed in the  $n_{jet} \geq q$  bin. The final two columns show the best fit value for the slope obtained when performing a linear fit and the p-value for the linear fit.

1622 Table 4.12 shows the same fits applied to the three closure tests that probe the  
1623 modelling between the different  $n_{jet}$  bins. The best fit value and its uncertainty is listed  
1624 for each set of closure tests in all three tables, along with the p-value of the constant and  
1625 linear fits applied.

Closure test	Symbol	Constant fit		Linear fit	
		Best fit value	p-value	Slope ( $10^{-4}$ )	p-value
$\mu + \text{jets}$	Inverted triangle	$-0.03 \pm 0.02$	0.02	$0.0 \pm 1.0$	0.01
$\mu + \text{jets}$ (outlier removed)	Inverted triangle	$-0.04 \pm 0.01$	0.42	$-1.4 \pm 1.1$	0.49
$\gamma + \text{jets}$	Diamond	$0.12 \pm 0.05$	0.79	$6.0 \pm 4.7$	0.94
$\mu\mu + \text{jets}$	Asterisk	$-0.04 \pm 0.07$	0.20	$4.9 \pm 4.4$	0.20

**Table 4.12.:** A summary of the results obtained from fits of zeroeth order polynomials (i.e. a constant) to five sets of closure tests performed in the  $2 \leq n_{\text{jet}} \leq 3$  bin. The final two columns show the best fit value for the slope obtained when performing a linear fit and the p-value for the linear fit.

1626     The best fit value for the constant parameter is indicative of the level of closure,  
 1627     averaged across the full range of  $H_T$  bins in the analysis, and the p-value an indicator of  
 1628     any significant dependence on  $H_T$  within the closure tests. The best fit values of all the  
 1629     tests are either statistically compatible with zero bias (i.e, less than  $2\sigma$  from zero) or at  
 1630     the level of 10% or less, with the exception of one closure test discussed below.

1631     Within Table 4.12, there exists one test that does not satisfy the above statement,  
 1632     which is the  $2 \leq n_{\text{jet}} \leq 3 \rightarrow n_{\text{jet}} \geq 4$  test using the  $\mu + \text{jets}$  control sample. The low  
 1633     p-value can be largely attributed to an outlier in the  $675 < H_T < 775$  GeV bin, rather  
 1634     than any significant trend in  $H_T$ . Removing this single outlier from the constant fit  
 1635     performed, gives a best fit value of  $-0.04 \pm 0.01$ ,  $\chi^2/\text{d.o.f} = 6.07/6$ . and a p-value of  
 1636     0.42. These modified fit results are included within Table 4.12 .

1637     In addition the best fit values for the slope terms of the linear fits in all three tables  
 1638     are of the order  $10^{-4}$ , which corresponds to a percent level change per 100 GeV. However  
 1639     in all cases, the best fit values are fully compatible with zero (within  $1\sigma$ ) once again with  
 1640     the exception detailed above, indicating that the level of closure is  $H_T$  independent.

#### 1641     4.6.1. Determining systematic uncertainties from closure tests

1642     Once it has been established that no significant bias or trend has been exist within  
 1643     the closure tests, systematic uncertainties are determined. The statistical precision  
 1644     of the closure tests is considered a suitable benchmark for determining the systematic  
 1645     uncertainties that are assigned to the TF's, which are propagated through to the likelihood  
 1646     fit.

1647 The systematic uncertainty band is split into five separate regions of  $H_T$ :

1648 1.  $275 < H_T < 325\text{GeV}$

1649 2.  $325 < H_T < 375\text{GeV}$

1650 3.  $375 < H_T < 575\text{GeV}$

1651 4.  $575 < H_T < 775\text{GeV}$

1652 5.  $H_T > 775\text{ GeV}$

1653 Within each region the square root of the sample variance,  $\sigma^2$ , is taken over the eight  
1654 closure tests to determine the systematic uncertainties to be applied within that region.

1655 Using this procedure the systematic uncertainties for each region are calculated and  
1656 are shown in Table 4.13, with the systematic uncertainty to be used in the likelihood  
1657 model conservatively rounded up to the nearest decile, shown in brackets.

$H_T$ band (GeV)	$2 \leq n_{jet} \leq 3$	$n_{jet} \geq 4$
$275 < H_T < 325$	6 (10)%	3 (10)%
$325 < H_T < 375$	6 (10)%	6 (10)%
$375 < H_T < 575$	7 (10)%	9 (10)%
$575 < H_T < 775$	13 (20)%	15 (20)%
$H_T > 775$	19 (20)%	21 (30)%

**Table 4.13.:** Calculated systematic uncertainties for the five  $H_T$  regions, determined from the closure tests. Uncertainties shown for both jet multiplicity categories. Values used within the likelihood model are conservatively rounded up to the nearest decile and shown in brackets.

1658 Figure 4.10 shows the sets of closure tests overlaid on top of grey bands that represent  
1659 the  $H_T$  dependent systematic uncertainties. These systematic uncertainties are assumed  
1660 to fully uncorrelated between the different  $n_b$  multiplicity categories and across the five  
1661  $H_T$  regions. This can be considered a more conservative approach given that some  
1662 correlations between adjacent  $H_T$  bins could be expected due to comparable kinematics.

1663 As already referenced. These closure tests represent a conservative estimate of the  
1664 systematic uncertainty in making a background prediction for the signal region. This  
1665 is due to significant differences in the background composition and event kinematics  
1666 between the two sub-samples used in the closure tests. This is contrary to the signal  
1667 region prediction where the two sub-samples are both have a comparable background

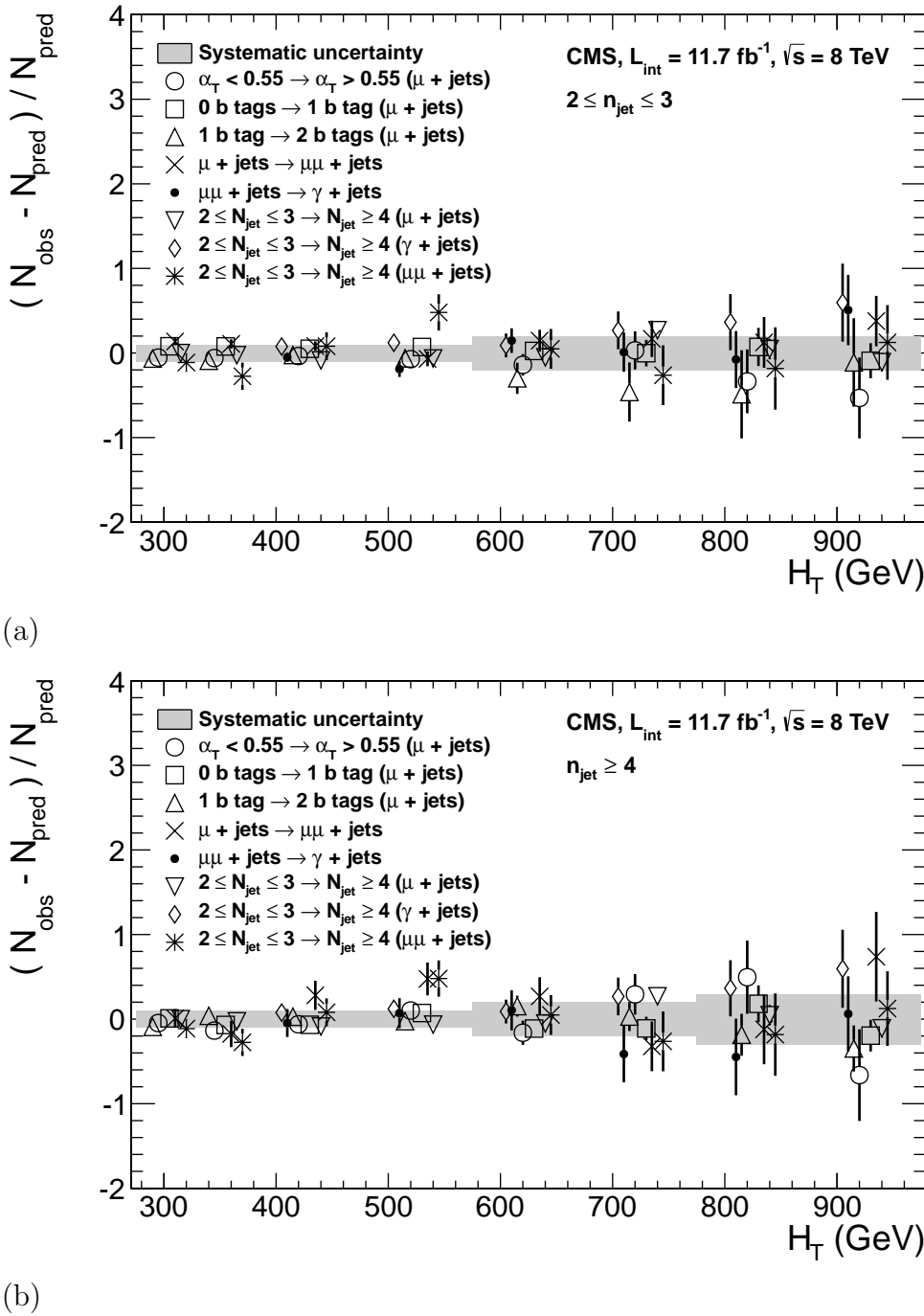


**Figure 4.10.: Sets of closure tests (open symbols) overlaid on top of the systematic uncertainty used for each of the five  $H_T$  regions (shaded bands) and for the two different jet multiplicity bins: (a)  $2 \leq n_{\text{jet}} \leq 3$  and (b)  $n_{\text{jet}} \geq 4$ .**

1668 admixture and similar kinematics owing to the fact that the predictions are always made  
 1669 using the same  $(n_{\text{jet}}, n_b, H_T)$  bin.

1670 This point is emphasised when we examine the sensitivity of the **TF**'s to a change  
1671 in the admixture of  $W + \text{jets}$  and  $t\bar{t}$  with the control and signal samples. This is  
1672 accomplished by varying the cross sections of the  $W + \text{jets}$  and  $t\bar{t}$  by +20% and -20%,  
1673 respectively. Figures C.2 and C.3 within Appendix C, show the effect upon the closure  
1674 tests for both jet multiplicity categories. Given these variations in cross sections, the  
1675 level of closure is found to be significantly worse, with biases as large as  $\sim 30\%$ , most  
1676 apparent in the lowest  $H_T$  bins. However the **TF**'s used to extrapolate from control to  
1677 signal are seen to change only at the percent level by this large change in cross section,  
1678 shown in Table C.1.

1679 Given the robust behaviour of the translation factors with respect to large (and  
1680 opposite) variations in the  $W + \text{jets}$  and  $t\bar{t}$  cross sections, one can assume with confidence  
1681 that any bias in the translation factors is adequately (and conservatively) covered by the  
1682 systematic uncertainties used in the analysis.

# Chapter 5.

## <sup>1683</sup> Searches For Natural SUSY With <sup>1684</sup> B-tag Templates.

<sup>1685</sup> Within this chapter a complimentary technique is discussed as a means to predict the  
<sup>1686</sup> distribution of three and four reconstructed b-quark jets in an event. The recent discovery  
<sup>1687</sup> of the Higgs boson has made third-generation “Natural SUSY” models attractive, given  
<sup>1688</sup> that light top and bottom squarks are a candidate to stabilise divergent loop corrections  
<sup>1689</sup> to the Higgs boson mass.

<sup>1690</sup> Using the  $\alpha_T$  search as a base, a simple templated fit is employed to estimate the  
<sup>1691</sup> SM background in higher b-tag multiplicities (3-4) from a region of a low number of  
<sup>1692</sup> reconstructed b-jets (0-2). As a proof-of-concept, the procedure after being shown to  
<sup>1693</sup> close in simulation, is applied to the SM enriched  $\mu + \text{jets}$  control sample of the  $\alpha_T$   
<sup>1694</sup> all-hadronic search detailed in Chapter 4. Results are presented using the CSV tagger  
<sup>1695</sup> (introduced in Section (3.3.2)) for the “Loose”, “Medium” and “Tight” working points.

### <sup>1696</sup> 5.1. Concept

<sup>1697</sup> The dominant SM backgrounds most SUSY searches are typically  $t\bar{t} + \text{jets}$ ,  $W + \text{jets}$  and  
<sup>1698</sup>  $Z \rightarrow \nu\bar{\nu} + \text{jets}$ . These process are characterised by typically having zero or two underlying  
<sup>1699</sup> b-quarks per event. The first step in this approach is to categorise two templates to be  
<sup>1700</sup> fitted to the low  $n_b^{reco}$  multiplicity in terms of these underlying b-quark event topologies :

<sup>1701</sup> Z0 -  $W + \text{jets}$ ,  $Z \rightarrow \nu\bar{\nu} + \text{jets}$ , DY + jets

<sup>1702</sup> Z2 -  $t\bar{t}$ , single top

1703 where Z0 and Z2 represent processes which have an underlying b-quark content of  
 1704 zero or two respectively.

1705 Both these templates can be generated through the application of the relevant event  
 1706 selection and taking the underlying  $n_b^{reco}$  distribution directly from simulation. However  
 1707 as discussed within Section (4.5), there are large uncertainties for high  $n_b^{reco}$  multiplicities  
 1708 due to limited MC statistics. This is particularly prominent for the Z0 templates, where  
 1709 the number of reconstructed b-tags is driven primarily by the light-quark mis-tagging  
 1710 rate. Therefore to improve the statistical precision of the predictions the formula method,  
 1711 introduced in Section (4.5.1) is used.

1712 The generation of these templates is then dependant upon the jet-flavour content and  
 1713 b-tagging rate within the phase space of interest, with the tagging probabilities of a jet  
 1714 being a function of the jet  $p_T$ , the pseudo-rapidity  $|\eta|$ , and the jet-flavour. This can be  
 1715 observed in Figure 5.1, where the b-tagging / c-quark mis-tagging / light mis-tagging  
 1716 efficiency for the three working points of the CSV tagger is shown as a function of jet  $p_T$ .

1717 Before the templates are generated, the relevant jet  $p_T$  and  $\eta$  corrections are applied  
 1718 to correct simulation to data, as specified in Section (4.5.3), to then determine the average  
 1719 tagging rates per analysis bin.

1720 These two templates are then fit to data in the low  $n_b^{reco}$  region (0-2). The fit result  
 1721 is used, along with the knowledge of the template shapes, to extrapolate an estimate to  
 1722 the high  $n_b^{reco}$  region (3,4), which is then compared to what is observed in data.

1723 This method can, in principle, be applied to any analysis where the signal hypothesis  
 1724 has a larger underlying b-quark spectra than the SM backgrounds, as it solely relies on  
 1725 fitting to the shape of the  $n_b^{reco}$  distribution.

## 1726 5.2. Application to the $\alpha_T$ search

1727 As detailed in the previous chapter, the  $\alpha_T$  analysis is a search for SUSY particles  
 1728 in all-hadronic final states, utilising the kinematic variable  $\alpha_T$  to suppress QCD to a  
 1729 negligible level. SM enriched control samples are used to estimate the background within  
 1730 an all-hadronic signal region.

1731 The selection for the  $\mu +$  jets control samples defined in Section (4.2.3) is used to  
 1732 demonstrate the template fitting procedure both conceptually in simulation, and also

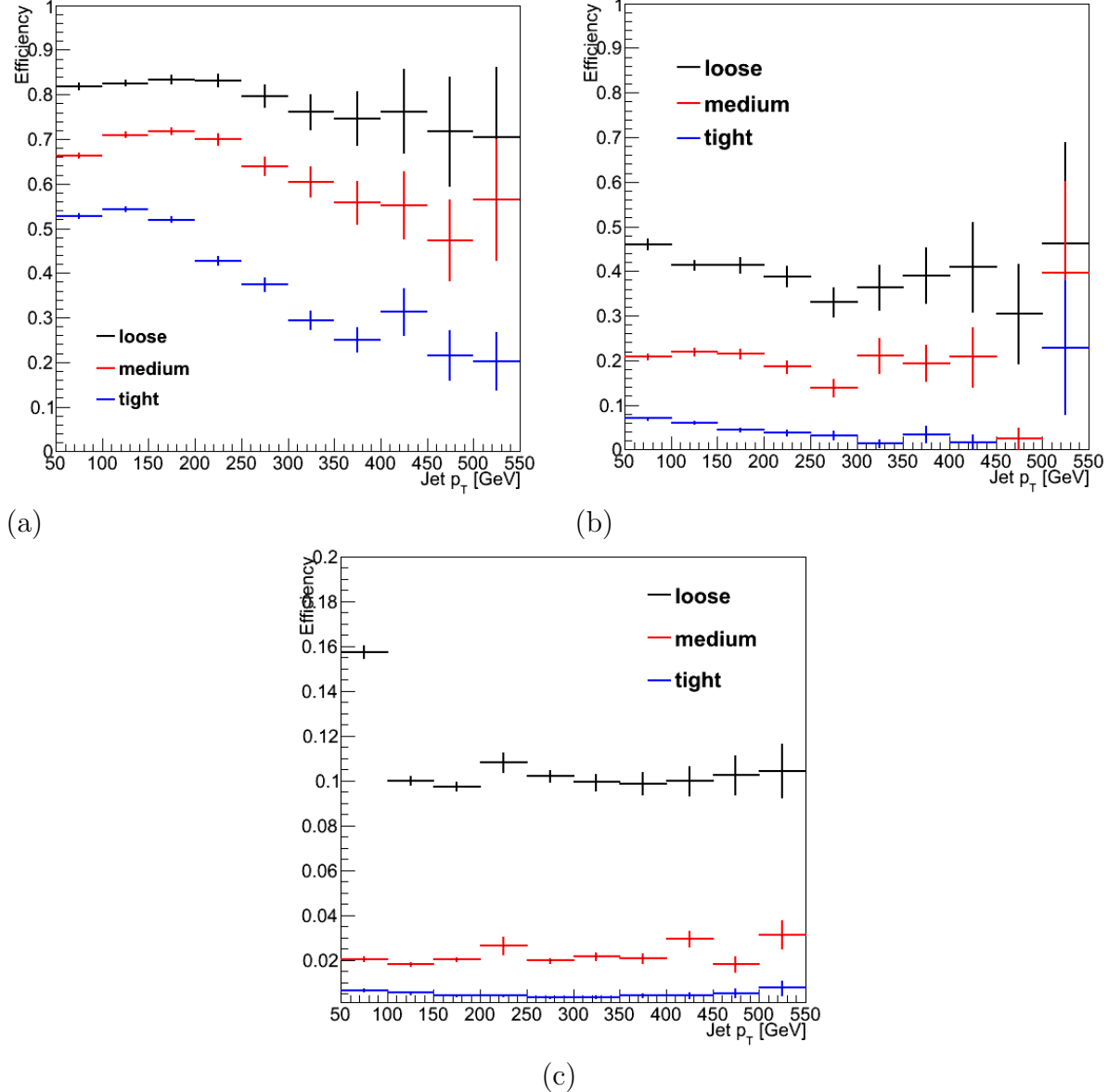


**Figure 5.1.:** The b-tagging (a), c-quark mis-tagging (b), and light-quark mis-tagging rate (c) as measured in simulation after the  $\alpha_T$  analysis,  $\mu + \text{jets}$  control sample selection in the region  $H_T > 375$ .

when applied in data. This is chosen, as such a selection is dominated by events stemming from the SM processes with little or no signal contamination from potential new physics.. Neither are contributions from rate SM processes with a higher underlying b-quark content (e.g.  $t\bar{t}bb$ ) expected. For these reasons, there is a degree of confidence that the procedure should close when applied to this phase space.

The analysis presented here is binning in source jet multiplicity bins, of 3,4 and  $\geq 5$  reconstructed jets per event (di-jet events are not included as there is no contribution

<sub>1740</sub> to the high  $n_b^{reco}$  region (3,4)) , in order to reduce the kinematic jet  $p_T$  dependence.

<sub>1741</sub> Furthermore the analysis is split into three  $H_T$  regions,

<sub>1742</sub> • 275-325 GeV

<sub>1743</sub> • 325-375 GeV

<sub>1744</sub> •  $> 375$  GeV

<sub>1745</sub> contrary to the eight used within the  $\alpha_T$  analysis. Templates for both underlying  
<sub>1746</sub> b-quark content hypotheses are then generated for the nine defined analysis bins.

### <sub>1747</sub> 5.2.1. Proof of principle in simulation

<sub>1748</sub> The to highlight the relative insensitivity of the performance of the b-tagging algorithm

<sub>1749</sub> in the effectiveness of the procedure.

# Chapter 6.

## <sup>1750</sup> Results

<sup>1751</sup> Results at 12fb 8TeV

### <sup>1752</sup> 6.1. Statistical Interpretation

<sup>1753</sup> Likelihood stuff

### <sup>1754</sup> 6.2. Interpretation in Simplified Signal Models

<sup>1755</sup> Result interpretation

<sup>1756</sup>

# Appendix A.

## <sup>1757</sup> Miscellaneous

### <sup>1758</sup> A.1. Noise Filters

<sup>1759</sup> For Calo jets the following criteria were applied:

---

Loose CaloJet Id	
Variable	Definition
$f_{HPD} < 0.98$	Fraction of jet energy contributed from “hottest” <b>HPD</b> , which rejects <b>HCAL</b> noise.
$f_{EM} > 0.01$	Noise from the <b>HCAL</b> is further suppressed by requiring a minimal electromagnetic component to the jet $f_{EM}$ .
$N_{hits}^{90} \geq 2$	Jets that have $> 90\%$ of its energy from a single channel are rejected, to serve as a safety net that catches jets arising from undiagnosed noisy channels.

---

**Table A.1.:** Criteria for a reconstructed jet to pass the loose calorimeter jet id.

<sup>1760</sup> For PF jets the following criteria were applied:

---

Loose PF jet Id	
Variable	Definition
$\text{nfhJet} < 0.99$	Fraction of jet composed of neutral hadrons. <b>HCAL</b> noise tends to populate high values of neutral hadron fraction.
$\text{nemfJet} < 0.99$	Fraction of jet composed of neutral electromagnetic energy. <b>ECAL</b> noise tends to populate high values of neutral EM fraction.
$\text{nmultiJet} > 1$	Number of constituents that jet is composed from.
$\text{chfJet} > 0$	Fraction of jet composed of charged hadrons.
$\text{cmultiJet} > 0$	Number of charged particles that compose jet.
$\text{cemfJet} < 0.99$	Fraction of jet composed of charged electromagnetic energy.

---

**Table A.2.:** Criteria for a reconstructed jet to pass the loose PF jet id.

1761      The following noise filters are applied, to remove events with spurious, non-physical  
1762      jets or missing transverse energy.

---

Noise Filters	
Variable	Definition
CSC tight beam halo filter	As proton beams circle the <b>LHC</b> , proton interactions with the residual gas particles or the beam collimators can occur, producing showers of secondary particles which can interact with the <b>CMS</b> detector.
HBHE noise filter with isolated noise rejection	Anomalous noise in the <b>HCAL</b> not due to electronics noise, but rather due to instrumentation issues associated with the <b>HPD</b> 's and Readout Boxes ( <b>RBXs</b> ).
HCAL laser filter	The <b>HCAL</b> uses laser pulses for monitoring the detector response. Some laser pulses have accidentally been fired in the physics orbit, and ended up polluting events recorded for physics analysis.
ECAL dead cell trigger primitive (TP) filter	<b>EB</b> and <b>EE</b> have single noisy crystals which are masked in reconstruction. Use the Trigger Primitive ( <b>TP</b> ) information to assess how much energy was lost in masked cells.
Bad EE Supercrystal filter	Two supercrystals in <b>EE</b> are found to occasionally produce high amplitude anomalous pulses in several channels at once, causing a large $E_T'$ spike.
ECAL Laser correction filter	A laser calibration multiplicative factor is applied to correct for transparency loss in each crystal during irradiation. A small number of crystals receive unphysically large values of this correction and become very energetic, resulting in $E_T'$ .

---

**Table A.3.:** Noise filters that are applied to remove spurious and non-physical  $E_T'$  signatures within the **CMS** detector.

## <sup>1763</sup> A.2. Primary Vertices

<sup>1764</sup> The pileup per event is defined by the number of 'good' reconstructed primary vertices  
<sup>1765</sup> in the event, with each vertex satisfying the following requirements

---

Good primary vertex requirement	
Variable	Definition
$N_{dof} > 4$	The number of degree of freedom, from the vertex fit to compute the best estimate of the vertex parameters.
$ \Delta z_{vtx}  < 24\text{cm}$	The distance, $ \Delta z_{vtx} $ , to the position of the closest <b>HLT</b> primary vertex.
$\rho < 2\text{cm}$	The perpendicular distance of track position to the beam spot.

---

**Table A.4.:** Criteria for a vertex in an event to be classified as a 'good' reconstructed primary vertex.

# Appendix B.

## <sup>1766</sup> L1 Jets

### <sup>1767</sup> B.1. Jet matching efficiencies

<sup>1768</sup> The single jet turn-on curves are derived from events independent of whether the leading  
<sup>1769</sup> jet in an event is matched to a Level 1 jet using  $\Delta R$  matching detailed in Section (3.4.3)  
<sup>1770</sup> or not. These turn-ons are produced from events which are not triggered on jet quantities  
<sup>1771</sup> and therefore it is not guaranteed that the lead jet of an event will be seeded by a Level  
<sup>1772</sup> 1 jet. Figure B.1 shows the particular matching efficiency of a lead jet to a L1 jet.

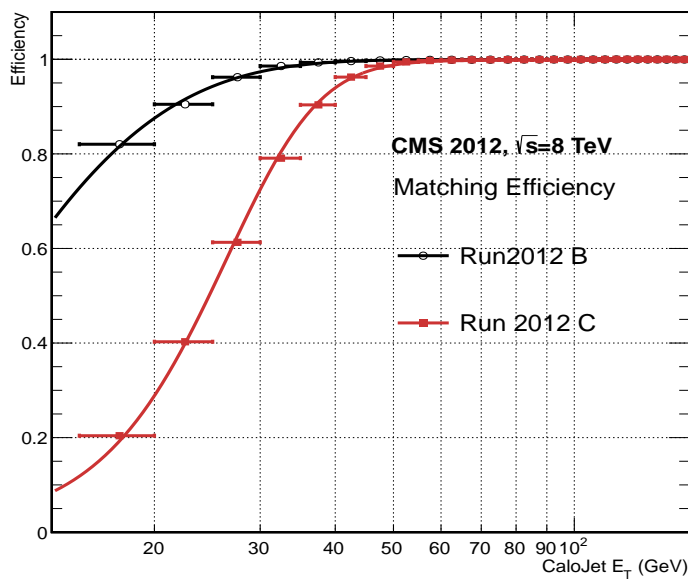


**Figure B.1.:** Leading jet matching efficiency as a function of the offline CaloJet  $E_T$ , measured in an isolated muon triggered dataset in the 2012B and 2012C run periods.

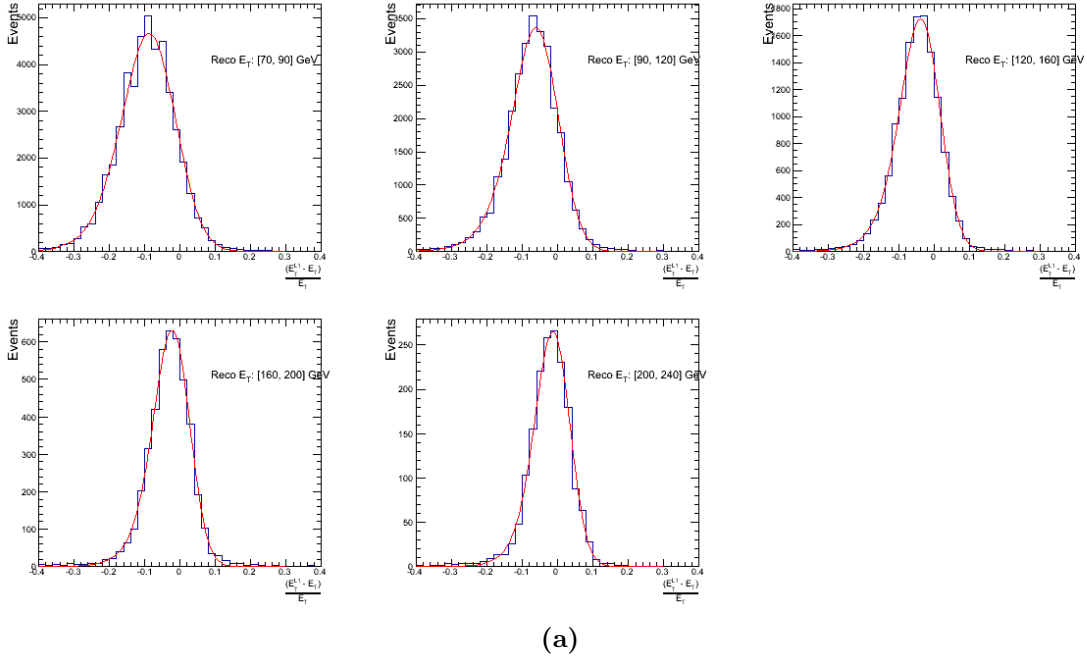
Run Period	$\mu$	$\sigma$
2012B	$6.62 \pm 0.01$	$0.79 \pm 0.03$
2012C	$19.51 \pm 0.03$	$7.14 \pm 0.02$

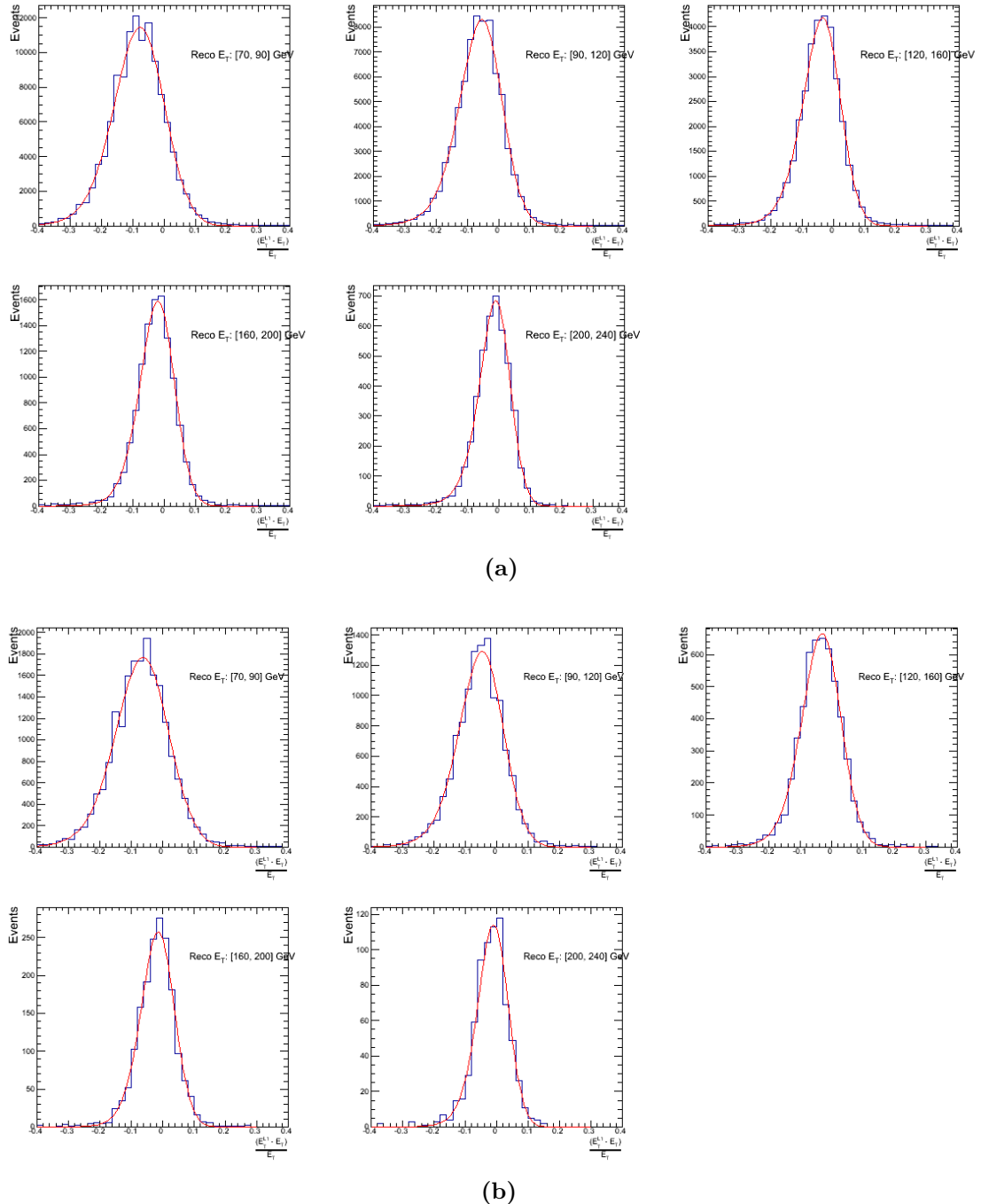
**Table B.1.:** Results of a cumulative EMG function fit to the turn-on curves for the matching efficiency of the leading jet in an event to a Level-1 jet in run 2012C and 2012B data, measured in an isolated muon triggered sample. The turn-on point,  $\mu$ , and resolution,  $\sigma$ , are measured with respect to offline Calo Jet  $E_T$ .

1773 It can be seen that the turn on is sharper during the 2012B run period. The seed  
 1774 threshold requirement of a 5 GeV jet seed in run 2012C results in more events in which  
 1775 even the lead offline jet does not have an associated L1 jet. For larger jet  $E_T$  thresholds,  
 1776 typical of thresholds used in physics analyses, 100% efficiency is observed.

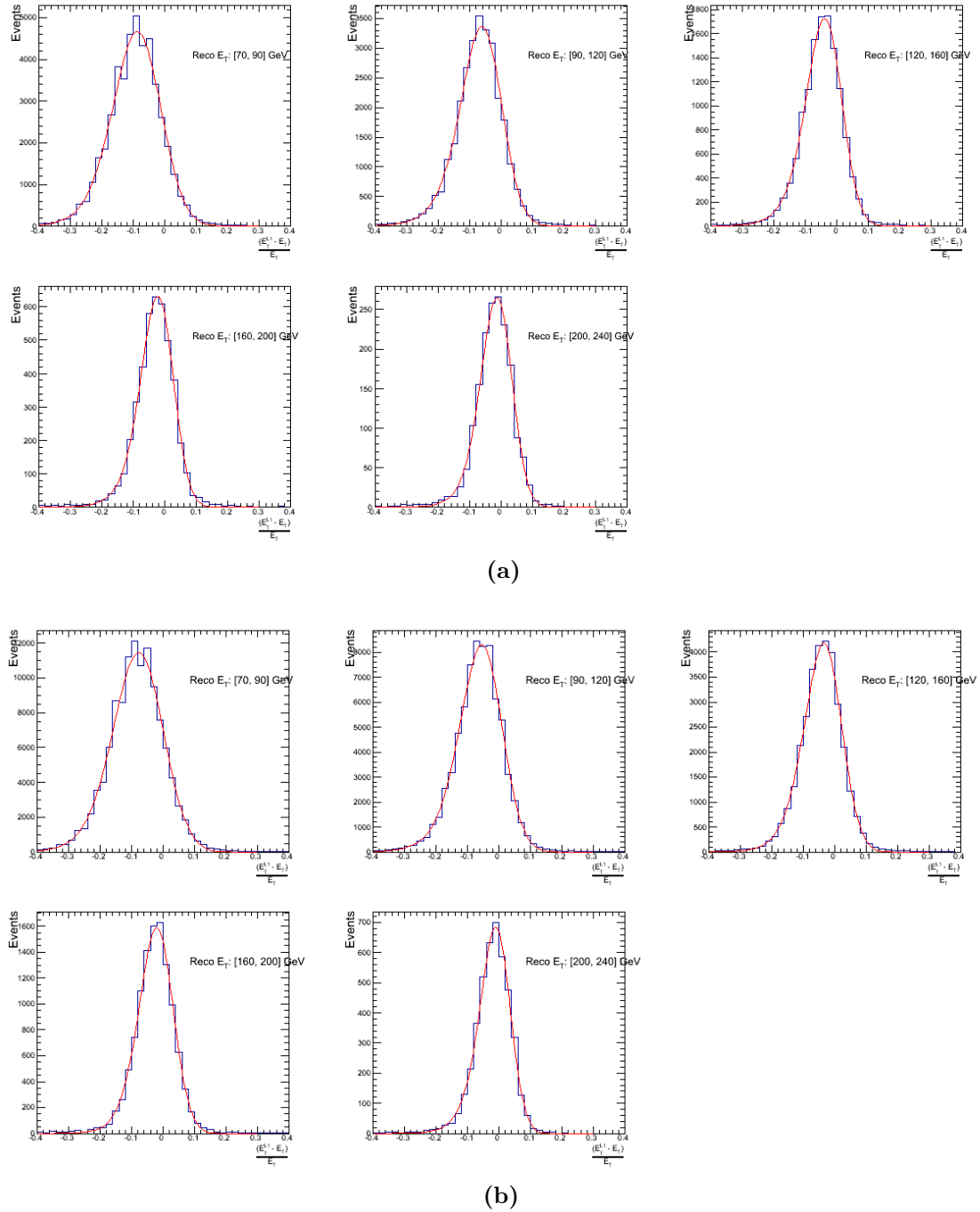
1777 The matching efficiencies have a  $\mu$  values of 6.62 GeV and 19.51 GeV for Run 2012B  
 1778 and 2012C respectively and is shown in Table B.1.

## 1779 B.2. Leading Jet Energy Resolution





**Figure B.2.:** Resolution plots of the leading offline jet Calo  $E_T$  measured as a function of  $\frac{(\text{L1 } E_T - \text{Offline } E_T)}{\text{Offline } E_T}$  for low (a), medium (b) and high (c) pile-up conditions.



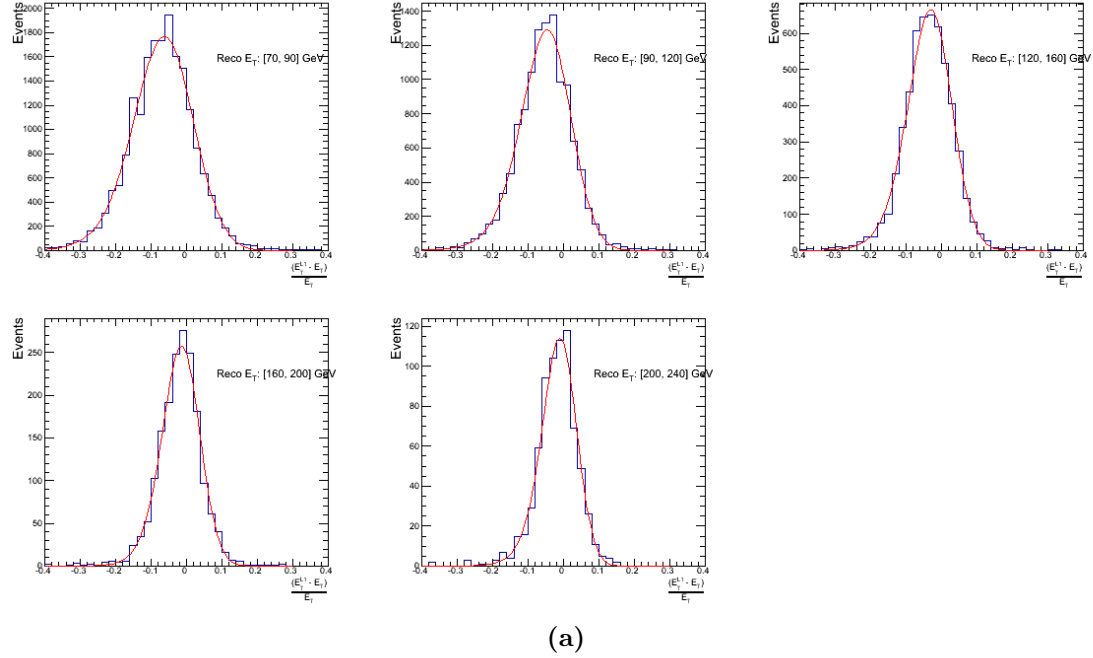


**Figure B.3.:** Resolution plots of the leading offline jet PF  $E_T$  measured as a function of  $\frac{(L1 E_T - \text{Offline } E_T)}{\text{Offline } E_T}$  for low (a), medium (b) and high (c) pile-up conditions.

### 1780 B.3. Resolution for Energy Sum Quantities

1781 The following plots show the resolution parameters for the four energy sum quantities as  
 1782 a function of the quantity ( $q$ ) itself. In this case, The mean and RMS of the individual  
 1783  $\frac{(L1 q - \text{Offline } q)}{\text{Offline } q}$  distributions, in bins of the quantity  $q$  is displayed.

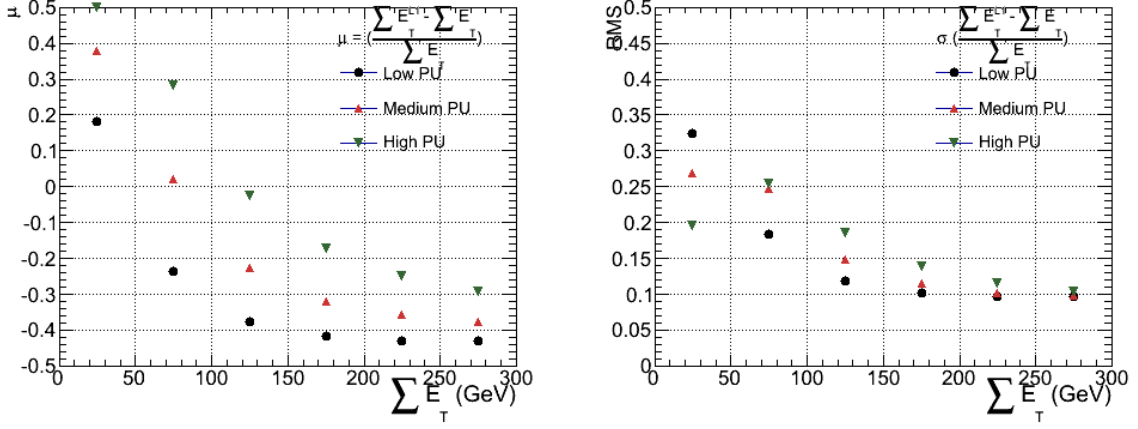


**Figure B.4.:**  $\sum E_T$  resolution parameters in bins of Calo  $\sum E_T$  measured for the defined low, medium and high pile up conditions. The plots show the mean  $\mu$  (left), resolution  $\sigma$  (RMS) of the  $\frac{\Delta q}{q}$  distributions.

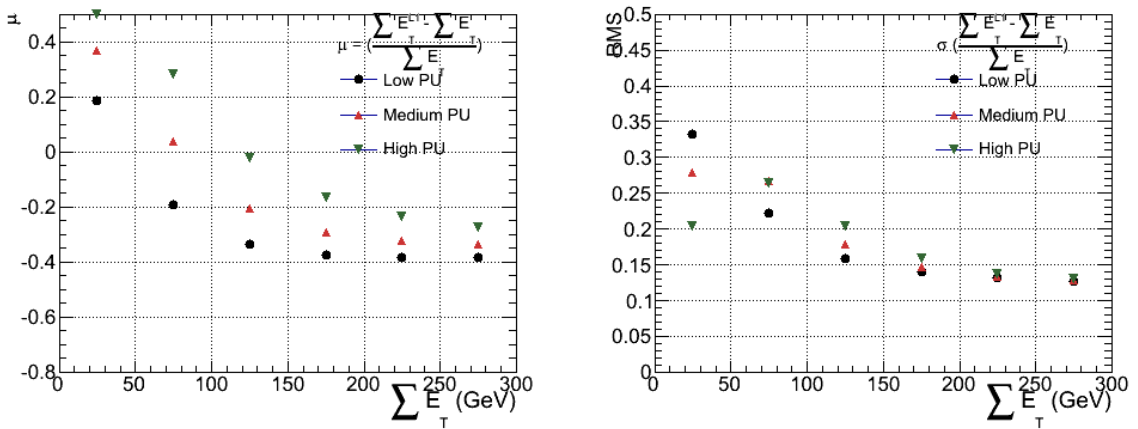


**Figure B.5.:**  $\sum E_T$  resolution parameters in bins of PF  $\sum E_T$  measured for the defined low, medium and high pile up conditions. The plots show the mean  $\mu$  (left), resolution  $\sigma$  (RMS) of the  $\frac{\Delta q}{q}$  distributions.

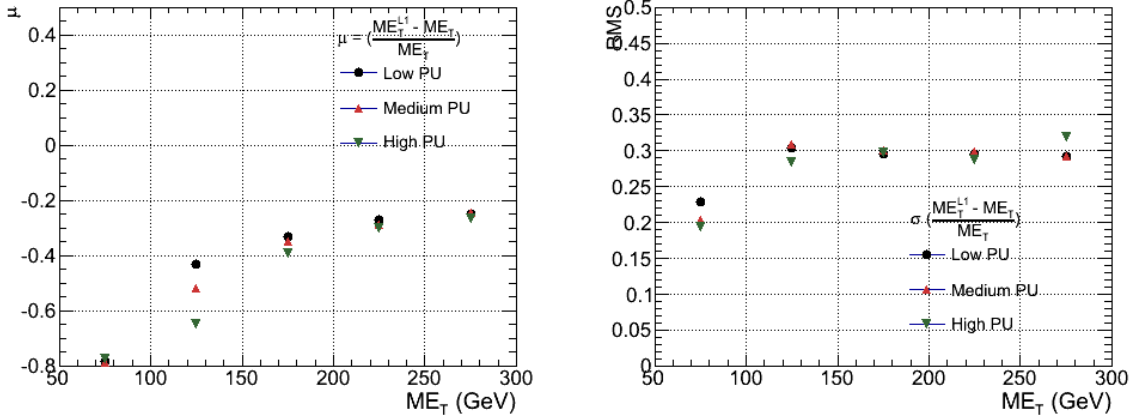


**Figure B.6.:**  $\mathcal{E}_T$  resolution parameters in bins of Calo  $\mathcal{E}_T$  measured for the defined low, medium and high pile up conditions. The plots show the mean  $\mu$  (left), resolution  $\sigma$  (RMS) of the  $\frac{\Delta q}{q}$  distributions.

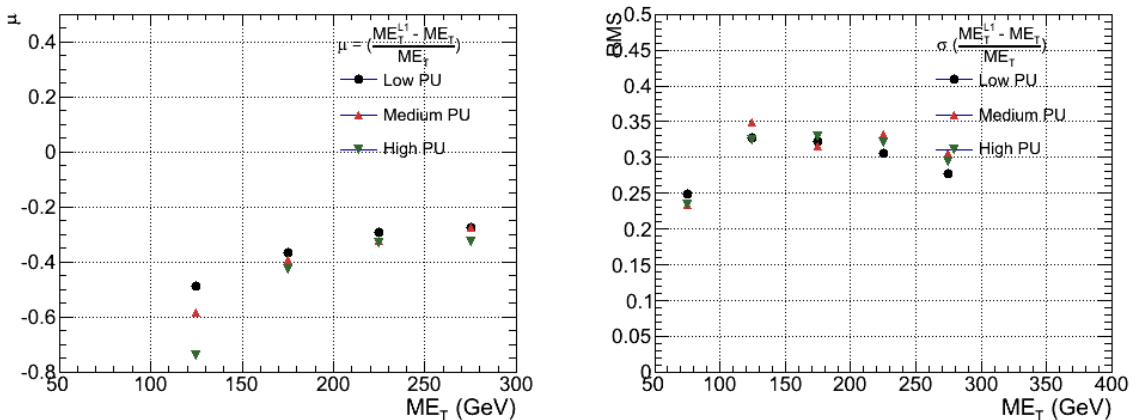


**Figure B.7.:**  $\mathcal{E}_T$  resolution parameters in bins of PF  $\mathcal{E}_T$  measured for the defined low, medium and high pile up conditions. The plots show the mean  $\mu$  (left), resolution  $\sigma$  (RMS) of the  $\frac{\Delta q}{q}$  distributions.

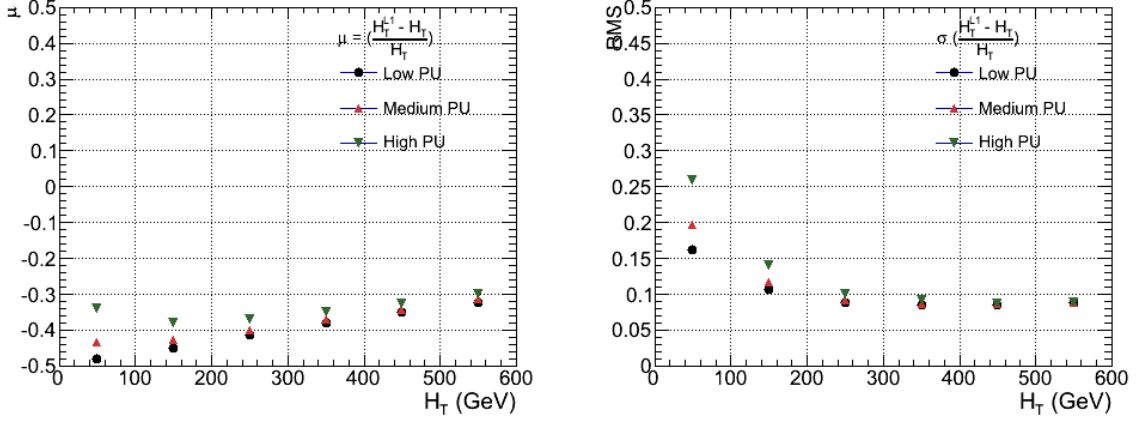


**Figure B.8.:**  $H_T$  resolution parameters in bins of Calo  $H_T$  measured for the defined low, medium and high pile up conditions. The plots show the mean  $\mu$  (left), resolution  $\sigma$  (RMS) of the  $\frac{\Delta q}{q}$  distributions.

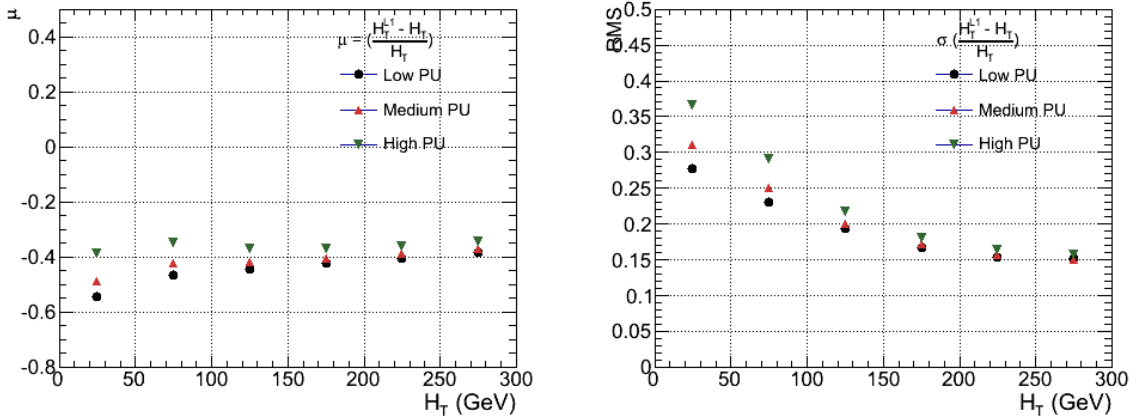


**Figure B.9.:**  $H_T$  resolution parameters in bins of PF  $H_T$  measured for the defined low, medium and high pile up conditions. The plots show the mean  $\mu$  (left), resolution  $\sigma$  (RMS) of the  $\frac{\Delta q}{q}$  distributions.

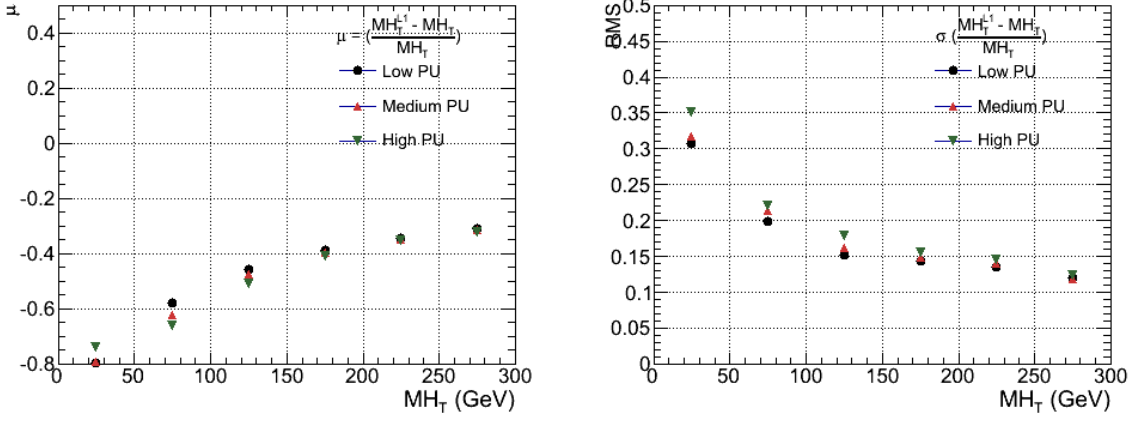


**Figure B.10.:**  $H_T$  resolution parameters in bins of  $H_T$  measured for the defined low, medium and high pile up conditions. The plots show the mean  $\mu$  (left), resolution  $\sigma$  (RMS) of the  $\frac{\Delta q}{q}$  distributions.

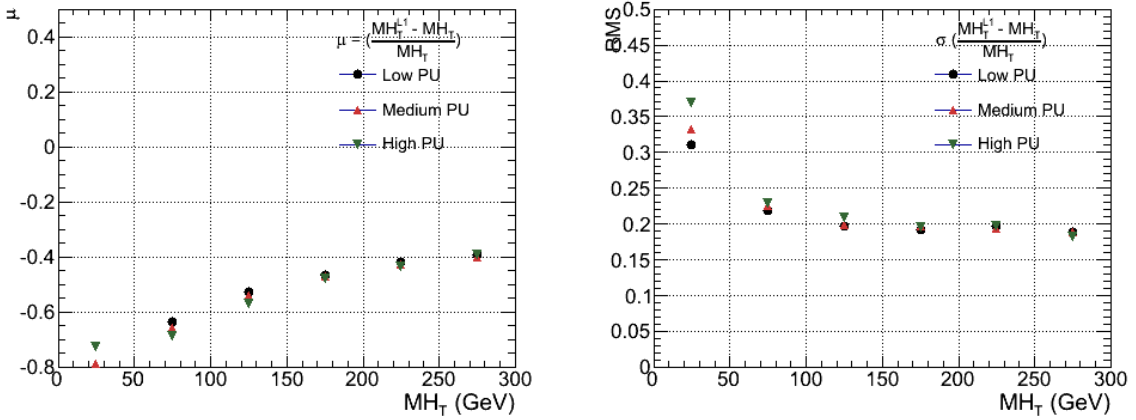


**Figure B.11.:**  $H_T$  resolution parameters in bins of PF  $H_T$  measured for the defined low, medium and high pile up conditions. The plots show the mean  $\mu$  (left), resolution  $\sigma$  (RMS) of the  $\frac{\Delta q}{q}$  distributions.

## Appendix C.

### <sup>1784</sup> Additional material on background estimation methods

#### <sup>1786</sup> C.1. Determination of $k_{QCD}$

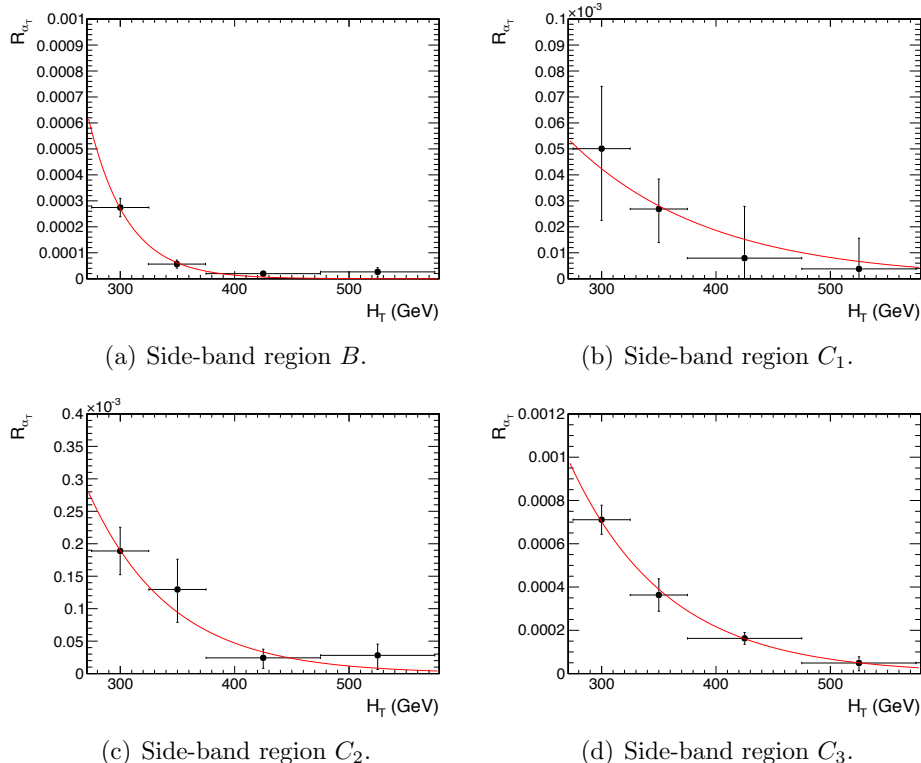


**Figure C.1.:**  $R_{\alpha_T}(H_T)$  and exponential fits for each of the data sideband regions. Fit is conducted between the  $H_T$  region  $275 < H_T < 575$ .

1788 **C.2. Effect of varying background cross sections on**  
1789 **closure tests**

1790 Closure tests with cross section variations of +20% and -20% applied to  $W + \text{jets}$  and  $t\bar{t}$   
1791 processes respectively.

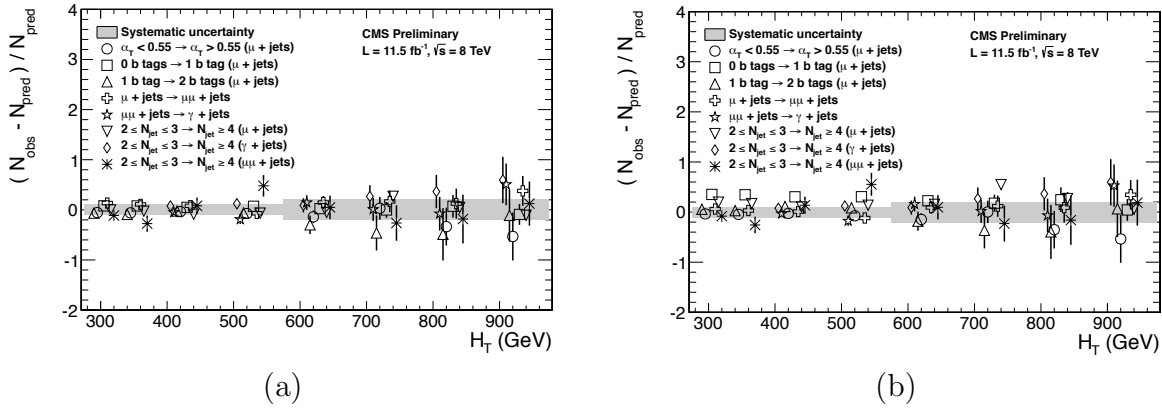


**Figure C.2.:** Sets of closure tests (open symbols) overlaid on top of the systematic uncertainty used for each of the five  $H_T$  regions (shaded bands) and for the two different jet multiplicity bins: (a)  $2 \leq n_{jet} \leq 3$  and (b)  $n_{jet} \geq 4$ .

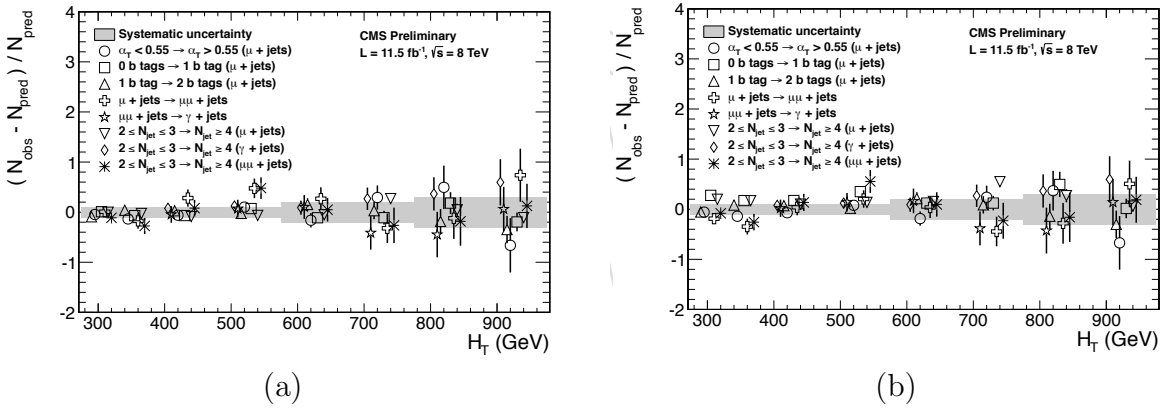


**Figure C.3.:** Sets of closure tests (open symbols) overlaid on top of the systematic uncertainty used for each of the five  $H_T$  regions (shaded bands) and for the two different jet multiplicity bins: (a)  $2 \leq n_{jet} \leq 3$  and (b)  $n_{jet} \geq 4$ .

	$H_T$ (GeV)
--	-------------

**Table C.1.**



# <sup>1793</sup> Bibliography

- <sup>1794</sup> [1] J. Beringer *et al.*, “Review of Particle Physics (RPP),” *Phys.Rev.*, vol. D86, p. 010001, 2012.
- <sup>1795</sup> [2] G. H. et al., “Nine-year wilkinson microwave anisotropy probe (wmap) observations: Cosmological parameter results,” *The Astrophysical Journal Supplement Series*, vol. 208, no. 2, p. 19, 2013.
- <sup>1796</sup> [3] G. Aad *et al.*, “Observation of a new particle in the search for the Standard Model Higgs boson with the ATLAS detector at the LHC,” *Phys.Lett.*, vol. B716, pp. 1–29, 2012.
- <sup>1797</sup> [4] S. Chatrchyan *et al.*, “Observation of a new boson at a mass of 125 GeV with the CMS experiment at the LHC,” *Phys.Lett.*, vol. B716, pp. 30–61, 2012.
- <sup>1798</sup> [5] S. Chatrchyan *et al.*, “Search for supersymmetry in hadronic final states with missing transverse energy using the variables AlphaT and b-quark multiplicity in pp collisions at 8 TeV,” *Eur.Phys.J.*, vol. C73, p. 2568, 2013.
- <sup>1799</sup> [6] S. Weinberg, “A model of leptons,” *Phys. Rev. Lett.*, vol. 19, pp. 1264–1266, Nov 1967.
- <sup>1800</sup> [7] S. Glashow, “Partial Symmetries of Weak Interactions,” *Nucl.Phys.*, vol. 22, pp. 579–588, 1961.
- <sup>1801</sup> [8] A. Salam, “Weak and Electromagnetic Interactions,” *Conf.Proc.*, vol. C680519, pp. 367–377, 1968.
- <sup>1802</sup> [9] G. Hooft, “Renormalizable lagrangians for massive yang-mills fields,” *Nuclear Physics B*, vol. 35, no. 1, pp. 167 – 188, 1971.
- <sup>1803</sup> [10] F. Hasert *et al.*, “Observation of Neutrino Like Interactions Without Muon Or Electron in the Gargamelle Neutrino Experiment,” *Phys.Lett.*, vol. B46, pp. 138–140, 1973.

- 1818 [11] G. Arnison *et al.*, “Experimental Observation of Lepton Pairs of Invariant Mass  
1819 Around 95-GeV/c\*\*2 at the CERN SPS Collider,” *Phys.Lett.*, vol. B126, pp. 398–410,  
1820 1983.
- 1821 [12] M. Banner *et al.*, “Observation of Single Isolated Electrons of High Transverse  
1822 Momentum in Events with Missing Transverse Energy at the CERN anti-p p  
1823 Collider,” *Phys.Lett.*, vol. B122, pp. 476–485, 1983.
- 1824 [13] E. Noether, “Invariante variationsprobleme,” *Nachrichten von der Gesellschaft  
1825 der Wissenschaften zu Gttingen, Mathematisch-Physikalische Klasse*, vol. 1918,  
1826 pp. 235–257, 1918.
- 1827 [14] F. Halzen and A. D. Martin, “Quarks and leptons.” Wiley, 1985.
- 1828 [15] *Introduction to Elementary Particles*. Wiley-VCH, 2nd ed., Oct. 2008.
- 1829 [16] C. S. Wu, E. Ambler, R. W. Hayward, D. D. Hoppes, and R. P. Hudson, “Ex-  
1830 perimental Test of Parity Conservation in Beta Decay,” *Physical Review*, vol. 105,  
1831 pp. 1413–1415, Feb. 1957.
- 1832 [17] P. Higgs, “Broken symmetries, massless particles and gauge fields,” *Physics Letters*,  
1833 vol. 12, no. 2, pp. 132 – 133, 1964.
- 1834 [18] F. Englert and R. Brout, “Broken symmetry and the mass of gauge vector mesons,”  
1835 *Phys. Rev. Lett.*, vol. 13, pp. 321–323, Aug 1964.
- 1836 [19] P. W. Higgs, “Broken symmetries and the masses of gauge bosons,” *Phys. Rev. Lett.*,  
1837 vol. 13, pp. 508–509, Oct 1964.
- 1838 [20] G. S. Guralnik, C. R. Hagen, and T. W. B. Kibble, “Global conservation laws and  
1839 massless particles,” *Phys. Rev. Lett.*, vol. 13, pp. 585–587, Nov 1964.
- 1840 [21] S. Weinberg, “A model of leptons,” *Phys. Rev. Lett.*, vol. 19, pp. 1264–1266, Nov  
1841 1967.
- 1842 [22] H. Yukawa, “On the interaction of elementary particles. i,” *Progress of Theoretical  
1843 Physics Supplement*, vol. 1, pp. 1–10, 1955.
- 1844 [23] Y. e. a. Fukuda, “Evidence for oscillation of atmospheric neutrinos,” *Phys. Rev.  
1845 Lett.*, vol. 81, pp. 1562–1567, Aug 1998.
- 1846 [24] R. Becker-Szendy, C. Bratton, D. Casper, S. Dye, W. Gajewski, *et al.*, “A Search  
1847 for muon-neutrino oscillations with the IMB detector,” *Phys.Rev.Lett.*, vol. 69,

- 1848 pp. 1010–1013, 1992.
- 1849 [25] S. P. Martin, “A Supersymmetry primer,” 1997.
- 1850 [26] H. Nilles, *Supersymmetry, Supergravity and Particle Physics*. Physics reports, North-Holland Physics Publ., 1984.
- 1852 [27] H. E. Haber and G. L. Kane, “The Search for Supersymmetry: Probing Physics Beyond the Standard Model,” *Phys.Rept.*, vol. 117, pp. 75–263, 1985.
- 1854 [28] E. Witten, “Dynamical Breaking of Supersymmetry,” *Nucl.Phys.*, vol. B188, p. 513, 1981.
- 1856 [29] J. Wess and B. Zumino, “Supergauge transformations in four dimensions,” *Nuclear Physics B*, vol. 70, no. 1, pp. 39 – 50, 1974.
- 1858 [30] H. Muller-Kirsten and A. Wiedemann, *Introduction to Supersymmetry*. World Scientific lecture notes in physics, World Scientific, 2010.
- 1860 [31] I. Aitchison, *Supersymmetry in Particle Physics: An Elementary Introduction*. Cambridge University Press, 2007.
- 1862 [32] K. A. Intriligator and N. Seiberg, “Lectures on Supersymmetry Breaking,” *Class.Quant.Grav.*, vol. 24, pp. S741–S772, 2007.
- 1864 [33] Y. Shadmi, “Supersymmetry breaking,” pp. 147–180, 2006.
- 1865 [34] C. Burgess, P. G. Camara, S. de Alwis, S. Giddings, A. Maharana, *et al.*, “Warped Supersymmetry Breaking,” *JHEP*, vol. 0804, p. 053, 2008.
- 1867 [35] H. Murayama, “Supersymmetry breaking made easy, viable, and generic,” 2007.
- 1868 [36] H. Baer and X. Tata, *Weak Scale Supersymmetry: From Superfields to Scattering Events*. Cambridge University Press, 2006.
- 1870 [37] S. P. Martin, “Implications of supersymmetric models with natural r-parity conservation,” 1996.
- 1872 [38] G. L. Kane, C. F. Kolda, L. Roszkowski, and J. D. Wells, “Study of constrained minimal supersymmetry,” *Phys.Rev.*, vol. D49, pp. 6173–6210, 1994.
- 1874 [39] C. Stlege, G. Bertone, D. Cerdeno, M. Fornasa, R. Ruiz de Austri, *et al.*, “Updated global fits of the cmSSM including the latest LHC SUSY and Higgs searches and XENON100 data,” *JCAP*, vol. 1203, p. 030, 2012.

- 1877 [40] M. Citron, J. Ellis, F. Luo, J. Marrouche, K. Olive, *et al.*, “The End of the CMSSM  
1878 Coannihilation Strip is Nigh,” *Phys.Rev.*, vol. D87, p. 036012, 2013.
- 1879 [41] D. Ghosh, M. Guchait, S. Raychaudhuri, and D. Sengupta, “How Constrained is  
1880 the cMSSM?,” *Phys.Rev.*, vol. D86, p. 055007, 2012.
- 1881 [42] D. Alves *et al.*, “Simplified Models for LHC New Physics Searches,” *J.Phys.*, vol. G39,  
1882 p. 105005, 2012.
- 1883 [43] J. Alwall, P. Schuster, and N. Toro, “Simplified Models for a First Characterization  
1884 of New Physics at the LHC,” *Phys.Rev.*, vol. D79, p. 075020, 2009.
- 1885 [44] S. Chatrchyan *et al.*, “Interpretation of Searches for Supersymmetry with simplified  
1886 Models,” *Phys.Rev.*, vol. D88, p. 052017, 2013.
- 1887 [45] J. Hisano, K. Kurosawa, and Y. Nomura, “Natural effective supersymmetry,”  
1888 *Nucl.Phys.*, vol. B584, pp. 3–45, 2000.
- 1889 [46] M. Papucci, J. T. Ruderman, and A. Weiler, “Natural SUSY Endures,” *JHEP*,  
1890 vol. 1209, p. 035, 2012.
- 1891 [47] B. Allanach and B. Gripaios, “Hide and Seek With Natural Supersymmetry at the  
1892 LHC,” *JHEP*, vol. 1205, p. 062, 2012.
- 1893 [48] K. Aamodt *et al.*, “The ALICE experiment at the CERN LHC,” *JINST*, vol. 3,  
1894 p. S08002, 2008.
- 1895 [49] G. Aad *et al.*, “The ATLAS Experiment at the CERN Large Hadron Collider,”  
1896 *JINST*, vol. 3, 2008.
- 1897 [50] R. Adolphi *et al.*, “The cms experiment at the cern lhc,” *JINST*, vol. 0803, p. S08004,  
1898 2008.
- 1899 [51] A. A. Alves *et al.*, “The LHCb Detector at the LHC,” *JINST*, vol. 3, p. S08005,  
1900 2008.
- 1901 [52] J.-L. Caron, “Lhc layout.. schema general du lhc..” Sep 1997.
- 1902 [53] C. Collaboration, “Cms luminosity - public results.”  
1903 twiki.cern.ch/twiki/bin/view/CMSPublic/LumiPublicResults., 2011.
- 1904 [54] CERN, “Cms compact muon solenoid..” <http://public.web.cern.ch/public/Objects/LHC/CMSnc.jpg>  
1905 Feb 2010.

- 1906 [55] *The CMS electromagnetic calorimeter project: Technical Design Report*. Technical  
1907 Design Report CMS, Geneva: CERN, 1997.
- 1908 [56] *The CMS muon project: Technical Design Report*. Technical Design Report CMS,  
1909 Geneva: CERN, 1997.
- 1910 [57] CMS Collaboration, “The cms physics technical design report, volume 1,”  
1911 *CERN/LHCC*, vol. 2006-001, 2006.
- 1912 [58] M. Cacciari, G. P. Salam, and G. Soyez, “The anti-  $k_t$  jet clustering algorithm,”  
1913 *Journal of High Energy Physics*, vol. 2008, no. 04, p. 063, 2008.
- 1914 [59] “Jet performance in pp collisions at 7 tev,” Tech. Rep. CMS-PAS-JME-10-003,  
1915 CERN, Geneva, 2010.
- 1916 [60] X. Janssen, “Underlying event and jet reconstruction in cms,” Tech. Rep. CMS-CR-  
1917 2011-012, CERN, Geneva, Jan 2011.
- 1918 [61] T. C. collaboration, “Determination of jet energy calibration and transverse mo-  
1919 mentum resolution in cms,” *Journal of Instrumentation*, vol. 6, no. 11, p. P11002,  
1920 2011.
- 1921 [62] R. Eusebi and on behalf of the CMS collaboration), “Jet energy corrections and  
1922 uncertainties in cms: reducing their impact on physics measurements,” *Journal of  
1923 Physics: Conference Series*, vol. 404, no. 1, p. 012014, 2012.
- 1924 [63] “Algorithms for b Jet identification in CMS,” Tech. Rep. CMS-PAS-BTV-09-001,  
1925 CERN, 2009. Geneva, Jul 2009.
- 1926 [64] “Performance of b tagging at  $\sqrt{s}=8$  tev in multijet, ttbar and boosted topology  
1927 events,” no. CMS-PAS-BTV-13-001, 2013.
- 1928 [65] T. C. collaboration, “Identification of b-quark jets with the cms experiment,” *Journal  
1929 of Instrumentation*, vol. 8, no. 04, p. P04013, 2013.
- 1930 [66] S. Dasu *et al.*, “CMS. The TriDAS project. Technical design report, vol. 1: The  
1931 trigger systems,” 2000.
- 1932 [67] P. Sphicas, “CMS: The TriDAS project. Technical design report, Vol. 2: Data  
1933 acquisition and high-level trigger,” 2002.
- 1934 [68] J. B. et al., “Calibration and Performance of the Jets and Energy Sums in the  
1935 Level-1 Trigger ,” no. CMS IN 2013/006 (2013), 2013.

- 1936 [69] B. et al., “Study of Level-1 Trigger Jet Performance in High Pile-up Running  
1937 Conditions,” no. CMS IN 2013/007 (2013), 2013.
- 1938 [70] J. J. Brooke, “Performance of the cms level-1 trigger,” Tech. Rep. CMS-CR-2012-322.  
1939 CERN-CMS-CR-2012-322, CERN, Geneva, Nov 2012.
- 1940 [71] L. Randall and D. Tucker-Smith, “Dijet searches for supersymmetry at the large  
1941 hadron collider,” *Phys. Rev. Lett.*, vol. 101, p. 221803, Nov 2008.
- 1942 [72] “SUSY searches with dijet events,” 2008.
- 1943 [73] “Search strategy for exclusive multi-jet events from supersymmetry at CMS,” Tech.  
1944 Rep. CMS-PAS-SUS-09-001, CERN, 2009. Geneva, Jul 2009.
- 1945 [74] “Calorimeter Jet Quality Criteria for the First CMS Collision Data,” Tech. Rep.  
1946 CMS-PAS-JME-09-008, CERN, 2010. Geneva, Apr 2010.
- 1947 [75] T. C. collaboration, “Performance of cms muon reconstruction in pp collision events  
1948 at  $\sqrt{s} = 7$  tev,” *Journal of Instrumentation*, vol. 7, no. 10, p. P10002, 2012.
- 1949 [76] “Search for supersymmetry in events with photons and missing energy,” Tech. Rep.  
1950 CMS-PAS-SUS-12-018, CERN, Geneva, 2012.
- 1951 [77] M. Cacciari and G. P. Salam, “Pileup subtraction using jet areas,” *Phys.Lett.*,  
1952 vol. B659, pp. 119–126, 2008.
- 1953 [78] Z. Bern, G. Diana, L. J. Dixon, F. Febres Cordero, S. Hoche, H. Ita, D. A. Kosower,  
1954 D. Maitre, and K. J. Ozeren, “Driving missing data at next-to-leading order,” *Phys.  
1955 Rev. D*, vol. 84, p. 114002, Dec 2011.
- 1956 [79] “Data-Driven Estimation of the Invisible Z Background to the SUSY MET Plus  
1957 Jets Search,” Tech. Rep. CMS-PAS-SUS-08-002, CERN, 2009. Geneva, Jan 2009.
- 1958 [80] Z. Bern, G. Diana, L. Dixon, F. Febres Cordero, S. Hoche, *et al.*, “Driving Missing  
1959 Data at Next-to-Leading Order,” *Phys.Rev.*, vol. D84, p. 114002, 2011.